Università degli studi di udine

Dipartimento politécnico di ingegneria e architetura

PhD in industrial and information engineering

Piezoelectric units with self-tuning multi-resonant shunts for vibration absorption

by

Gabriel Konda Rodrigues

Supervisor

Paolo Gardonio

academic year 2021-2022

ACKNOWLEDGEMENTS

This work would not be possible without the work and support of many. Here I try to recognise their assistance through this three years of work.

Firstly, I would like to thank God for creation, motivation, strength and everything else that was required to realise this work;

To my dear family for the unconditional support throughout the years;

To my beloved Júlia, my partner for all good and bad moments (even when faraway);

To Prof. Paolo Gardonio, for the opportunity and supervision on this doctorate research;

To Dr. Emanuele Turco, for his assistance on the research and with the paperwork for international students;

To Dr. Loris dal Bo, for the assistance on the experimental setup;

To the PhD office workers, for the assistance on all matters regarding the administration of my Ph.D;

To my office fellows and my friends. Thank you.

Lastly, I would like to acknowledge the funding support of the Italian Ministry of Education, University and Research (MIUR) through the project DEVISU, funded under the scheme PRIN-2107 – grant agreement No. 22017ZX9X4K006.

To my dear family and to the fellow reader

ABSTRACT

This thesis is focused on a lightweight and modular control system formed by a piezoelectric patch connected to either a single-resonant or a multi-resonant self-tuning shunt, which can be used to mitigate the resonant response of one or multiple low-order flexural modes of a hosting structure. The aim of the study is to develop a self-contained unit, which can be bonded in batches on thin structures to decrease the low frequency flexural response generated by stationary stochastic disturbances.

To this end, the study investigates the optimal tuning of both single-resonant and multi-resonant shunts with reference to a global and a local cost function. Two configurations of the single-resonant shunt are considered, which are formed by a resistance-inductance (RL) connected respectively in series and in parallel. Instead, a single configuration of the multi-resonant shunt is investigated, which is formed by an array of parallel branches encompassing a resistance-inductance-capacitance (RLC) connected in series. The global cost function, given by the minimisation of the hosting structure time-averaged total flexural kinetic energy, is used as a reference metric to assess the optimal tuning of the shunt. Instead, the local cost function, given by the maximisation of the time-averaged electric power absorbed either by the RL single-resonant shunt or by each RLC branch of the multi-resonant shunt, is employed for the practical implementation of the self-tuning shunt.

The study shows that, with respect to the resistance and inductance shunt parameters, the two cost functions are characterised by mirror bell surfaces. Hence, the optimal shunt resistance and inductance values that would minimise the global cost function coincide with those that would maximise the local cost functions. As a result, both the single-resonant and multi-resonant shunts can be suitably tuned within the shunt itself by maximising the time-average electric power absorbed by the single-resonant shunt or by each branch of the multi-resonant shunt. The study also shows that, the tuning can be effectively implemented with a recursive two-paths tuning approach, whereby the inductance is first tuned along a constant-resistance path characterised by a bell shaped curve of the cost function and then the resistance is tuned along a constant-inductance path characterised by a bell shaped curve of the cost function too. This two-paths tuning sequence can be run recursively online such that the shunt can be adapted to variations of the electro-mechanical response of the hosting structure and

piezoelectric transducer as well as to variations of the electric response of the shunt components, which can both occur in presence of temperature variations or other exogenous physical effects.

Since the optimisations along the constant resistance and constant inductance paths are characterised by non-convex cost functions, the study proposes to employ the extremum seeking algorithm to find the optimal shunt parameters that would maximise the electric power absorption. This is a model-free gradient driven search algorithm, which asymptotically leads to the maximum of the non-convex bell-shaped paths. The algorithm is based on a periodic dithering signal that perturbs the inductance and resistance tuning signals such that the resulting electric power absorbed by the shunt equally shows such a periodic signal, which is either in phase or out-of-phase with the dithering signal depending the tuning is under or over estimating the shunt parameter with respect to the optimal one that maximises the power absorption. The study shows that this algorithm suitably leads to the optimal shunt values regardless the structure is excited by a stochastic disturbance such that the power cost function undergoes significant variations over time.

Keywords: Semi-active control; Power maximisation; Adaptive absorber; Broadband control; Extremum seeking;

Contents

List of Figures

Chapter 1

Introduction

Noise transmission through lightweight structures is a relevant problem for civil transportation vehicles [1]–[6]. Due to national and international regulations on carbon emissions and ecological impact combined with the market demands for low costs and high efficiency-high comfort standards of land and air vehicles have brought the transportation industry to develop new designs based on lightweight and low-cost materials. These materials fulfil most of these demands as they entail: a) less raw material and thus lower manufacturing costs and lower ecological footprint and b) lower fuel consumption and thus lower carbon emissions and lower operational costs. However, they are characterised by poor vibration and noise insulation properties too, which degrade interior noise comfort in the vehicles [1], [2], [4]. Therefore, during the past three decades, there has been a steady move towards new designs of aircraft fuselage, automobile bodywork, railway carriage, etc., which increasingly incorporate lightweight and stiff thin panels, often made of low-cost materials. This has a direct impact on the air-borne and structure-borne noise transmission to the interior of the vehicles. In the first place, the flexural vibration fields of these panels couple more efficiently with the interior acoustic fields of the vehicles. In fact, the coincidence frequencies between the panels flexural vibrations and the interior acoustics are shifted to lower values, exactly in the audio frequency range that outlines the comfort of passengers [7]. In the second place, the low modal density, and thus low modal overlap [7]–[9], the frequency range of these structures tend to shift from very low frequencies (normally below 100 Hz) towards higher frequencies (up to 500 Hz or even 1 kHz). As a result, the critical audio frequency range for the comfort of passengers is characterised by distinct resonances due to

the lightly damped resonant responses of the low order flexural modes of the lightweight and stiff panels. To mitigate these issues, vibration control techniques are required to fully suffice these new challenges. The following sections will present a brief overview on the control approaches. Traditionally, the methods are divided into passive or active based on the dependence on an external power source. There are also mixed approaches being referred as semi-active (or semi-passive) which is partially dependent on an external supply.

1.1 Passive Vibration Control

Passive control strategies are based on the manipulation of the fundamental characteristics of a dynamic system. The resonant behaviour of a system can be adjusted by changing the mass and stiffness of the system, in order to avoid certain disturbance frequencies. In case of very narrow frequency band or even tonal excitation, a localised mass addition, such as the balancing procedure for vehicle wheels, is a suitable option. Increasing the structural dampening is another resource to mitigate the response of systems. This latter approach is very common in household appliances specially with foams (which scatter sound waves) and viscoelastic materials (which have high structural damping). The applications are often related to control acoustic emissions and reflections, reducing interior reverberation for better sound comfort.

Another passive approach is to isolate connections points to reduce transmission. This approach is usually applied in the cases where the main cause of vibration cannot be removed nor directly controlled without degrading other aspects of the system. Vehicles with internal combustion engines are one example of application of this isolation technique. The engine parameters cannot be modified without a severe penalty of the performance objectives, thus the coupling to the chassis is made with rubber joints, which also add a considerable amount of damping. In addition, the engine bay has another insulation, a foam layer, which is responsible for thermal and acoustic comfort inside the vehicle. Another example of isolation for vibration control is tumble drum suspension in washing machines. The random distribution of the clothing inside the drum during centrifuge cycle is a spinning unbalanced system, but unlike the vehicle wheel unbalancing that is predictable and stable, the tumble drum mass distribution changes for every water extraction cycle. Thus, the only reliable way, so far, to mitigate this issue is by isolating the rotating system.

A last resource for passive vibration control is the utilisation of a secondary system that is designed to match a specific resonant frequency for a given structure, the so-called vibration absorber. This device extract the energy from the main structure due to its soft stiffness coupling, this means that the mass of the vibration absorber has less resistance to the vibration excitation, thus the energy at the frequency band of the vibration absorber is deflected from the main structure, reducing the resonant effect on the main structure [10]. Because this device is designed to match a specific frequency, it is also referred as tuned vibration absorber (TVA).

In general, these passive solutions have a satisfactory performance for medium to high frequencies and stationary disturbances [11]. To control the low order flexural resonant response and sound radiation of a thin stiff structure, a more effective approach is offered by the TVA, which requires a large seismic mass mounted on a spring-damper suspension element [12]–[16] composed with a soft spring to generate substantial vibration and sound radiation reductions. Thus, classical solutions to mitigate noise transmission at low audio frequencies (e.g. stiffening, viscous damping layers, double walls, porous materials, TVA, Helmholtz resonators, etc.) comes at a substantial mass and volume penalties [12], [17]. Therefore, whenever higher performance standards are necessary or the control action should perform at low frequencies or the system dynamics are not stationary, then active systems are preferred.

1.2 Active Vibration Control

Sensors and actuators are the keywords on the active control approaches. It reason in the simple "if you can sense, you can act and vice-versa", which is not that simple in reality. In fact, the placement of sensors and actuators is one way of categorising the active control, dividing into the collocated control, where the pair sensor-actuator is located, physically, at the same spot on the structure, and the non-collocated control, which the pair is placed at different positions. There is an extensive research field on optimal placement for sensors and actuators in structures, [18]–[22]. A collocated control retains minimal phase, this means that the phase is limited between 0 and 180 degrees, while a non-collocated pair is not phase limited. In fact, the phase is linked to the resonances, or poles, and anti-resonances, zeros, of a system. The occurrence of alternating poles and zeros along the frequency axis limits the phase, Fig. 1.1, since poles shift the phase in -180 degrees and zeros shift in $+180$. When placing the sensor away from the actuator, from collocated to non-collocated configuration, a phenomenon called pole-zero

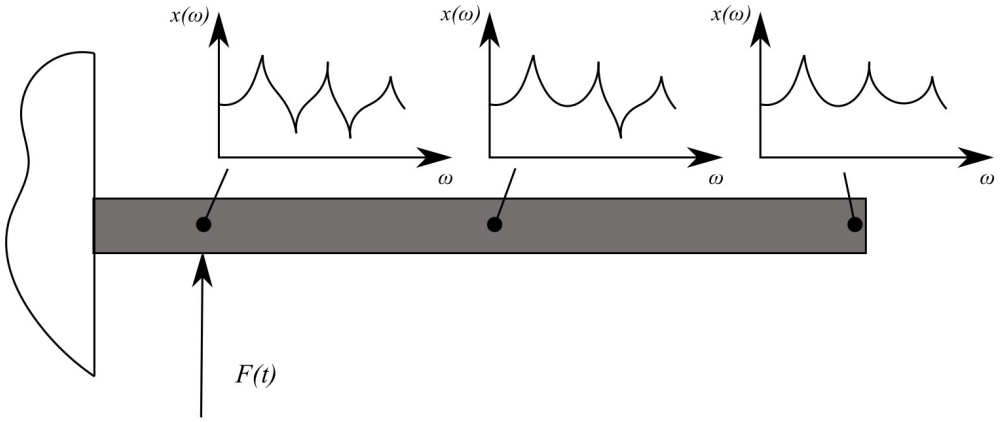

Figure 1.1: Relation between sensor placement, poles and zeros

shift is observed. In practical terms, this translate to a "disappearance" of an anti-resonance from the frequency response, which remove the minimal phase condition. Moreover, this "losing" of zeros is increased as the distance between the sensor-actuator pair is increased. This "loss" of information on phase can be a cause of instabilities for some control loops [23].

Another way to categorise the active control is based on the number of inputs and outputs, namely single-input single-output (SISO) systems, which is constituted by a single pair sensor-actuator, and multiple-input and multiple-output (MIMO) systems. This later can be divided into centralised MIMO, where an array of sensors are connected to a central unit to control an array of actuators [24] and decentralised MIMO, which each pair sensor-actuator have an individual control unit, thus, being effectively an array of SISO systems. Centralised MIMO control have the advantage of being able to control low frequency without the dependency on collocated pairs [25], [26]. However, this configuration can be very complex with a large scale appliances with very complicated control algorithms with the need for reliable and/or redundancy for the sensors and actuators to prevent a general failure, thus requiring lots of wiring (which also adds to cost and weight). On the contrary, the decentralised MIMO can maintain the easiness, since it is basically a SISO control, during the scaling process, it can save on the wiring cost (and weight) and it is much more resilient to a general failure. However, this comes at the cost of cross-talk between the control units, which can become a potential source for instabilities.

Lastly, the categorisation can be based on the control signal path.

Feedforward control is based on a prediction of the disturbance events to apply a predictive correction, see Fig. 1.2, for this reason, feedforward control is also called predictive control. The prediction is based on a very well known system and disturbance, as Fuller [27] described *"[...] feedforward control arrangements require a high degree of accuracy in magnitude and phase of the control system to obtain good cancellation."*. The base for the feedforward control is the compensator, which, as the name implies, creates a compensating effort to minimise the disturbance on the system [28]. The compensating signal is an "anti-signal" that should result in a destructive interference between the external disturbance and the control effort. In order to create the compensating signal, the original disturbance must be directly observed for a proper application of this technique. In addition, the phase must be tightly controlled to insure proper cancellation. To implement this control strategy, adaptive digital filters are often utilised, [11], being the Finite Impulse Response (FIR) filter the most common because of its guaranteed stability [29] at the cost of large real-time computational power.

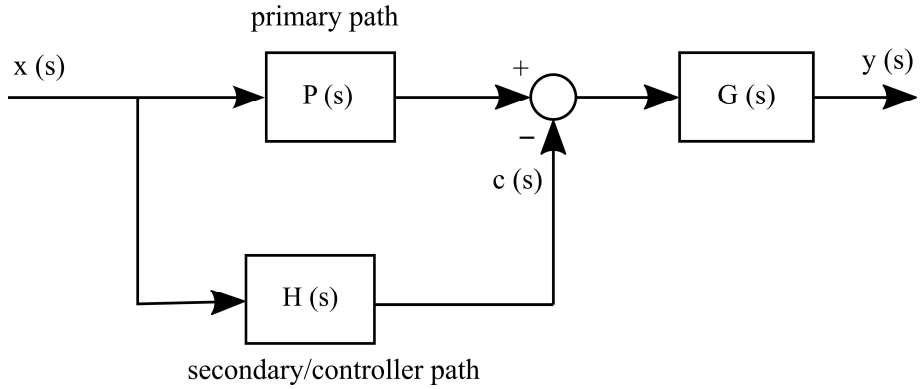

Figure 1.2: Classic feedforward system

Error correction is the keyword for feedback control. A closed loop configuration creates the error signal by feeding the output signal back and subtracting from the reference signal ($e = r - c$), see Fig. 1.3. On the contrary to the feedforward control, the feedback control can be implemented with indirect sensing of the disturbance. A common application is the velocity feedback, which, as the name implies, the measured velocity of a system is fed back through the control path. Thus, as the control system is proportional to the velocity, in physical terms, it has a behaviour of a sky-hook damper, hence, increasing the energy dissipation of the system. Therefore, this approach

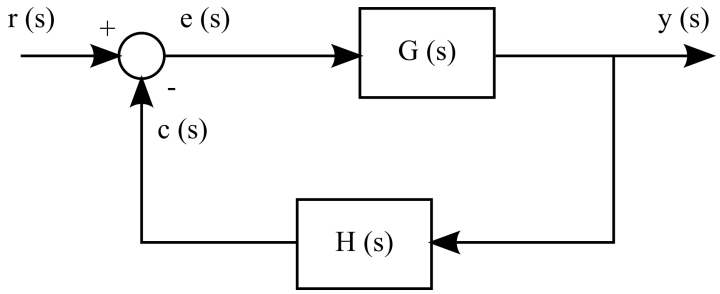

Figure 1.3: Classic feedback system

is particularly effective on lightly-dampened structures [30]–[35]. Another application is the implementation of model-based optimal controllers such as Linear-Quadratic Regulators (LQR) which can provide large reductions inside the bandwidth window of the control. However, the dynamics and disturbances outside of the control bandwidth can cause distortions on the controller operation. These are referred as control spillover and observer spillover, respectively, and they are the main cause of instability on LQR controllers.

Instabilities on the closed loop system is one of the main concerns for the feedback controllers. There are a number of criterion to analyse the stability of systems, e.g., root locus, Nyquist, Routh-Hurwitz, Lyapunov [23], [24], [36], which depends on the knowledge of the system, $G(s)$, and the controller, $H(s)$. The ability of a control loop to reject external disturbances and/or changes on the system/control parameters while retaining its performance is called robustness [11]. This characteristic is crucial for systems, specially for non-linear systems, with a non-negligible uncertainty on its operation.

1.3 Semi-Active Vibration Control

The mixed territory of semi-active control try to combine the advantages of both active and passive solutions while mitigating their drawbacks. As active systems, the semi-active systems requires an external supply of energy, but in a much smaller degree then the fully active systems. This reduces the cost and weight of semi-active controllers in comparison to the active counterpart. In addition, semi-active systems are based on passive devices with adjustable properties, e.g, stiffness and damping, which confers better stability than the active systems and, usually, better performance than the solely passive approaches [23].

1.3.1 Magneto/Electro Rheologic

Magneto/electro-rheological fluids are one example of the application of semi-active control approach. This material changes its viscosity depending on the field that is subjected to. This means by manipulating the magnetic or the electric field it is possible to control the viscosity of the fluid. The control over the viscosity is suitable, for instance, in shock absorbers, where the damping is directly linked to the viscosity of the fluid [37]. Some other applications can employ magneto/electro rheologic materials as Klingenberg noted [38].

1.3.2 Shape Memory Alloy

Shape memory alloys (SMA) is a class of compliant materials that can return to its initial shape after heat exposure. Moreover, under a high-temperature phase, some SMAs exhibit an "extended elastic behaviour" recovering from large deformations, a so-called superelasticity [39]. These thermo-mechanic characteristic and the superelasticity can be exploited for designing variable stiffness springs, where the stiffness can be adjusted by controlling the temperature of the SMA [40]–[42]. Some of the desgin applications that can benefit from such thermo-mechanical behaviour are TVAs [41], mechanical couplers [43] and seismic absorbers [44].

1.3.3 Shunted Electromagnets

Electromagnetic devices are commonly utilised as mechanical actuators, such as speakers , shakers, etc. Nevertheless, the coupling mechanism is dual. Hence, mechanical input results in an electrical output. For this reason, electromagnets with shunt circuitry have been proposed to work as TVAs [45]–[47]. A coil-magnet transducer with the moving part suspended on springs to form a classical mass-spring-damper mechanical vibration absorber. The coil is connected to a resistive-inductive shunt circuit such that a combined damping and stiffness effect is generated via the electromagnetic transduction, which can be used to vary, and thus tune, the natural frequency and damping ratio of the vibration absorber [48]–[53]. This arrangement is particularly suited for the implementation of self-tuning algorithms, which vary online the resistive and inductive components of the shunt in such a way as the fundamental natural frequency and damping ratio of the resulting shunted electromagnetic vibration absorber are continuously adapted to changes of

the hosting structure dynamic response [46], [54]–[58].

1.3.4 Shunted Piezoelectrics

Similarly to electromagnetic devices, piezoelectric devices have the ability to couple electrical and mechanical domains. The utilisation of shunt circuits with piezoelectric material was initially proposed by Forward [59] and later improved by Hagood and von Flotow [60]. The solution, which is adopted in this work, relies on a piezoelectric patch transducer connected to a resistive-inductive shunt circuit. In this case, the resistive-inductive effects of the shunt combined with the capacitive effect of the piezoelectric element generate via the piezoelectric transduction a combined inertia-stiffness-damping action on the hosting mechanical system, which can be used to produce a piezoelectric vibration absorption effect [60]–[69]. With this arrangement too, self-tuning algorithms can be implemented, which vary online the resistive and inductive components of the shunt in such a way as the fundamental natural frequency and damping ratio of the resulting shunted piezoelectric vibration absorber are continuously adapted to changes of the dynamic response of the hosting structure [70]–[74].

1.4 Objectives

The overall goal of this Ph.D. thesis is to study and develop a modular control unit formed by a piezoelectric patch connected to a self-tuning shunt, which can be bonded in batches on thin structures to control the low frequency flexural response due to stochastic broadband disturbances. To this end, the study has been planned and developed with respect to the following specific objectives.

- Firstly, to devise single-resonant and multi-resonant self-tuning shunts for the control of respectively single and multiple resonant responses of low order flexural modes of the hosting structure.

- Secondly, to identify a local cost function for the tuning of the shunts components, which can be implemented within the unit without knowledge of the flexural response of the hosting structure.

- Thirdly, to develop an on-line tuning strategy such that the components of the shunts can be continuously updated and the control unit can

track changes in the electro-mechanical response of the hosting structure and piezoelectric patch and in the electrical response of the shunt itself generated by exogenous factors, such as temperature changes.

1.5 Thesis Contribution

This thesis presents theoretical, simulation and experimental studies on the flexural response of a thin rectangular plate model structure equipped with the modular control units investigated in this study, which are formed by a thin piezoelectric patch connected to a tunable shunt implemented in a digital board. The principal contributions of the study can be summarized in the following points.

- The design of single-resonant and multi-resonant digital shunts that mimic electric circuits formed by a single RL branch or a parallel array of RLC branches, which can be tuned to control the resonant responses of target flexural modes of the hosting structure.
- The conception of a local cost function such that the shunt resistive and inductive components are tuned by setting the time-average electric power absorbed by the single RL branch or by each RLC branch of the single and multi-resonant shunts respectively.
- The simulation and experimental proof that the proposed local cost function leads to the same optimal tuning of the shunt components as those obtained from the reference cost function given by the minimization of the time-average total flexural kinetic energy of the plate, which, indeed, estimates the overall flexural response of the hosting structure.
- The conception and development of a two-paths tuning strategy where the inductive and resistive components in the single-branch or in each branch of the multi-resonant shunt are adjusted independently along constant-resistance and constant-inductance paths.
- The idea of running sequentially the two paths tuning strategy with two feedback loops that implement independently extremum seeking algorithms to search for the maximum of the constant-resistance and constant-inductance curves of the power cost function.
- The demonstration with simulations and experiments of the vibration control effects generated by five control units set to control the resonant response of a single or three resonant modes of the hosting structure.

1.6 Thesis Layout

This work is divided into five chapters. Chapter 2 serves as an introduction to the proposed self-tuning shunted piezoelectric vibration control unit. Chapter 3 and 4 discuss the implementation of the proposed modular control unit on a plate structure. In particular, Chapter 3 discusses the self-tuning of a single-resonant shunt for the control of the resonant response of a target flexural mode of the hosting structure. Alternatively, Chapter 4 presents the self-tuning of a multi-resonant shunt for the control of the resonant responses of multiple target flexural modes of the hosting structure. Finally, Chapter 5 closes this thesis by setting the final remarks of this work and gives suggestions for future research.

Chapter 2

Introduction to the proposed piezoelectric control units connected to a self tuning shunt

---

2.1 Introduction

This chapter presents a theoretical and simulation study on the extremum-seeking online tuning of a piezoelectric vibration absorber for broadband vibration control of a mechanical system subject to stochastic stationary excitation, which is based on the maximisation of the time-averaged electric power absorbed by the shunt.

2.1.1 Background on shunted piezoelectric units for vibration control

The idea of using shunted piezoelectric elements to control the vibration of mechanical systems was introduced in the late 1970 by Forward [59] who investigated the effects produced by a piezoelectric transducer connected to an inductive shunt (L-shunt). About a decade later, Uchino [75] discussed the effects produced by a resistive shunt (R-shunt). Then, in the 1990s, at first Hagood and von Flotow [60], and then Wu [62], studied the effects produced by resistive-inductive shunts (RL-shunt), with the two elements

connected in series and parallel respectively. They showed that these RL-shunts combine with the capacitive effect of the piezoelectric element to form a resonating electric circuit, which, in turn, effectively couples to the resonant response of the hosting system via the piezoelectric transduction. The shunted piezoelectric transducer can thus be set to work as a classical mass-spring-damper mechanical vibration absorber [13], [76], which can be effectively used to control the resonant response of the hosting mechanical system to a stationary stochastic excitation by setting its natural frequency close to the natural frequency of the mechanical system and its damping factor to a value that critically dampen the resulting double-resonance response [13], [76]–[78]. Over the years, several studies were presented to provide approximate or exact tuning laws for the optimal values of the electrical components of either series or parallel RL-shunts (e.g. see Refs. [60], [62]–[67], [79]–[83]), which relay on simple model problems formed by a mass-spring-damper mechanical system coupled to the RL circuit via the transduction effect of a piezoelectric element. In this respect, it is interesting to highlight the works presented by Kim et al. [84]–[86], who derived with a frequency domain formulation the optimal resistance and inductance of the shunt in such a way as to maximise the energy dissipated in the shunt.

2.1.2 Overview of shunt self tuning approaches

In general, variations of both the dynamic response of the hosting system and the electrical response of the shunt, due for example to mechanical tensioning effects and temperature changes, may significantly affect the tuning of the shunt components and thus the vibration control effectiveness of the piezoelectric vibration absorber [65], [70], [87]–[91]. Therefore, real-time adaptive tuning solutions are necessary to guarantee the correct functioning of the shunted piezoelectric absorber under a wide range of operation conditions. In this respect, Hollkamp and Starchville [70] first proposed a self-tuning piezoelectric vibration absorber for the case where the hosting mechanical system is exposed to a stationary stochastic excitation. They suggested that the inductance of a series RL-shunt should be continuously adapted in such a way as to maximise the ratio between the Root-Mean-Square (RMS) of the voltage across the shunt and the RMS of the system response. The RMS of the system response was obtained using an additional piezoelectric element acting as a monitor sensor of the system vibration. The proposed tuning approach was proved experimentally using a synthetic inductor such as a gyrator filter [92], [93]. Fleming and Moheimani [71] reviewed this idea and suggested to use the piezoelectric transducer connected to the shunt itself to monitor

the vibration of the hosting structure. More specifically, they proposed to continuously adapt the inductor of the RL-shunt by maximising the ratio between the RMS of the voltage across the shunt and the RMS voltage of the system response. The adaptive shunt was in this case synthesised using a digital signal processor connected to the piezoelectric patch via a suitable electronic interface circuit [94]–[96]. A rather different approach was taken by Niederberger et al. [72], who, instead of minimising RMS functions, suggested to adapt online the inductance of the shunt by minimising the relative phase difference between a vibration reference signal and the shunt current. A similar approach was used by Gripp et al. [74] who considered a RLC shunt circuit with a negative capacitor, which, as discussed in Refs. [97]–[102], enhances the effectiveness of the shunt.

2.1.3 Proposed self tuning metric and algorithm

This chapter presents a new online approach for the optimal tuning of both the inductive and resistive components of either series or parallel RL-shunts connected to a piezoelectric transducer fixed on resonant mechanical system subject to a stationary stochastic excitation. The tuning is based on an extremum seeking gradient search algorithm that finds the optimal resistance R_s and inductance L_s components of the shunt in such a way as to maximise the time-averaged electric power absorbed by the shunt, $P_e(R_s, L_s)$. The study shows that the power cost function has a bell-type non-convex shape with a single global maximum, which is characterised by two principal directions defined by $R_s = \text{const}$ and $L_s = \text{const}$. Accordingly, it proposes a two-paths tuning algorithm, where the inductance L_s and resistance R_s are tuned sequentially using an extremum seeking gradient search algorithm [103] specifically tailored to the bell-shaped cost function. The proposed tuning, relies on the current through (RL-series) or the voltage across (RL-parallel shunt) the shunt resistance, which can be estimated locally in the shunt in such a way as to form a self-contained adaptive control unit without the need of extra sensors to monitor the vibration of the hosting system. Therefore, it is expected that shunt and tuning algorithm can be effectively implemented in a miniaturised lightweight DSP board characterised by low electric power consumption. In particular, for hosting systems characterised by slow variations of their physical properties, the tuning algorithm can be operated intermittently, possibly using the electric power absorbed by the shunt itself.

The idea of maximising the electric power absorbed by the shunt has

been explored for the tuning of shunted electromagnetic vibration absorbers too. In particular, in Refs. [56], [57] showed that, unlike piezoelectric vibration absorbers, the electric power maximisation cost function can be effectively implemented provided the electromagnetic transducer is characterised by a low mechanical damping.

Extremum seeking control was introduced in the 1950s by Morosanov [104] and Ostrovsky [105] to find the optimal values of static cost functions. More recently, in the 2000s, the implementation of stable feedback extremum seeking control schemes was investigated to search for the optimal values of dynamic cost functions [106]–[109], which have been used in this study to adapt in real-time the tuning of the resistive-inductive components of the shunts.

The maximisation of the time-averaged electric power absorption has been recently considered for the tuning of resistive and inductive components of a shunted electro-magnetic vibration absorber [56], [57]. Also, a similar approach based on the maximisation of the time-averaged vibration power absorption has been employed for the tuning of the control gain of velocity feedback control units using collocated sensor-actuator pairs [16], [110]. In this respect, it is important to underline that this tuning approach is valid for stochastic excitations otherwise, as shown in Ref. [111], the system may actually maximise the vibration power injected in the controlled system by a tonal excitation.

2.1.4 Simple case study

To accurately introduce and analyse the proposed tuning approach, a simple case study is considered, which is composed by a seismic mass mounted onto a piezoelectric elastic element connected to the series or parallel RL-shunt respectively. This system can be modelled with a classical mass-spring-damper mechanical system, which is connected through the piezoelectric transduction to an electric mesh encompassing the inherent capacitance of the piezoelectric transducer and the resistive and inductive components of the series and parallel shunts. A simple model problem is thus considered, which nevertheless replicates the typical resonant response of low-order structural modes of complex structures.

2.1.5 Structure of the chapter

This Chapter is structured in three sections. Section 2.2 presents the state-space and frequency formulations used to derive the response of the single degree of freedom (SDOF) mechanical system equipped with a piezoelectric transducer, which is connected to the series and parallel RL-shunts. Section 2.3 derives and investigates the principal features of the reference cost function given by the time-average of the mechanical kinetic energy and the proposed cost function given by the time-average of the electrical power absorbed in the shunt with respect to the tuning of the shunt RL components. Then, Section 2.4 presents a simulation study on the online implementation of the proposed self-tuning approach using the extremum seeking gradient search algorithm.

2.2 Mechanical system and piezoelectric vibration absorber: lumped parameter model and mathematical formulations

This section first presents the lumped parameter model of the mechanical system and piezoelectric vibration absorber investigated in this thesis. It then introduces the mathematical formulations used to derive the system response and to calculate the time-average kinetic energy of the system and the time-average electric power absorbed by the shunt, which have been used respectively to assess the vibration control performance and to tune the resistive and inductive shunt components of the piezoelectric vibration absorber.

2.2.1 Lumped-parameter model

The study considers a simple electro-mechanical system, which, as shown in Fig. 2.1(a), is characterised by a block mass suspended on a piezoelectric elastic element with thin electrodes at the top and bottom surfaces, which are connected to the self-tuning RL electric shunt. The block mass is exposed to a stationary stochastic force excitation $f(t)$. The piezoelectric element and RL-shunt form a piezoelectric vibration absorber, which is used to control the time-averaged vibration of the suspended block mass. The system is thus studied with the lumped parameter model shown in Fig. 2.1(b), which is composed by a mass m_m in parallel with a damper

having damping coefficient c_m. The elastic effect of the piezoelectric element is described with an axial spring connected in parallel too. Assuming the piezoelectric transducer is in short circuit, the stiffness of the spring is given by $k_m^E = Y_{pe}^E A_{pe}/H_{pe}$, where Y_{pe}^E is the Young modulus of the piezoelectric material under constant electric field and A_{pe}, H_{pe} are the cross sectional area and height of the element. The electro-mechanical transduction effect of the piezoelectric element is modelled with a two port ideal transducer [112], which is schematised as a voltage-controlled ideal reactive force generator and a relative velocity-controlled ideal current generator, both characterised by the transduction coefficient $\psi_{pe} = d_{33} k_m^E$, where d_{33} is the strain/charge piezoelectric constant in direction 33 [113]. Therefore, the two transduction effects are governed by the following laws:

$$f_{pe} = \psi_{pe} v_s, \tag{2.1}$$

$$i_{pe} = \psi_{pe} \dot{x}_m, \tag{2.2}$$

where f_{pe} and i_{pe} are the force and current due to the shunt voltage v_s and block mass velocity $\dot{x}_m$ respectively. The piezoelectric transducer is also characterised by a capacitive effect, which is described with a capacitor connected in parallel with the transducer ideal current generator. Assuming the piezoelectric transducer is blocked, the capacitance is given by $C_{pe}^S = (\epsilon_{pe}^S A_{pe})/H_{pe}$ where $\epsilon_{pe}^S = \epsilon_{pe}^T (1 - k_{33}^2)$ is the permittivity of the piezoelectric material under constant strain [61], which is normally derived from measured data of the permittivity under constant stress ϵ_{pe}^T and the electromechanical coupling factor k_{33}^2 of the piezoelectric material (e.g. see Table 4.1 in Ref. [113]).

2.2.2 System equations of motion and state-space formulation

The electro-mechanical coupled response of this system can be derived applying Newton's law for the motion of the block mass and Kirchhoff law for the current flow in the electric mesh, which respectively give:

$$m_m \ddot{x}_m = -c\dot{x}_m - k_m^E x_m + \psi_{pe} \dot{\lambda}_s + f_m, \tag{2.3}$$

$$i_s = C_{pe}^S \ddot{\lambda}_s + \psi_{pe} \dot{x}_m, \tag{2.4}$$

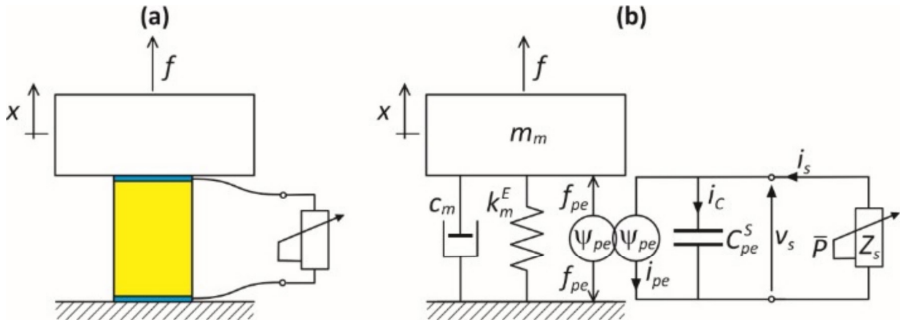

Figure 2.1: block mass mounted on a piezoelectric transducer connected to an adaptive shunt: a) scheme, b) lumped parameter model.

where i_s is the shunt current and λ_s is the shunt flux linkage, that is $\dot{\lambda}_s = v_s$ [113]. Also, using Kirchhoff voltage and current laws, the following equations are derived for the series and parallel RL-shunts respectively:

$$\dot{\lambda}_s = -R_s i_s - L_s \dot{i}_s, \tag{2.5}$$

$$i_s = -\frac{1}{R_s}\dot{\lambda}_s - \frac{1}{L_s}\lambda_s. \tag{2.6}$$

Here the minus sign in the right hand side of the two equations arises from the notation used for the shunt voltage, and thus flux linkage, and the shunt current variables. Note that the dot-notation is used for the derivation with respect to time, such that $\dot{x}_m = \frac{dx_m}{dt}$, $\dot{i}_s = \frac{di_s}{dt}$ and $\dot{\lambda}_s = \frac{d\lambda_s}{dt}$. Equations (2.3), (2.4) can be combined with either Eq. (2.5) or (2.6) to give the equation of motion in state-space form when the system is connected respectively to the RL-series or RL-parallel shunts. To start with, the system connected to the RL-series shunt is considered. Assuming the state variables are grouped in the state vector

$$\mathbf{y}_s = \begin{bmatrix} x_m \\ i_s \\ \dot{x}_m \\ \dot{i}_s \end{bmatrix}, \tag{2.7}$$

the first order differential equations are casted in the following matrix expression:

$$\dot{\mathbf{y}}_s = \mathbf{A}_s \mathbf{y}_s + \mathbf{B}_s f_m. \tag{2.8}$$

Here the state and input matrices are given by:

$$\mathbf{A}_s = \begin{bmatrix} 0 & 0 & 1 & 0 \\ 0 & 0 & 0 & 1 \\ -k_m^E/m_m & -(\psi_{pe}R_s)/m_m & -c_m/m_m & (-\psi_{pe}L_s)/m_m \\ 0 & -1/(C_{pe}^S L_s) & \psi_{pe}/(C_{pe}^S L_s) & -R_s/L_s \end{bmatrix}, \tag{2.9}$$

$$\mathbf{B}_s = \begin{bmatrix} 0 \\ 0 \\ 1/m_m \\ 0 \end{bmatrix}. \tag{2.10}$$

Alternatively, for the system connected to the parallel RL-shunt, collecting the state variables in the state vector

$$\mathbf{y}_s = \begin{bmatrix} x_m \\ \lambda_s \\ \dot{x}_m \\ \dot{\lambda}_s \end{bmatrix}, \tag{2.11}$$

the first order differential equations are casted in the following matrix expression:

$$\dot{\mathbf{y}}_p = \mathbf{A}_p \mathbf{y}_p + \mathbf{B}_p f_m. \tag{2.12}$$

In this case, the state and input matrices are given by:

$$\mathbf{A}_p = \begin{bmatrix} 0 & 0 & 1 & 0 \\ 0 & 0 & 0 & 1 \\ -k_m^E/m_m & 0 & -c_m/m_m & \psi_{pe}/m_m \\ 0 & -1/(C_{pe}^S L_s) & -\psi_{pe}/(C_{pe}^S) & -1/(C_{pe}^S R_s) \end{bmatrix}, \tag{2.13}$$

$$\mathbf{B}_p = \begin{bmatrix} 0 \\ 0 \\ 1/m_m \\ 0 \end{bmatrix}. \tag{2.14}$$

Assuming the excitation is a random force characterised by a white noise spectrum, the response of the system is evaluated with respect to the time-average of the kinetic energy of the system, that is

$$\bar{K}(R_s, L_s) = E[K(R_s, L_s, t)], \tag{2.15}$$

where $E[\,]$ is the expectation operator and the time-dependent kinetic energy is given by:

$$K(R_s, L_s, t) = \frac{1}{2} m_m \dot{x}_m^2. \tag{2.16}$$

The velocity of the mass can be retrieved directly from the state-space vectors y_s, y_p as follows

$$\dot{x}_m = \mathbf{C}_K \mathbf{y}_s, \tag{2.17}$$

$$\dot{x}_m = \mathbf{C}_K \mathbf{y}_p, \tag{2.18}$$

where the output matrix is given by:

$$\mathbf{C_K} = \begin{bmatrix} 0 & 0 & 1 & 0 \end{bmatrix}. \tag{2.19}$$

Therefore, the kinetic energy can be expressed as follows:

$$K(t) = \frac{1}{2} m_m \mathbf{y}_s^T \mathbf{C}_K^T \mathbf{C}_K \mathbf{y}_s = \frac{1}{2} m_m \mathbf{y}_p^T \mathbf{C}_K^T \mathbf{C}_K \mathbf{y}_p. \tag{2.20}$$

As will be discussed below, the tuning approach proposed in this thesis is based on the maximisation of the time-averaged electric power absorbed by the shunt

$$\bar{P}(R_s, L_s) = E[P(R_s, L_s, t)]. \tag{2.21}$$

Here, the time-dependent power absorbed by the shunt corresponds to the power dissipated by the shunt resistor, which, as highlighted in red in Fig. 2.2(a) and (b), in practice can be estimated for both shunts from the voltage drop across the shunt resistor v_R and the value of the shunt resistor itself R_s, i.e.:

$$P(R_s, L_s, t) = v_R i_R = \frac{1}{R_s} v_R^2. \tag{2.22}$$

For the simulations presented in this thesis, the above expression has been specified for the RL-series and RL-parallel shunts with reference to the shunt current and shunt voltage state-space variables respectively, such that:

$$P_{series}(R_s, L_s, t) = v_R i_s = R_s i_s^2, \tag{2.23}$$

$$P_{parallel}(R_s, L_s, t) = v_s i_R = \frac{1}{R_s} v_s^2 = \frac{1}{R_s} \dot{\lambda}_s^2. \tag{2.24}$$

Here $v_R = R_s i_s$ is the voltage across the resistor connected in series with the inductor and $i_R = v_s / R_s$ is the current through the resistor connected in parallel with the inductor. The shunt current and shunt voltage can be retrieved from the state-space vectors y_s, y_p with the following output expressions:

$$i_s = \mathbf{C}_i \mathbf{y}_s, \tag{2.25}$$

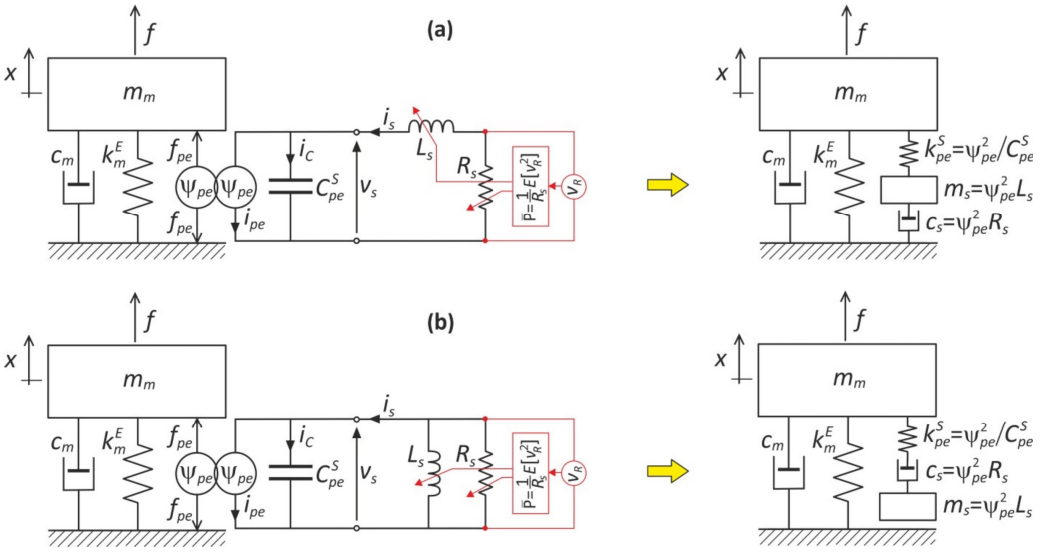

Figure 2.2: Equivalent mechanical models for (a) the series and (b) the parallel RL-shunts. Self-tuning arrangement highlighted in red.

$$v_s = \dot{\lambda}_s = \mathbf{C_v y_p}, \tag{2.26}$$

where the output matrices are given by:

$$\mathbf{C}_i = \begin{bmatrix} 0 & 1 & 0 & 0 \end{bmatrix}. \tag{2.27}$$

$$\mathbf{C}_v = \begin{bmatrix} 0 & 0 & 0 & 1 \end{bmatrix}. \tag{2.28}$$

Therefore, the power expressions in Eqs. (2.23), (2.24) can also be derived with respect to the state-vectors as follows:

$$P_{series}(R_s, L_s, t) = R_s \mathbf{y}_s^T \mathbf{C}_i^T \mathbf{C}_i \mathbf{y}_s. \tag{2.29}$$

$$P_{parallel}(R_s, L_s, t) = \frac{1}{R_s} \mathbf{y}_p^T \mathbf{C}_v^T \mathbf{C}_v \mathbf{y}_p. \tag{2.30}$$

2.2.3 Frequency domain formulation for spectral analysis

Assuming time-harmonic vibrations such that the mechanical (displacement, velocity, force) and electrical (current, voltage) functions take the

form $f(t) = \mathrm{Re}[f(\omega)\exp(j\omega t)]$, where $f(\omega)$ is the complex amplitude, ω is the circular frequency and $j = \sqrt{-1}$, Eqs. (2.3), (2.4) can be rewritten with reference to the complex amplitudes of the mechanical and electrical variables as follows

$$\Big(j\omega m_m + c_m + \frac{k_m^E}{j\omega}\Big)\dot{x}_m(\omega) - \psi_{pe} v_s(\omega) = f_m(\omega), \tag{2.31}$$

$$i_s(\omega) = j\omega C_{pe}^S v_s(\omega) + \psi_{pe}\dot{x}_m(\omega). \tag{2.32}$$

Here $\dot{x}_m(\omega)$, $f_m(\omega)$, $i_s(\omega)$, $v_s(\omega)$ are the complex amplitudes respectively of the block mass velocity and force and of the shunt current and voltage. The complex voltage across the shunt terminals is related to the complex current flow through the shunt terminals by the following impedance relation

$$v_s(\omega) = -Z_s(\omega) i_s(\omega), \tag{2.33}$$

where $Z_s(\omega)$ is exactly the impedance function of the shunt, which for the series and parallel RL shunts takes respectively the form

$$Z_s(\omega) = R_s + j\omega L_s, \tag{2.34}$$

$$Z_s(\omega) = \Big(\frac{1}{R_s} + \frac{1}{j\omega L_s}\Big)^{-1}. \tag{2.35}$$

Substitution of Eq. (2.32) into Eq. (2.33) gives

$$v_s(\omega) = -Z_{ps}(\omega)\psi_{pe}\dot{x}_m(\omega), \tag{2.36}$$

where the piezo-shunt impedance function can be retrieved from the following relation:

$$\frac{1}{Z_{ps}(\omega)} = \frac{1}{Z_s(\omega)} + \frac{1}{Z_{pe}^S(\omega)}. \tag{2.37}$$

Here $Z_{pe}^S(\omega) = \frac{1}{j\omega C_{pe}^S}$ is the electrical impedance of the piezoelectric transducer, which is characterised by the capacitive effect with reference to constant strain [112]. Also, $Z_s(\omega)$ is the electrical impedance of the series and parallel RL-shunts defined above. Eq. (2.37) can now readily substituted into Eq. (2.31) to give:

$$\big[Z_m(\omega) + \psi_{pe}^2 Z_p s(\omega)\big]\dot{x}_m(\omega) = f_m(\omega), \tag{2.38}$$

where the mechanical impedance of the mass-spring-damper system is given by:

$$Z_m(\omega) = j\omega m_m + c_m + \frac{k_m^E}{j\omega}. \tag{2.39}$$

The equivalent mechanical impedance effects produced by the piezoelectric transducer connected to the series and parallel RL-shunts are thus given respectively by:

$$\psi_{pe}^2 Z_p s(\omega) = \frac{\psi_{pe}^2}{\frac{1}{\frac{1}{j\omega C_{pe}^S}} + \frac{1}{R_s + j\omega L_s}} = \frac{1}{\frac{1}{\frac{k_{pe}^S}{j\omega}} + \frac{1}{c_s + j\omega m_s}} = k_{pe}^S \frac{\left(j\omega + \frac{c_s}{m_s}\right)}{\left(-\omega^2 + j\omega \frac{c_s}{m_s} + \frac{k_{pe}^S}{m_s}\right)}, \quad (2.40)$$

$$\psi_{pe}^2 Z_p s(\omega) = \frac{\psi_{pe}^2}{\frac{1}{\frac{1}{j\omega C_{pe}^S}} + \frac{1}{R_s} + \frac{1}{j\omega L_s}} = \frac{1}{\frac{1}{\frac{k_{pe}^S}{j\omega}} + \frac{1}{c_s} + \frac{1}{j\omega m_s}} = k_{pe}^S \frac{\left(j\omega\right)}{\left(-\omega^2 + j\omega \frac{c_s}{m_s} + \frac{k_{pe}^S}{m_s}\right)}. \quad (2.41)$$

These expressions suggest that, as discussed in Refs. [72], [80], [82] and shown schematically in Fig. 2.2, the series RL-shunt produces an equivalent mechanical impedance effect given by a spring $k_{pe}^S = \frac{\psi_{pe}^2}{C_{pe}^S}$ in series with a damper $c_s = \psi_{pe}^2 R_s$ and mass $m_s = \psi_{pe}^2 L_s$ connected in parallel. Alternatively, the parallel RL-shunt generates an equivalent mechanical impedance effect given by the spring $k_{pe}^S = \frac{\psi_{pe}^2}{C_{pe}^S}$, damper $c_s = \psi_{pe}^2 R_s$ and mass $m_s = \psi_{pe}^2 L_s$ connected in series. At this point, the complex amplitude of the velocity response of the system with respect to the complex amplitude of the force excitation can be readily derived from Eq. (2.38) in terms of the following mobility expression

$$\dot{x}_m(\omega) = Y(\omega) f_m(\omega), \quad (2.42)$$

where the mobility function is given by

$$Y(\omega) = \frac{1}{\left[Z_m(\omega) + \psi_{pe}^2 Z_p s(\omega)\right]}. \quad (2.43)$$

This mobility function can be specified for the series and parallel RL-shunts with second order polynomial expressions in ω for the mechanical and shunt electro-mechanical effects:

$$Y_s(\omega) = \frac{j\omega(-\omega^2 + j\omega 2\xi_s\omega_s + \omega_s^2)}{m_m}\Big[(-\omega^2 + j\omega 2\xi_m\omega_m + \omega_m^2)(-\omega^2 + j\omega 2\xi_s\omega_s + \omega_s^2) + \frac{k_{pe}^S}{m_m}(-\omega^2 + j\omega\Omega_s)\Big]^{-1}, \quad (2.44)$$

$$Y_p(\omega) = \frac{1}{m_m} \frac{j\omega(-\omega^2 + j\omega 2\xi_p\omega_p + \omega_p^2)}{\left[(-\omega^2 + j2\xi_m\omega\omega_m + \omega_m^2)(-\omega^2 + j\omega 2\xi_p\omega_p r + \omega_p^2) + \frac{k_{pe}^S}{m_m}\right]}, \quad (2.45)$$

Here, $\omega_m = \sqrt{\frac{k_m}{m_m}}$ and $\xi_m = \frac{c_m}{2\sqrt{k_m/m_m}}$ are the natural frequency and damping ratio of the mechanical system. Also, $\omega_s = \sqrt{\frac{k_{pe}^S}{m_m}} = \frac{1}{\sqrt{L_s C_{pe}^S}}$, $\xi_s = \frac{c_s}{2\sqrt{k_{pe}^S m_s}} = \frac{R_s}{2}\sqrt{\frac{C_{pe}^S}{L_s}}$, $\Omega_s = \frac{c_s}{m_s} = \frac{R_s}{L_s}$ are the natural frequency, the damping ratio and the resistive-inductive cut-off frequency of the piezoelectric transducer connected to the series RL-shunt. Finally, $\omega_p = \sqrt{\frac{k_{pe}^S}{m_s}} = \frac{1}{\sqrt{L_s C_{pe}^S}}$, $\xi_p = \frac{(m_s k_{pe}^S)/c_s}{2\sqrt{k_{pe}^S m_s}} = \frac{1}{2R_s}\sqrt{\frac{L_s}{C_{pe}^S}}$ are the natural frequency and damping ratio of the piezoelectric transducer connected to the parallel RL-shunt. At this point, the time-averaged kinetic energy and the time-averaged electric power dissipated by shunt resistor can be readily derived recalling that

$$\bar{K}(R_s, L_s) = \frac{1}{2\pi}\int_{\infty}^{+\infty} S_K(R_s, L_s, \omega)d\omega, \quad (2.46)$$

$$\bar{P}(R_s, L_s) = \frac{1}{2\pi}\int_{\infty}^{+\infty} S_P(R_s, L_s, \omega)d\omega, \quad (2.47)$$

where $S_K(\omega)$ is the Power Spectral Density (PSD) of the kinetic energy function and $S_P(\omega)$ is the PSD of the electric power dissipated by the shunt resistor. The PSD of the kinetic energy is given by

$$S_K(R_s, L_s, \omega) = \frac{1}{2} m_m \lim_{T\to\infty} E\left[\frac{1}{T}\dot{x}_m^*(\omega)\dot{x}_m(\omega)\right], \quad (2.48)$$

where $E[\ ]$ is the expectation operator, $(\ )^*$ is the complex conjugate operator and T is the length of the time function $\dot{x}(t)$ having Fourier Transform $\dot{x}_m(\omega)$ [114]. Substituting Eq. (2.42) into Eq. (2.48) leads to

$$S_K(R_s, L_s, \omega) = \frac{1}{2} m_m |Y(\omega)|^2 S_{ff}(\omega), \quad (2.49)$$

where $S_{ff}(\omega)$ is the PSD of the force excitation:

$$S_{ff}(R_s, L_s, \omega) = \lim_{T\to\infty} E\left[\frac{1}{T} f_m^*(\omega) f_m(\omega)\right]. \quad (2.50)$$

In parallel, according to Eqs. (2.22), (2.23), the PSD of the electric power dissipated by the resistor in the series and parallel RL-shunts is given by the following expressions

$$S_P(R_s, L_s, \omega) = -R_s \lim_{T\to\infty} E\left[\frac{1}{T} i_s^*(\omega) i_s(\omega)\right], \tag{2.51}$$

$$S_P(R_s, L_s, \omega) = -\frac{1}{R_s} \lim_{T\to\infty} E\left[\frac{1}{T} v_s^*(\omega) v_s(\omega)\right] \tag{2.52}$$

Here, recalling Eqs. (2.33), (2.36), (2.37), (2.42), the complex amplitude of the current through the series RL-shunt is given by

$$i_s(\omega) = G_{if}(\omega) f_m(\omega), \tag{2.53}$$

whereas, the complex amplitude of the voltage across the shunt is given by

$$v_s(\omega) = -G_{vf}(\omega) f_m(\omega). \tag{2.54}$$

In these expressions

$$G_{if}(\omega) = \frac{Z_{pe}^S(\omega)\psi_{pe}Y(\omega)}{Z_{pe}^S(\omega) + Z_s(\omega)}, \tag{2.55}$$

and

$$G_{vf}(\omega) = \frac{Z_{pe}^S(\omega)Z_s(\omega)\psi_{pe}Y(\omega)}{Z_{pe}^S(\omega) + Z_s(\omega)}. \tag{2.56}$$

Therefore, the PSD of the electric power dissipated by the resistor in the series and parallel RL-shunts given in Eqs. (2.51), (2.52) result

$$S_P(R_s, L_s, \omega) = -R_s |G_{if}(\omega)|^2 S_{ff}(\omega), \tag{2.57}$$

$$S_P(R_s, L_s, \omega) = -\frac{1}{R_s} |G_{vf}(\omega)|^2 S_{ff}(\omega). \tag{2.58}$$

2.3 RL-maps and optimal tuning

The effectiveness of the proposed tuning strategy based on the maximisation of the time-average electric power absorbed by the shunt $\bar{P}$ is investigated in this section with respect to the time-averaged kinetic energy of the SDOF system $\bar{K}$, which gives the effective response of the mechanical

Table 2.1: Electro-mechanical properties of the system depicted in Fig. 2.1

Property	**Value**
Seismic mass	$m_m = 3,79$ kg
Damping coefficient	$c_m = 16,85$ Ns/m
Short circuit transducer stiffness	$k_m^E = 1,17 \times 10^6$ N/m
Piezoelectric transduction coefficient	$\psi_{pe} = 89,4 \times 10^{-3}$ N/V, As/m
Blocked transducer capacitance	$C_{pe}^S = 501$ nF

system and shunted piezoelectric vibration absorber. To this end, for both RL-series and RL-parallel shunts, the plots with RL-maps of $\bar{K}(R_s, L_s)$ and $\bar{P}(R_s, L_s)$ are first presented. Hence, waterfall spectra are introduced with the SDOF system kinetic energy PSD, $S_K(R_s, L_s, \omega)$, and shunt absorbed power PSD, $S_P(R_s, L_s, \omega)$ calculated considering the intermediated values of the resistance R_s and inductance L_s that would be implemented in the shunts to move from arbitrary initial values $(R_{(s,ini)}, L_{(s,ini)})$ to the optimal values $(R_{(s,opt)}, L_{(s,opt)})$ with the proposed two-paths tuning strategy. The analysis considers the system depicted in Fig. 2.1 is characterised by the physical parameters summarised in Table 1.

2.3.1 RL-series

The SDOF mechanical system with piezoelectric transducer connected to the RL-series shunt is considered first. Fig. 2.3(a) shows that the map of the time-averaged kinetic energy of the SDOF system, $\bar{K}(R_s, L_s)$, is characterised by a non-convex inverse bell-shape with a single minimum point. Instead, Fig. 2.3(b) shows that the map of the time-averaged power absorbed by the shunt, $\bar{P}(R_s, L_s)$, is given by a mirror non-convex bell-shape with a single maximum point. As highlighted by the cross and circle markers, the points where $\bar{K}(R_s, L_s)$ is minimum and $\bar{P}(R_s, L_s)$ is maximum overlap. Therefore, it can be concluded that the time-averaged response of the SDOF mechanical system connected to the shunted piezoelectric vibration absorber can be effectively attenuated by setting the optimal shunt resistance $R_{(s,opt)}$ and inductance $L_{(s,opt)}$ to maximise the time-averaged electric power absorbed by the shunt. A close inspection of the two plots suggests that the two maps are characterised by two principal directions defined by $R_s = \text{const}$ and $L_s = \text{const}$. Therefore, a two-paths climb strategy is proposed to find independently the optimal resistance $R_{(s,opt)}$ and the optimal inductance $L_{(s,opt)}$ of the shunt, which maximises $\bar{P}(R_s, L_s)$ and thus minimises $\bar{K}(R_s, L_s)$. For instance, the map in Fig. 2.3(b) shows the two paths, which, starting from arbitrary initial

values $(R_{(s,ini)}, L_{(s,ini)})$, first lead to a value close to the optimal inductance, i.e. $(R_{(s,ini)}, L_{(s,ini)}) \rightarrow (R_{(s,ini)},\ L_{(s,opt)})$, and then get to a value close to the optimal resistance, i.e. $(R_{(s,ini)},\ L_{(s,opt)}) \rightarrow (\ R_{(s,opt)},\ L_{(s,opt)})$. As will be discussed in the forthcoming section, this two-paths optimisation search can be conveniently implemented iteratively with an extremum seeking gradient search algorithm, which effectively finds the maxima of the $R_s = \text{const}$ and $L_s = \text{const}$ non-convex paths. The two maps in Fig. 2.3 suggest that single climbs along $R_s = \text{const}$ and $L_s = \text{const}$ are sufficient to get to a point close to the optimal inductance $L_{(s,opt)}$ and resistance $R_{(s,opt)}$ of the shunt. Actually, the bell shaped power cost function is quite flat in the vicinity of the peak value and thus the time-averaged power absorbed by the shunt and the time-averaged kinetic energy of the system when the shunt implements the resistance and inductance found with the two climbs is very close to the maximum value and minimum value possible respectively.

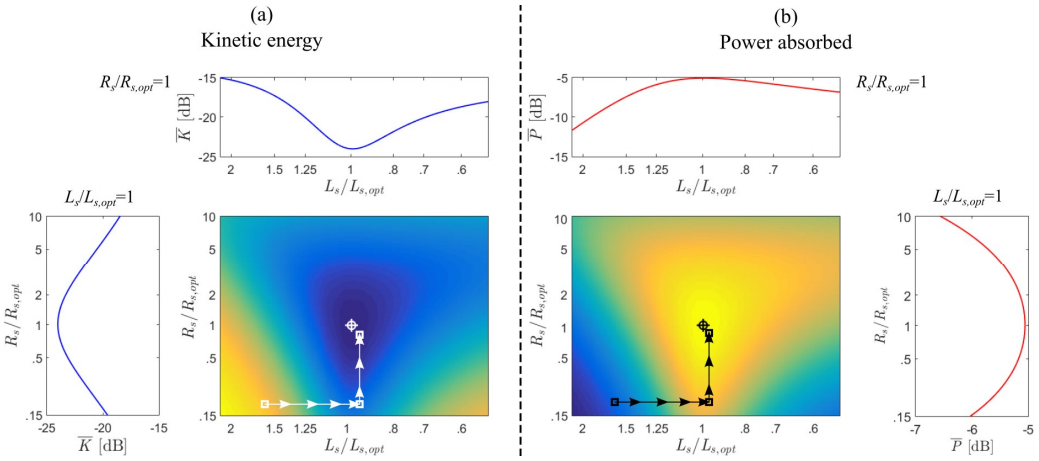

Figure 2.3: RL-series shunt. Maps of $\bar{K}(R_s, L_s)$ (a) and $\bar{P}(R_s, L_s)$ (b). Lateral plots: maps slice for L_{opt}. Top plots: maps slice for R_{opt}. Lines with arrows indicate (1) the $R_i, L_i \rightarrow L_{\text{opt}}$ and (2) the $R_i \rightarrow R_{\text{opt}}, L_{\text{opt}}$ tuning paths. Cross marker $\min(\bar{K})$. Circular marker $\max(\bar{P})$.

The two waterfall plots in Fig. 2.4 show that, when the shunt is mistuned, i.e. $R_s = R_{(s,ini)}, L_s = L_{(s,ini)}$, the spectra of the kinetic energy PSD, $S_K(\omega)$, and absorbed power PSD, $S_P(\omega)$, highlighted by the thick black lines are characterised by a single resonance peak, centred at about ω_m. Then, as the inductance is raised towards the optimal value $L_{(s,opt)}$, a second peak with increasingly larger resonance frequency $\omega_2 < \omega_m$ progressively grows whereas the former first peak progressively moves to higher frequencies

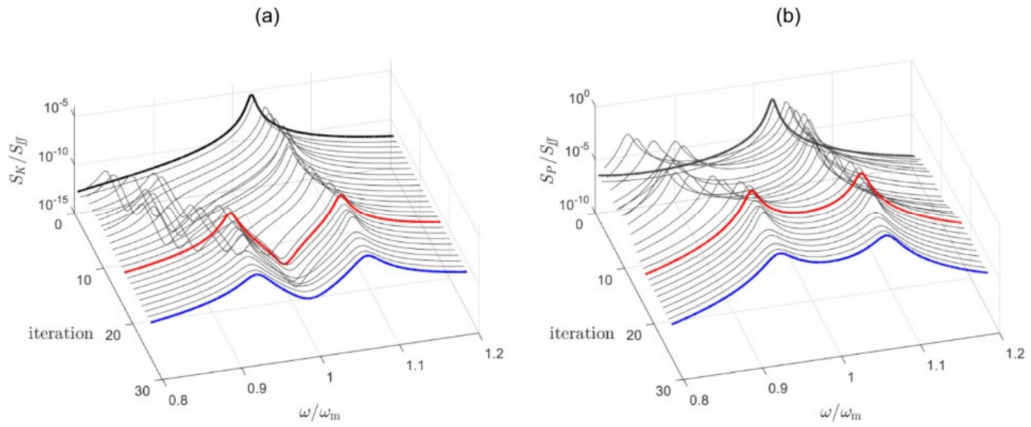

Figure 2.4: RL-series shunt. Waterfall spectra of (a) $S_K(\omega)$ and (b) $S_P(\omega)$ for the shunt resistance and inductance values of the optimisation paths (1) and (2) highlighted in Fig 2.3. Thick-black spectra $R = R_i, L = L_i$. Thick-blue spectra $R = R_i, L = L_{\text{opt}}$. Thick-red spectra $R = R_{\text{opt}}, L = L_{\text{opt}}$.

$\omega_1 > \omega_m$. The thick blue spectra show that, when a value close to $L_{(s,opt)}$ is reached, both $S_K(\omega)$ and $S_P(\omega)$ are characterised by two marked peaks. At this point, as the shunt resistance is raised towards its optimum value $R_{(s,opt)}$, the two peaks in the $S_K(\omega)$ and $S_P(\omega)$ spectra are progressively rounded and broadened. Overall, the vibration response of the mechanical system is significantly lessened whereas the electric power absorbed, and thus dissipated, by the shunt is further increased to a maximum value.

2.3.2 RL-parallel

The SDOF mechanical system with the piezoelectric transducer connected to the RL-parallel shunt is considered next. In this case too, the plots in Fig. 2.5 show that the maps of $\bar{K}(R_s, L_s)$ and $\bar{P}(R_s, L_s)$ are characterised respectively by a non-convex inverse bell-shape with a single minimum point and a mirror non-convex bell-shape with a single maximum point. Yet again, the cross and circle markers, indicate that the points where $\bar{K}(R_s, L_s)$ is minimum and $\bar{P}(R_s, L_s)$ is maximum overlap. Therefore, for the RL-parallel shunt too, the time-averaged response of the SDOF mechanical system connected to the shunted piezoelectric vibration absorber and excited by a stochastic force can be effectively attenuated by setting the shunt resistance and shunt inductance to maximise the time-averaged electric power absorbed by the

shunt itself. As observed for the series RL-shunt, the two maps in Fig. 2.5 are characterised by principal directions $R_s = \text{const}$ and $L_s = \text{const}$. Hence, the two-paths tuning strategy proposed above for the RL-series shunt can be adopted in the RL-parallel shunt too. For example, the two bell-shaped non-convex paths highlighted in Fig. 2.5(b) can be climbed in sequence with an extremum seeking gradient search algorithm, first to find the optimal inductance, $L_{(s,opt)}$, and then to find the optimal resistance, $R_{(s,opt)}$. The two maps, indicate that in this case, after single climbs along $R_s = \text{const}$ and $L_s = \text{const}$ the values identified for the shunt inductance and resistance practically correspond to the optimal ones $L_{(s,opt)}$ and $R_{(s,opt)}$.

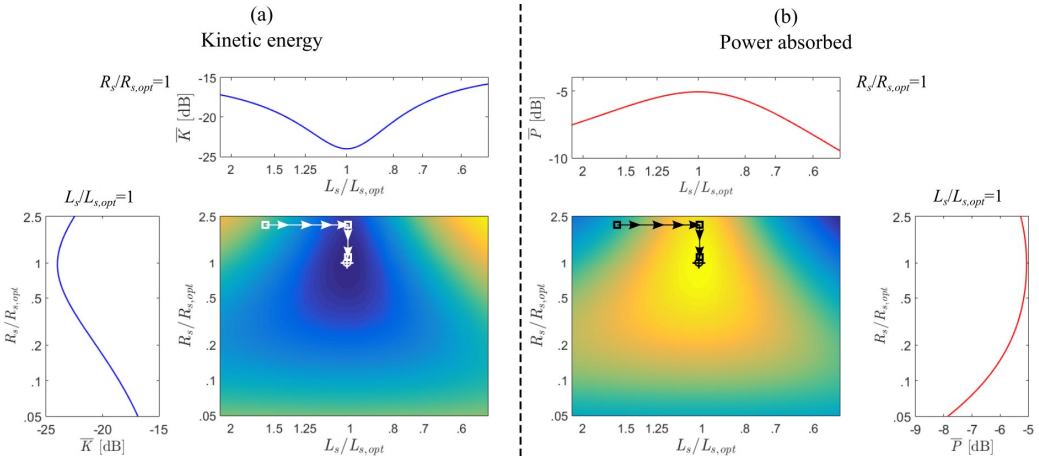

Figure 2.5: RL-parallel shunt. Maps of $\bar{K}(R_s, L_s)$ (a) and $\bar{P}(R_s, L_s)$ (b). Lateral plots: maps slice for L_{opt}. Top plots: maps slice for R_{opt}. Lines with arrows indicate (1) the $R_i, L_i \rightarrow L_{\text{opt}}$ and (2) the $R_i \rightarrow R_{\text{opt}}$, L_{opt} tuning paths. Cross marker $\min(\bar{K})$. Circle marker $\max(\bar{P})$.

The waterfall plots in Fig. 2.6 show that, as seen above for the series RL-shunt, when the RL-parallel shunt is mistuned, i.e. $R_s = R_{(s,ini)}, L_s = L_{(s,ini)}$, the spectra of the kinetic energy PSD, $S_K(\omega)$, and absorbed power PSD, $S_P(\omega)$, highlighted by the thick black lines are characterised by a single resonance peak, centred at about ω_m. However, in this case, when the inductance is raised towards the optimal value $L_{(s,opt)}$, a second peak arises at progressively smaller resonance frequencies $\omega_2 > \omega_m$ whereas the initial peak progressively moves to lower frequencies $\omega_1 < \omega_m$. The thick blue spectra show that, when $L_{(s,opt)}$ is reached, both $S_K(\omega)$ and $S_P(\omega)$ are characterised by a pair of neighbour peaks, which are then rounded off and broadened as the shunt resistance is raised towards its optimum value $R_{(s,opt)}$. Overall,

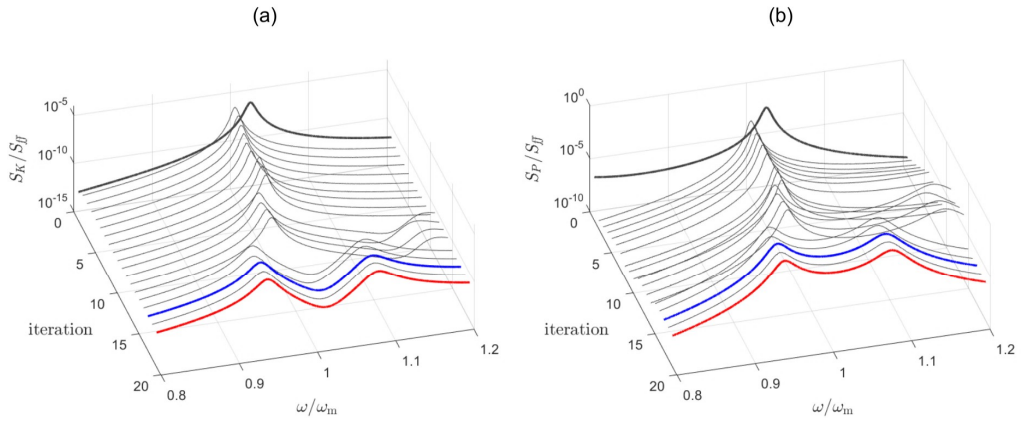

Figure 2.6: RL-parallel shunt. Waterfall spectra of (a) $S_K(\omega)$ and (b) $S_P(\omega)$ for the shunt resistance and inductance values of the optimisation paths (1) and (2) highlighted in Fig. 2.3. Thick-black spectra $R = R_i, L = L_i$. Thick-blue spectra $R = R_i, L = L_{\text{opt}}$. Thick-red spectra $R = R_{\text{opt}}, L = L_{\text{opt}}$.

the RL-parallel shunt too generates a substantial reduction of the vibration response of the mechanical system accompanied by a significant increment of the electric power absorbed, and thus dissipated, by the shunt.

2.4 Self-tuning algorithm: convergence analysis

The online system to tune the shunts featured in this study is based on an extremum seeking gradient search algorithm [105] specifically tailored to the electric power absorption objective function proposed in this thesis, which is characterised by a non-convex bell-shape with a single maximum. More specifically, as discussed in the previous section and depicted in the flow-chart of Fig. 2.7, the tuning is based on a two-paths search, where considering initial values of the shunt components $R_{(s,ini)}, L_{(s,ini)}$ the search is carried out in two phases:

1. The optimal inductance $L_{(s,opt)}$ is pursued along the path $R_s = R_{(s,ini)}$ starting from $L_{(s,ini)}$;
2. The optimal resistance $R_{(s,opt)}$ is searched along the path $L_s = L_{(s,opt)}$ starting from $R_{(s,ini)}$.

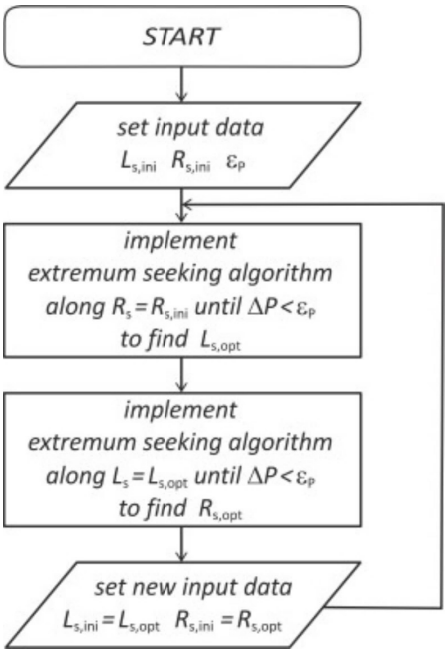

Figure 2.7: Flow chart of the proposed tuning approach

As shown above, the cost function based on the maximisation of the time-averaged electric power absorbed by each branch of the shunts is characterised by a bell-type non-convex surface with respect to the inductance and resistance shunt parameters, which actually define principal directions to search for the maximum of the power cost function. Hence, the tuning can be run independently along constant-resistance and constant-inductance paths, which, in turn, are characterised by bell-shaped curves with respect to the resistance and inductance parameters respectively. Since these cost functions are characterised by non-convex curves, in this study the search for the maximum is implemented along the two tuning paths with an extremum seeking algorithm [103]–[107], whose operation principle is illustrated here considering the tuning of the inductance parameter as depicted in the block diagram in Figure 2.8.

The extremum seeking algorithm is a perturb-and-see algorithm [103], which, relies on a ripple signal that modifies the tuning variable, thus creating a ripple on the output cost function signal too, that is on the electric power absorbed by the shunt. For simplicity, as depicted in the block diagram in Figure 2.8, the implementation of the tuning of the shunt inductance is described here. As anticipated before, the algorithm employs a time-harmonic ripple signal

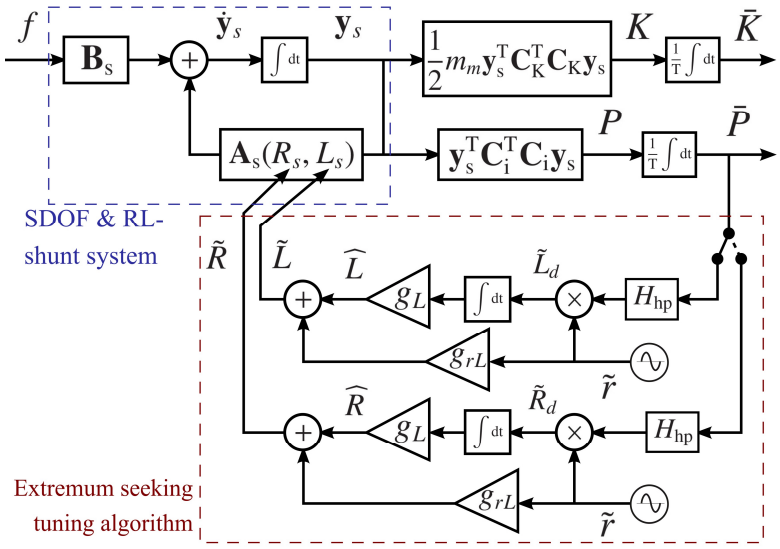

Figure 2.8: Block diagram of the State-Space model for the SDOF system with the extremum seeking gradient search feedback control loop for the online tuning of the series shunt resistance R_s and inductance L_s.

$$\tilde{r}(t) = r_0 \sin(\omega_L t), \tag{2.59}$$

with amplitude r_0 and circular frequency ω_L, which is chosen much smaller than the lower frequency of operation of the shunted piezoelectric patch. This signal is amplified by a gain g_{rL} and then added to the tuning inductance signal $\widehat{L}$. As depicted in Figure 2.9, the resulting signal is thus characterised by the off-set tuning signal $\widehat{L}$ and the magnified time-harmonic ripple $\tilde{r} g_r L$, that is

$$\tilde{L}(t) = \widehat{L}(t) + g_{rL} r_0 \sin(\omega_L t), \tag{2.60}$$

The wavy tuning inductance generates an equivalent ripple on the electric power absorbed by the shunt, which can then be defined as the sum of two power terms as well:

$$P = \widehat{P} + \tilde{P}. \tag{2.61}$$

The first term, $\widehat{P}$, is the absorbed power due to the $\widehat{L}$ tuning component whereas the second term $\tilde{P} = \sigma_P g_{rL} \tilde{r}$ encompasses the ripple signal whose amplitude is scaled by a factor σ_P. In this way, yet the extremum seeking algorithm can be implemented to find the maximum of the time-average

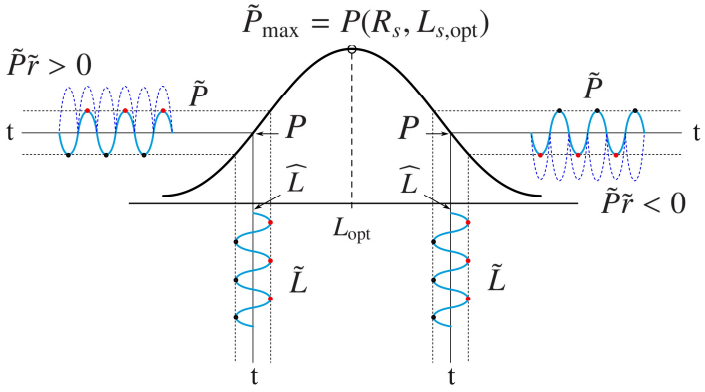

Figure 2.9: Extremum seeking working principle for the tuning of the shunt inductance

electric power absorbed by the shunt. As can be noticed in Figure 2.9, when $\widehat{L} < L_{\text{opt}}$ the wavy time-averaged power signal $\tilde{P}$ and the wavy tuning signal $\tilde{r}(t)$ are bound to be in-phase (i.e. $\sigma_P > 0$), whereas when $\widehat{L} > L_{\text{opt}}$ they are bound to be out-of-phase (i.e. $\sigma_P < 0$). Therefore, to identify whether the inductance signal $\widehat{L}$ is higher or lower than the optimal value L_{opt}, it is sufficient to check the relative phase of the harmonic components of $\tilde{P}$ and $\tilde{r}$. As depicted in the block diagram of Figure 2.8, the harmonic signal $\tilde{P}$ can be extracted from the electric power signal $\bar{P}$ with a high pass filter

$$H_{\text{hp}}(j\omega) = \frac{j\omega}{j\omega + \omega_{\text{hp}}}, \tag{2.62}$$

having very low cut-off frequency ω_{hp}. To compare the phase of $\tilde{r}$ and $\tilde{P}$ the two signals are then multiplied, to give a wavy tuning signal:

$$\tilde{L}_d(t) = \tilde{P}\tilde{r}. \tag{2.63}$$

As highlighted in Figure 2.9, when the two harmonic signals $\tilde{P}$ and $\tilde{r}$ are in-phase their product will be mostly positive, i.e., $\tilde{L}_d > 0$, whereas when they are out-of-phase it will be mostly negative, i.e., $\tilde{L}_d < 0$. At this point, to generate a suitable tuning signal $\widehat{L}$, the wavy signal $\tilde{L}_d$ should be rectified. Therefore, the $\tilde{L}_d$ signal is integrated and magnified such that

$$\widehat{L} = g_L \int_T \tilde{L}_d dt. \tag{2.64}$$

In conclusion, the resulting tuning signal will tend to rise when $\widehat{L}(t) < L_{s,\mathrm{opt}}(t)$ and tend to decrease when $\widehat{L}(t) > L_{s,\mathrm{opt}}(t)$. In fact, the rate with which the $\widehat{L}(t)$ signal increases or decreases is proportional to the gradient of the objective function signal $P(t)$. The gain g_L dictates the speed of convergence of the algorithm, although to avoid instability its value should be carefully chosen [108]. In summary, as highlighted in Figure 2.8, the extremum seeking algorithm is characterised by three blocks: first the modulation block where the tuning signal is modulated by the ripple signal and then the demodulation and parameter update blocks where the wavy electric power signal is demodulated and rectified in such a way as to have the tuning signal. The tuning of the resistance is based exactly on the same type of algorithm, which is therefore not described in detail here. This perturb-and-observe algorithm adapts asymptotically the inductance and resistance to their optimal values. Therefore, when the algorithm has converged, the shunt resistance and inductance will tend to oscillate indefinitely around the optimal values. The implementation of the algorithm is fairly straightforward, but requires a careful choice of the frequency ω_L and amplitude r_0 of the dithering signal $\tilde{r}(t)$; the cut-off frequency ω_{hp} and the gains g_{zL} , g_{zR} , g_L and g_R. Because of this exclusive dependence on the ripple signal and output electric power signal, the optimisation (maximisation) is not dependent on an explicit model of the system. Thus, the proposed self-tuning shunted piezoelectric vibration absorber can track the changes in the flexural response of the hosting structures, due for example to variations of temperature or to variations of the operation conditions, which would affect both the mechanical response of the structure, the electro-mechanical response of the piezoelectric patches and the electrical response of the shunts. The self-tuning algorithm proposed in this study can effectively track these changes and maximise the control effect in a wide range of operation conditions.

The search in each path is stopped once the variation of the time-averaged absorbed power is smaller than a predefined threshold ϵ_P As described in the lateral and top plots of Fig. 2.3(b) and 2.5(b), both paths are characterised by non-convex bell-shaped curves with single maxima, which, as discussed in Section 2.2, identify values close to $L_{(s,opt)}$ and $R_{(s,opt)}$ respectively. As depicted in the flow chart, the initial search is repeated online by setting at the beginning of each iteration $R_{(s,ini)} = R_{(s,opt)}$ and $L_{(s,ini)} = L_{(s,opt)}$. In this way, the effective optimal shunt inductance and resistance are identified.

Nevertheless, as will be shown in the forthcoming sub-sections, the combination of the proposed time-averaged absorbed electric power objective function and extremum seeking gradient search adaptive control algorithm gives a powerful approach for the tuning of the resistive and inductive com-

ponents of the RL-series and RL-parallel shunts. The forthcoming two sub-sections present numerical simulations on the real-time implementation of the proposed tuning approach. For this analysis, the random force excitation is actually passed through a high-pass filter, with low cut-off frequency at 5 Hz, and a low-pass filter, with cut-off frequency 10 times higher than the mechanical natural frequency of the SDOF system. The high-pass filter cuts the steady-state component of the random excitation whereas the low-pass filter cuts the higher frequencies spectral component of the excitation to facilitate the convergence of the algorithm that integrates the first-order differential equations of the state-space model of the system.

2.4.1 RL-series

To start with, the real-time implementation of the RL-series shunt is analysed here. Fig.s 2.10 and 2.11 show three time-histories taken during the implementation of the two-paths extremum seeking gradient search algorithm proposed above to tune the shunt inductance and resistance in sequence. More specifically, Figure 2.10 shows: (a) the stochastic force excitation, (b) the velocity of the black mass, which gives an indication of the response of the mechanical system, and (c) the shunt voltage, which gives an indication of the electrical power absorbed by the shunt. In parallel, Fig. 2.11 shows the time-histories of the mechanical system kinetic energy, (b) electric power absorbed by the shunt and (c) shunt inductance and shunt resistance.

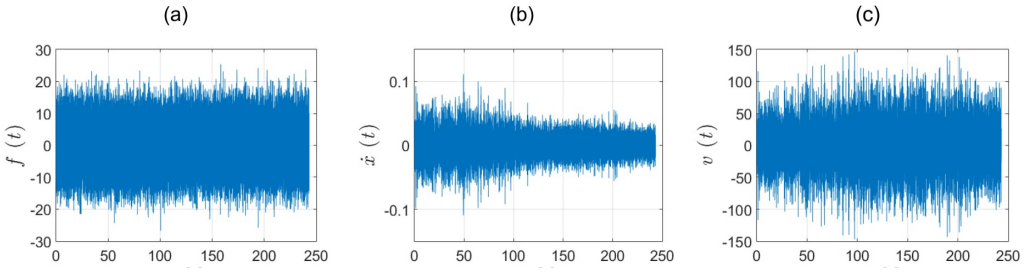

Figure 2.10: Time-histories of (a) the force excitation, (b) block mass velocity and (c) shunt voltage when the proposed tuning algorithm is implemented on the RL-series shunt.

Considering first the plots in Fig. 2.10, the velocity graph shows that, as the algorithm is implemented, the amplitude of the velocity nearly halves whereas the amplitude of the shunt voltage nearly doubles. Moving to Fig. 2.11, plots (a) and (b) indicate that initially, during the inductance tuning

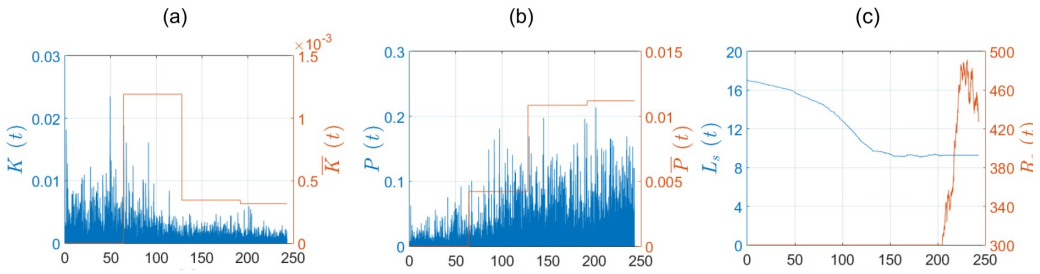

Figure 2.11: Time-histories of (a) the instantaneous kinetic energy (orange broken line time-averaged value), (b) instantaneous electric power absorbed by the shunt (orange broken line time-averaged value) and (c) the shunt inductance (blue line) and resistance (red line) as the proposed tuning algorithm is implemented on the RL-series shunt.

phase, the kinetic energy of the system is steady while the power absorbed from the mechanical system increases slightly. The average values in these plots refer to the previous window. Thus, the increase seen in the time average of the kinetic energy on Fig. 2.11(a) is referred to the initial state, as well as the small value in the time average of the electric power. Nevertheless, after about 80 seconds there is a marked decrement of the system kinetic energy, which then continues to fall until the optimal inductance is reached within the imposed tolerance τ. The following tuning of the resistance requires a single step, which produces a negligible reduction of the kinetic energy of the system anyhow. This is related to the fact that, as shown on the lateral and top plots in Fig. 2.3(b), the tuning path $L_s = \text{const}$ to find the optimal resistance is, comparatively, much flatter than the tuning path $R_s = \text{const}$ to find the optimal inductance. Indeed, the map of the time-averaged electrical power absorbed by the shunt is characterised by a bell-shape squeezed along the horizontal constant resistance. Thus, a faster convergence is achieved because of the threshold criterion on the absorbed power.

2.4.2 RL-parallel

The real-time implementation of the RL-parallel shunt is now investigated with respect to the results presented in Figs. 2.12 and 2.13, which have the same layout as Figs. 2.10 and 2.11 presented above for the RL-series shunt. The velocity graph in Fig. 2.12(b) shows that, as the shunt is tuned, the amplitude of the velocity nearly halves in the first 120 s. Also, Fig. 2.12(c) indicates that the shunt voltage grows with the bigger increase on the initial

100 seconds and remains about even throughout the following iterations.

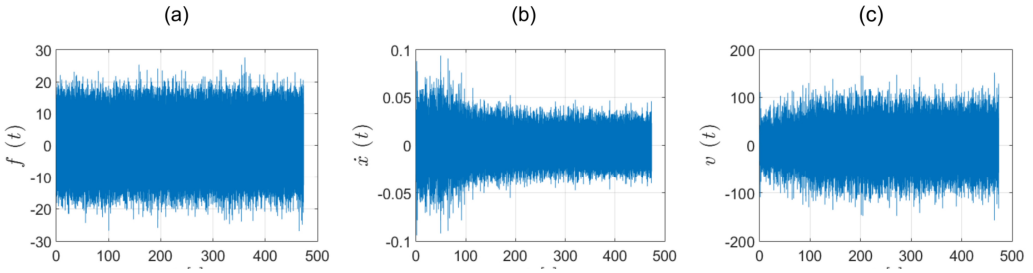

Figure 2.12: Time-histories of (a) the force excitation, (b) block mass velocity and (c) shunt voltage when the proposed tuning algorithm is implemented on the RL-parallel shunt.

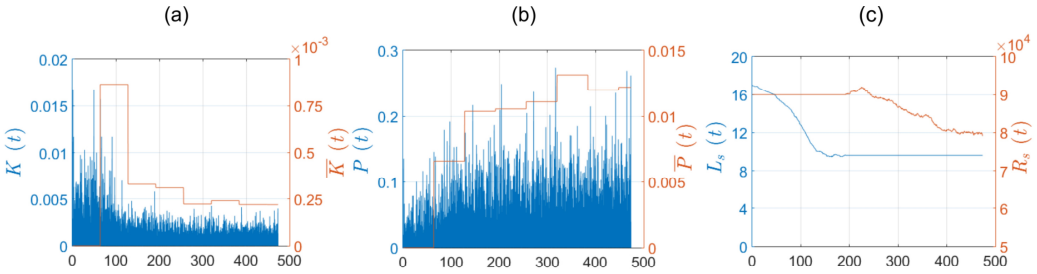

Figure 2.13: Time-histories of (a) the instantaneous kinetic energy (orange broken line time-averaged value), (b) instantaneous electric power absorbed by the shunt (orange broken line time-averaged value) and (c) the shunt inductance (blue line) and resistance (red line) as the proposed tuning algorithm is implemented on the RL-parallel shunt.

Moving to Fig. 2.13, Plots (a) and (b) show that, with this shunt too, the kinetic energy initially increases. Nevertheless, from 50 to 200 seconds of the inductance tuning phase, the kinetic energy falls significantly in front of substantial increments of the electric power absorbed by the shunt. Besides, as seen for the RL-series shunt, in the remaining part of the tuning between 200 and 500 s, a comparatively smaller additional reduction of the system kinetic energy is noticed despite the longer time available. This effect can be explained with the side plot on Fig. 2.5(b). Unlike the RL-series configuration, the RL-parallel does have a larger variation on the power absorbed by the shunt on the tuning path $L_s = \text{const}$. Thus, a longer time will be required for the control to achieve the stop conditions.

The results presented in this and previous subsections are based on a random disturbance, which is thus characterised by quite an uneven time history. In practice, stochastic disturbances are normally smoother (smaller standard deviation, bandlimited, etc...) and thus it is expected that the time-frame to tune the two components of the shunt could be much shorter that that found in the simulations presented herein.

Chapter 3

Piezoelectric patch vibration control units connected to a single-resonant self tuning shunt

3.1 Introduction

This chapter investigates the practical implementation of the self tuning shunted piezoelectric units introduced in the previous chapter considering the flexural vibrations of a simple model structure. More specifically, it presents a simulation and experimental study on the control of the resonant response of a target low-order flexural mode of a thin panel structure equipped with five self-tuning vibration absorbers formed by a piezoelectric patch connected to a tuneable shunt composed by a resistor and inductor connected in parallel (RL-shunt). The two-paths online tuning approach proposed in the previous chapter is employed, where the inductance and resistance of the shunts are tuned sequentially with an extremum seeking gradient search algorithm [103], [107], [115], [116] in such a way as to maximise the time-averaged electric power absorption from the resonant response of the target low-order flexural mode of the panel.

3.1.1 Modular self tuning single-resonant shunt for piezoelectric vibration control units

In this chapter, the practical implementation of systems composed by a piezoelectric patch connected to a self-tuning shunt is thus investigated in

details. The ultimate goal of this work is to devise self-contained, compact and lightweight vibration control units, which can be bonded in batches on thin-walled lightweight structures. Each unit can then be set to control the resonant response of a distinct low-order flexural mode. In this way, both the flexural vibration and the sound radiation of the structure can be effectively reduced at low audio frequencies where, due to the low modal overlap [9], the overall response is indeed characterised by the resonant responses of the target low-order flexural modes.

3.1.2 Structure of the chapter

The Chapter is structured in three sections. Section 3.2 first presents the laboratory thin plate structure considered in this study, which is equipped with five piezoelectric patches connected to the proposed self-tuning RL-shunts implemented in a digital board. Then, it recalls the mathematical model used to produce the simulation analyses. Next, Section 3.3 presents simulation and experimental results that contrast the tuning effects of the reference and proposed cost functions given respectively by the minimisation of the time-averaged total flexural kinetic energy of the panel and the maximisation of the time-averaged electric power absorbed by the shunt, both with respect to the resonant response of the target mode. After that, Section 3.4 presents experimental results on the online implementation of the proposed extremum seeking gradient search tuning algorithm set to maximise the time-averaged electric power absorbed by the shunt.

3.2 Experimental Setup and Modelling

Figure 3.1 shows the test rig used for this study, which is composed by a thin flat rectangular panel made of steel. Five thin square MFC piezoelectric patches [117] are bonded on one side of the panel with the terminals connected via ad hoc interface circuits to a multi-channel dSPACE digital board, which has been used for the online implementation of the five self-tuning RL-shunts. The panel is fixed to a rigid frame and is excited by a transverse point force exerted by a shaker via a stinger equipped with a force cell. The dSPACE board works with sampling frequency of 48 kHz and has 16-bit $\pm$10V for both analogue-to-digital (ADC) and digital-to-analogue (DAC) converters. The geometry and physical properties of the panel and five equal piezoelectric patches are summarised in Table 3.1.

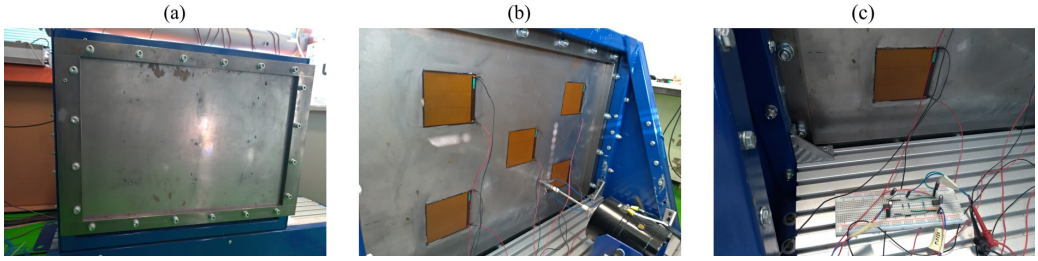

Figure 3.1: Thin panel model structure (a), which is equipped with five piezoelectric patches (b) connected to the self-tuning shunts implemented in a dSPACE digital board via *ad hoc* interface circuits (c).

Table 3.1: Dimensions and physical properties of the panel and piezoelectric patches

Parameter	Plate	Piezoelectric patches
dimensions	$l_{xp} \times l_{yp} = 668 \times 443mm$	$l_{xpe} \times l_{ype} = 85 \times 85mm$
thickness	$h_p = 1.8mm$	$h_{pe} = 0.3mm$
density	$\rho_p = 7200kg/m^3$	$\rho_{pe} = 5440kg/m^3$
Young's modulus	$E_p = 14 \times 10^{10} N/m^2$	$E_{pe} = 2.3 \times 10^{10} N/m^2$
Poisson ratio	$\nu_p = 0.3$	$\nu_{pe} = 0.35$
modal damping ratio	$\xi_p = 0.004$	
strain/charge constants		$d_{31}^0 = -212 \times 10^{-12} m/V$ $d_{32}^0 = -212 \times 10^{-12}$ $d_{36}^0 = 0$
permittivity(const. stress)		$\epsilon_{pe}^S = 18.7 \times 10^{-9} F/m$
capacitance		$C_{pe} = 466 \times 10^{-9} F$
point force position		$x_p = 0.63 l_{xp}, y_p = 0.25 l_{yp}$
patches centre position		$\frac{l_{xp}}{2}, y_{pe1} = \frac{l_{yp}}{2}$ $x_{pe2,3,4,5} = \frac{l_{xp}}{2} \pm \Delta_x,$ $y_{pe2,3,4,5} = \frac{l_{yp}}{2} \pm \Delta_y$ $\Delta_x = 185mm$, $\Delta_y = 117.5mm$

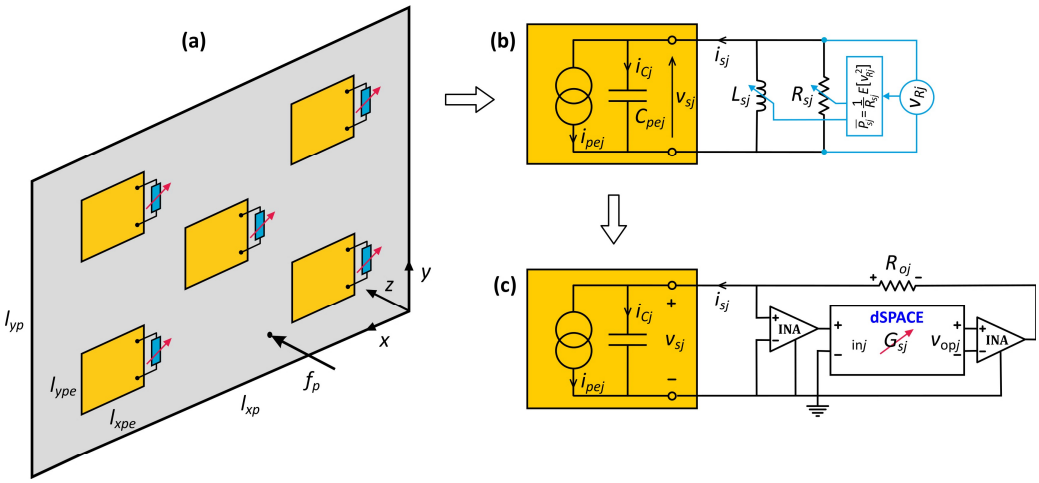

Figure 3.2: Panel with five piezoelectric patches (a) connected to RL self-tuning shunts (b) implemented in a dSPACE digital board (c).

3.2.1 Tuneable digital shunts

As depicted in Figure 3.2(a), (b), the five piezoelectric patches are connected to self-tuning shunts composed by a resistor and inductor connected in parallel. Each shunt is tuned locally to maximise the time-averaged electric power absorbed by the shunt itself, which, as shown in Figure 3.2(b), is derived from the voltage drop across the resistor of the shunt [118], [119]. More precisely, each shunt is set to maximise the electric power absorption from the resonant response of a target low-order flexural mode of the plate. To this end, the electric power is filtered with a band-pass filter centred at the resonance frequency of the target mode. The bandwidth of the filter is selected in such a way as it incorporates the resonant response of the target mode only. It is important to recall here, that the proposed control unit is meant to work at low audio frequencies, where the flexural response of the panel is characterised by a low modal density such that there is no frequency overlap between the resonant responses of neighbour flexural modes of the structure [9]. Therefore, recalling that the hosting structure is lightly damped, the filters were selected in such a way as to have about a 20 dB bandwidth with respect to the resonance peak of the target mode. The five self-tuning shunts are implemented online in a multi-channel digital board, which is connected to the five piezoelectric patches through five interface circuits [95]. More specifically, as shown in Figure 3.2(c), the terminals of each piezoelectric patch are connected to the input channels of the digital board via a high input

impedance instrumentation amplifier, which feeds to the board the shunt voltage without influencing the current flow through the terminals. Each output channel of the digital board is then connected to the terminals of the respective piezoelectric patch via a high input impedance instrumentation amplifier, which ensures the output voltage from the board is turned by the resistor R_{oj} into a given shunt current flow through the terminals of the piezoelectric patch. In this way, the desired shunt impedance can be generated on each piezoelectric patch by suitably synthesising the transfer function $G_{sj}(s)$ between the input and output channel pairs of the digital board (here s is the Laplace variable [36]). Assuming time-harmonic vibrations with the mechanical and electrical functions given in the following form $f(t) = \mathrm{Re}[f(\omega)\exp(j\omega t)]$, where $f(\omega)$ is the complex amplitude, $j = \sqrt{-1}$ and ω is the circular frequency, the following three equations can be set in the frequency domain for the interface circuit of the j-th shunt drawn in Figure 3.2(c):

$$v_{inj}(\omega) = v_{sj}(\omega), \tag{3.1}$$

$$v_{opj}(\omega) = G_{sj}(\omega) v_{inj}(\omega), \tag{3.2}$$

$$v_{sj}(\omega) - v_{opj}(\omega) = R_{oj} i_{sj}(\omega). \tag{3.3}$$

Here, $v_{sj}(\omega)$, $i_{sj}(\omega)$, $v_{inj}(\omega)$, $v_{opj}(\omega)$ are the complex amplitudes of the shunt voltage and current and of the digital board input and output voltages. Also, R_{oj} is the resistance used to generate a given current flow and $G_{sj}(\omega)$ is the frequency response function implemented in the digital board. The shunt voltage and current are linked by the electrical impedance frequency response function of the shunt $Z_{sj}(\omega)$

$$v_{sj}(\omega) = Z_{sj}(\omega) i_{sj}(\omega), \tag{3.4}$$

where, for the parallel RL-shunt considered in this study

$$\frac{1}{Z_{sj}(\omega)} = \frac{1}{R_{sj}} + \frac{1}{j\omega L_{sj}}. \tag{3.5}$$

After some mathematical steps, the following two equations are derived from the above equations:

$$Z_{sj}(\omega) = \frac{v_{sj}(\omega)}{i_{sj}(\omega)} = \frac{R_{oj}}{1 - G_{sj}(\omega)}, \tag{3.6}$$

$$G_{sj}(\omega) = \frac{v_{opj}(\omega)}{v_{inj}(\omega)} = 1 - \frac{R_{oj}}{Z_{sj}(\omega)}. \tag{3.7}$$

Here, the first equation gives the electrical impedance Z_{sj} generated by the shunt when the frequency response function G_{sj} is implemented in the digital board. Alternatively, the second equation gives the expression of the frequency response function G_{sj} that should be synthesised in the digital board to generate the desired impedance function Z_{sj}. For instance, the shunt electrical impedance given in Eq. 3.5 can be generated with the circuit shown in Figure 3.2(c) provided the digital board synthetises the following frequency response function

$$G_{sj}(\omega) = 1 - \frac{R_{oj}}{R_{sj}} - \frac{R_{oj}}{j\omega L_{sj}} = \frac{j\omega(R_{sj} - R_{oj})L_{sj} - R_{oj}R_{sj}}{j\omega R_{sj}L_{sj}}. \tag{3.8}$$

In practice, the dSPACE board was operated through a Real-Time Interface, which implemented a MATLAB–Simulink model of the desired transfer functions $G_{sj}(s)$ between the dSPACE input and output ports connected to the piezoelectric patches. To minimise high frequency noise effects and to ensure the transfer function implemented digitally is guaranteed to be proper [24], the transfer function G_{sj} was modified in such a way as it encompasses a low-pass filtering effect with the corner frequency set at 500 Hz. This value was chosen in such a way as the digital shunt can work in the 20 – 140 Hz frequency range where the flexural response of the panel is characterised by a low modal density and thus the resonant response of the target flexural mode does not overlap with those of neighbour modes [9]. Overall, the transfer functions implemented in the dSPACE board were given by the following frequency response function

$$G_{sj}(\omega) = \frac{j\omega(R_s - R_{oj})L_s\omega_{lp,s} - R_{oj}R_s\omega_{lp,s}}{(j\omega\omega_{lp,s} - \omega^2)R_sL_s}, \tag{3.9}$$

where $\omega_{lp,s}$ is the corner frequency of the low-pass filter.

3.2.2 Electro-mechanical analytical model

The flexural response of the plate with the five piezoelectric patches connected to the RL-shunts was derived from Hamilton's principle [113], [120], [121], which sets to zero the following variation integral

$$\text{V.I.} = \int_{t_1}^{t_2} [\Delta(K^* - V + W_e^*) + \Delta W_n c]dt = 0, \tag{3.10}$$

where $\Delta(\ )$ is the variation operator. The composite structure at hand is formed by an isotropic thin plate and five comparatively thinner orthotropic

piezoelectric patches; therefore, classical laminate plate theory was assumed [122] such that, the kinetic coenergy K^*, the elastic potential energy V and the electrical coenergy W_e^* for the flexural vibrations of the structure are expressed as follows [66]:

$$K^* = \frac{1}{2}\int_{V_p} \rho_p \dot{w}^2 dV_p + \sum_{j=1}^{5} \frac{1}{2}\int_{V_{pe,j}} \rho_{pe} \dot{w}^2 dV_{pe,j}, \tag{3.11}$$

$$V = \frac{1}{2}\int_{V_p} \mathbf{S}_p^T \mathbf{T}_p dV_p + \sum_{j=1}^{5} \frac{1}{2}\int_{V_{pe,j}} \mathbf{S}_{pe,j}^T \mathbf{T}_{pe,j} dV_{pe,j}, \tag{3.12}$$

$$W_e^* = \sum_{j=1}^{5} \frac{1}{2}\int_{V_{pe,j}} E_{pe,j} D_{pe,j} dV_{pe,j}. \tag{3.13}$$

In these equations, ρ_p, ρ_{pe} are the densities of the plate and piezoelectric material, $w(x,y)$, $\dot{w}(x,y)$ are the transverse displacement and velocity of the plate mid-plane (for brevity in the formulation the dependency on x, y is omitted) and V_p and $V_{pe,j}$ are the volumes of the plate and j-th piezoelectric patch. Also, recalling that the classical laminate plate theory leads to a case of both plane strain and plane stress [122] such that, considering the Kelvin-Voigt notation [123], $S_3 = S_4 = S_5 = 0$ and $T_3 = T_4 = T_5 = 0$, $\mathbf{T}_p = \begin{bmatrix} T_{p1} & T_{p2} & T_{p6} \end{bmatrix}^T$, $\mathbf{S}_p = \begin{bmatrix} S_{p1} & S_{p2} & S_{p6} \end{bmatrix}^T$ and $\mathbf{T}_{pe,j} = \begin{bmatrix} T_{pe1,j} & T_{pe2,j} & T_{pe6,j} \end{bmatrix}^T$, $\mathbf{S}_{pe,j} = \begin{bmatrix} S_{pe1,j} & S_{pe2,j} & S_{pe6,j} \end{bmatrix}^T$ are the stress and strain vectors for the plate structure and piezoelectric patch transducers, where $(\ )^T$ is the vector transpose operator. Finally, $E_{pe,j}$ and $D_{pe,j}$ are the electric field across the j-th piezoelectric patch (i.e. in z-direction) and the electric displacement at the two electrodes of the j-th piezoelectric patch. According to the classical laminate plate theory [122], the following stress-strain relations holds [113], [120]:

$$\mathbf{T}_p = \mathbf{c}_p \mathbf{S}_p, \tag{3.14}$$

$$\begin{bmatrix} D_{pe,j} \\ \mathbf{T}_{pe,j} \end{bmatrix} = \begin{bmatrix} \epsilon_{pe}^S & \mathbf{e}_{pe}^T \\ -\mathbf{e}_{pe} & \mathbf{c}_{pe}^E \end{bmatrix} \begin{bmatrix} E_{pe,j} \\ \mathbf{S}_{pe,j} \end{bmatrix}. \tag{3.15}$$

Here, the stiffness matrices for the plate and piezoelectric materials are given by:

$$\mathbf{c}_p = \begin{bmatrix} \frac{Y_p}{1-\nu_p^2} & \frac{\nu_p Y_p}{1-\nu_p^2} & 0 \\ \frac{\nu_p Y_p}{1-\nu_p^2} & \frac{Y_p}{1-\nu_p^2} & 0 \\ 0 & 0 & \frac{Y_p}{2(1+\nu_p)} \end{bmatrix}, \tag{3.16}$$

$$\mathbf{c}_{pe}^{E} = \begin{bmatrix} \frac{Y_{pe}^{E}}{1-\nu_{pe}^{E\,2}} & \frac{\nu_{pe}^{E} Y_{pe}^{E}}{1-\nu_{pe}^{E\,2}} & 0 \\ \frac{\nu_{pe}^{E} Y_{pe}^{E}}{1-\nu_{pe}^{E\,2}} & \frac{Y_{pe}^{E}}{1-\nu_{pe}^{E\,2}} & 0 \\ 0 & 0 & \frac{Y_{pe}^{E}}{2(1+\nu_{pe}^{E})} \end{bmatrix}, \tag{3.17}$$

where Y_p, ν_p and Y_{pe}^{E} and ν_{pe}^{E} are the Young's modulus and Poisson ratio of the plate and piezoelectric patches materials, the latter being taken with respect to constant electric field intensity, i.e., $E_{pe,j} = 0$. In addition, ϵ_{pe}^{S} is the permittivity of the piezoelectric material under constant strain and $e_{pe} = \begin{bmatrix} e_{31} & e_{32} & 0 \end{bmatrix}^T$ is the vector with the e_{31} and e_{32} piezoelectric stress/charge constants of the piezoelectric material, which are given by the following relations

$$\epsilon_{pe}^{S} = \epsilon_{pe}^{T}(1 - k^2), \tag{3.18}$$

$$\mathbf{e}_{pe} = \mathbf{c}_{pe}^{E}\mathbf{d}_{pe}. \tag{3.19}$$

Here ϵ_{pe}^{T} is the permittivity of the piezoelectric material under constant stress, $k^2 = \mathbf{d}_{pe}^{T}\mathbf{c}_{pe}^{E}\mathbf{d}_{pe}/\epsilon_{pe}^{T}$ is the electromechanical coupling factor of the piezoelectric material and the column vector $\mathbf{d}_{pe} = \begin{bmatrix} d_{31} & d_{32} & 0 \end{bmatrix}^T$ encompasses the d_{31} and d_{32} piezoelectric strain/charge constants reported in Table 3.1 [61], [113]. Finally, the classical laminated plate theory [122] assumes that, for a given position (x, y), the components in the strain vectors are linked to the plate mid-plane transverse displacement w through the following relations

$$\mathbf{S}_p = -z\mathbf{k}, \tag{3.20}$$

$$\mathbf{S}_{pe,j} = -z\mathbf{k}, \tag{3.21}$$

where the column vector $\mathbf{k} = \begin{bmatrix} \frac{\partial^2 w}{\partial x^2} & \frac{\partial^2 w}{\partial y^2} & 2\frac{\partial^2 w}{\partial x \partial y} \end{bmatrix}^T$ contains second derivatives of $w(x, y)$ with respect to x and y. The electric field across the j-th piezoelectric patch (i.e. in z-direction), $E_{pe,j}$, and the electric displacement at the two electrodes of the j-th piezoelectric patch, $D_{pe,j}$, are linked to the potential difference across the electrodes, $v_{pe,j}$, and the current flow through the terminals, $i_{pe,j}$, via the following two relations [61], [113]:

$$E_{pe,j} = \frac{v_{pe,j}}{h_{pe,j}}, \tag{3.22}$$

$$i_{pe,j} = \frac{d}{dt}\int_{A_{pe,j}} D_{pe,j} dA_{pe,j}, \tag{3.23}$$

where $h_{pe,j}$ is the thickness of the piezoelectric patch. Moving back to Eq. 3.10, ΔW_{nc} encompasses the virtual work done by the external force applied to the plate, the damping effect produced by the air and the electric currents flowing to the piezoelectric patches, which can be casted in the following expression [66]:

$$\Delta W_{nc} = \int_{A_p} f_p w_p dA_p - \int_{A_p} c_d w dA_p - \sum_{j=1}^{5} \int_{A_{pe,j}} \sigma_{pe,j} v_{pe,j} dA_{pe,j}. \quad (3.24)$$

Here, A_p and $A_{pe,j}$ are the areas of the plate and j-th piezoelectric patch. Also, in the first term, f_p and w_p are the transverse force and displacement at the primary excitation position (x_p, y_p). In the second term, c_d is the damping coefficient per unit surface for the damping force exerted by the air $f_d(x, y) = -c_d \dot{w}(x, y)$. Finally, in the third term, $\sigma_{pe,j}, v_{pe,j}$ are the surface charge density at, and the electric potential difference across, the electrodes of the j-th piezoelectric patch.

3.2.3 Electro-mechanical coupled equations

As shown in Figure 3.1 and discussed above, the thin plate is equipped with five piezoelectric patches, which, however, are comparatively much thinner and cover a rather large portion of the plate such that they generate quite uniform inertia and bending effects over the surface of the plate. In this case, the flexural response can be approximated with reference to the natural frequencies and natural modes of a uniform composite plate with equivalent smeared stiffness and smeared inertia effects. In this way, assuming synchronous motion, such that the response is separable into space and time functions, and assuming the plate is exposed to a light viscous damping effect produced by the air, which can be conveniently modelled as a proportional damping [124], the expansion theorem for self-adjoint systems can be employed to express the transverse displacement as a linear combination of the natural modes $\phi_{nr}(x, y)$ and the generalised (or modal) coordinates $q_r(t)$:

$$w(x, y, t) = \sum_{r=1}^{R} \phi_{nr}(x, y) q_r(t) = \phi(x, y) q(t). \quad (3.25)$$

Here $\phi(x, y) = \begin{bmatrix} \phi_{n1}(x, y) & \dots & \phi_{nR}(x, y) \end{bmatrix}$ is a row vector with the amplitudes of the natural modes at position (x, y) and $q(t) = \begin{bmatrix} q_1(t) & \dots & q_R(t) \end{bmatrix}^T$ is a column vector with the generalised coordinates. A modal analysis of the flexural vibration of the plate with the piezoelectric patches in short circuit

[125] showed that, despite the plate was fixed on a rigid frame, the flexural natural modes can be suitably described with the following expression for simply supported plates [124],

$$\phi_{nr}(x,y) = 2\sin\left(\frac{r_1\pi x}{l_{xp}}\right)\sin\left(\frac{r_2\pi y}{l_{yp}}\right), \tag{3.26}$$

where r_1, r_2 represent the modal indices of the r-th mode. Therefore, the flexural natural frequencies were derived from the following expression [124]

$$\omega_{nr} = \sqrt{\frac{E_s h_p^2}{12\rho_s(1-\nu_s^2)}}\left[\left(\frac{r_1\pi}{l_{xp}}\right)^2 + \left(\frac{r_2\pi}{l_{yp}}\right)^2\right], \tag{3.27}$$

with reference to the thickness of the plate h_p and the smeared density, ρ_s, smeared Young's modulus of elasticity, E_s, and smeared Poisson's ratio, ν_s, of the composite plate summarized in Table 3.1. These values were based on those for steel, corrected in such a way as to comply with the natural frequencies identified from the measured flexural frequency response functions of the panel with the piezoelectric patches in short circuit [125]. The modal expansion for the plate transverse displacement introduced in Eq. 3.25 can be conveniently employed to derive the energies and virtual work done by non-conservative forces formulated in the previous sections, such that, after a few mathematical steps (e.g. see Ref. [66]), the Hamilton's variation integral principle stated in Eq. 3.10 results into the set of R coupled equations of motion and into a set of 5 coupled equations for the electro-mechanical response of the five piezoelectric patches reported below in compact matrix form:

$$\mathbf{M}\ddot{\mathbf{q}}(t) + \mathbf{C}\dot{\mathbf{q}}(t) + \mathbf{K}\mathbf{q}(t) + \mathbf{\Theta}_{pe}\mathbf{v}_s(t) = \mathbf{\Phi}_p f_p(t), \tag{3.28}$$

$$-\mathbf{\Theta}_{pe}^T\mathbf{q}(t) + \mathbf{C}_{pe}\mathbf{v}_s(t) = \mathbf{q}_s(t). \tag{3.29}$$

Here, $v_s(t)$ and $q_s(t)$ are the vectors with the potential difference and the charges at the terminals of the piezoelectric patches. Also,

$$\mathbf{M} = \begin{bmatrix} m_p & & \\ & \ddots & \\ & & m_p \end{bmatrix}, \tag{3.30}$$

$$\mathbf{C} = \begin{bmatrix} 2\xi_p\omega_{n1}m_p & & \\ & \ddots & \\ & & 2\xi_p\omega_{nR}m_p \end{bmatrix}, \tag{3.31}$$

$$\mathbf{K} = \begin{bmatrix} \omega_{n1}^2 m_p & & \\ & \ddots & \\ & & \omega_{nR}^2 m_p \end{bmatrix}. \tag{3.32}$$

are the $R \times R$ modal mass, damping and stiffness diagonal matrices, where, m_p is the mass of the plate and piezoelectric patches whereas ξ_p and ω_{nr} are the damping ratio and natural frequencies of the plate and piezoelectric patches flexural modes. The damping effect produced by the air on the plate has been assumed comparable for the first few flexural natural modes. Moreover,

$$\Theta_{pe} = \begin{bmatrix} \theta_{11} & \theta_{12} & \dots & \theta_{1N} \\ \theta_{21} & \theta_{22} & \dots & \theta_{2N} \\ \dots & \dots & \dots & \dots \\ \theta_{R1} & \theta_{R2} & \dots & \theta_{RN} \end{bmatrix} \tag{3.33}$$

is the $R \times N$ matrix with the transduction factors, which have been derived with the following equation [66]

$$\theta_{rj} = 2 z_{pe} \int_{A_{pe,j}} \nabla^2 \phi_{nr}(x, y) \mathbf{e}_{pe} dA_{pe,j}, \tag{3.34}$$

where $\nabla^2 \phi_{nr} = \begin{bmatrix} \frac{\partial^2 \phi_{nr}}{\partial x^2} & \frac{\partial^2 \phi_{nr}}{\partial y^2} & 2\frac{\partial^2 \phi_{nr}}{\partial x \partial y} \end{bmatrix}$ and the column vector e_{pe} with the piezoelectric stress/charge constants is given in Eq. 3.21. Also,

$$\Phi_p = \begin{bmatrix} \boldsymbol{\phi}_{n1}(x_p, y_p) \\ \vdots \\ \phi_{nR}(x_p, y_p) \end{bmatrix}, \tag{3.35}$$

encompasses the amplitudes of the flexural natural modes at the primary force position. Lastly,

$$\mathbf{C}_{pe} = \begin{bmatrix} C_{pe}^S & & \\ & \ddots & \\ & & C_{pe}^S \end{bmatrix}, \tag{3.36}$$

is the diagonal matrix with the capacitances C_{pe}^S under constant strain of the piezoelectric patches. The parameters used to calculate these matrices are summarised in Table 3.1 and were taken from datasheets of the materials, from inspection of the test rig and from a modal analysis carried out on the flexural response of the plate with the five piezoelectric patches in short circuit using a laser vibrometer [125]. The modal analysis showed that, in the vicinity of the excitation point, the shapes of the (3,1) and (1,2) modes

do not overlap exactly the functions given by Eq. 3.26. This is due to the mass effect produced by the load cell used to measure the force exerted by the shaker. Therefore, both the amplitudes at the excitation point $\phi_{nr}(x_p, y_p)$ and the transduction factors θ_{ri} for these two modes were adjusted according to the measured shapes.

3.2.4 Cost functions

As anticipated above, the shunted piezoelectric units have been designed to control the time-averaged resonant response of a target flexural mode when the hosting plate structure is exposed to a stationary stochastic excitation. Therefore, as done in Chapter 2, two cost functions were considered in this study. First, the so-called "reference cost function" given by the time-averaged and spatially-averaged flexural vibration of the structure, which has been used to monitor the response of the panel when the piezoelectric patches are not connected to the shunts, and thus are in open circuit, or implement the self-tuning RL shunts. Second, the so-called "tuning cost function" given by the time-averaged vibration energy absorbed by each shunted piezoelectric patch, which, in fact, has been used to tune online the resistive and inductive components of the shunts. More specifically, the reference cost function has been taken as the time-averaged total flexural kinetic energy of the panel, that is

$$\bar{K}(R_{sj}, L_{sj}) = E[K(R_{sj}, L_{sj}, t)], \tag{3.37}$$

where $E[\,]$ is the expectation operator and $K(R_{sj}, L_{sj}, t)$ is the time-dependent total flexural kinetic energy of the panel, which according to Eq. 3.11 can be written as follows:

$$K(t) = \frac{1}{2}\int_{A_p} \rho_p h_p \dot{w}^2 dA_p + \sum_{j=1}^{5} \frac{1}{2}\int_{A_{pe,j}} \rho_{pe} h_{pe} \dot{w}^2 dA_{pe,j}. \tag{3.38}$$

As done in Ref. [56] for shunted electromagnetic proof-mass transducers, the tuning cost function has been estimated with the time-averaged electric power absorbed by the shunt, which, for the j-th shunt, is given by:

$$\bar{P}(R_{sj}, L_{sj}, t) = E[P(R_{sj}, L_{sj}, t)], \tag{3.39}$$

where $P(R_{sj}, L_{sj}, t)$ is the time-dependent electric power absorbed by the shunt, that is

$$P(R_{sj}, L_{sj}, t) = v_{sj} i_{sj}. \tag{3.40}$$

Since the electric power absorbed by the shunt coincides with the power dissipated by the shunt itself, as shown in Figure 3.2(b), in practice the

tuning power function will be derived from the voltage drop across the shunt resistor:

$$P(R_{sj}, L_{sj}, t) = v_{Rj} i_{Rj} = \frac{1}{R_{sj}} v_{Rj}^2. \tag{3.41}$$

In this study, both cost functions will be derived using a frequency-domain formulation based respectively on simulated and measured Power Spectral Density (PSD) functions. Indeed, according to Refs. [114], [126], for stationary ergodic processes, the reference and tuning cost functions can also be derived from the following frequency integrals

$$\bar{K}(R_{sj}, L_{sj}) = \frac{1}{2\pi} \int_{-\infty}^{+\infty} S_K(R_{sj}, L_{sj}, \omega) d\omega, \tag{3.42}$$

$$\bar{P}(R_{sj}, L_{sj}) = \frac{1}{2\pi} \int_{-\infty}^{+\infty} S_P(R_{sj}, L_{sj}, \omega) d\omega, \tag{3.43}$$

where $S_K(R_{sj}, L_{sj}, \omega)$ is the PSD of the plate total flexural kinetic energy and $S_P(R_{sj}, L_{sj}, \omega)$ is the PSD of the electric power absorbed by the j-th shunt. Based on Eq. 3.38, the PSD of the flexural kinetic energy is given by:

$$\begin{aligned} S_K(R_{sj}, L_{sj}, \omega) = \frac{1}{2} \int_{A_p} \rho_p h_p \lim_{T \to \infty} E\Big[\frac{1}{T} \dot{w}^*(x, y, \omega) \dot{w}(x, y, \omega)\Big] dA_p + \\ \sum_{j=1}^{5} \frac{1}{2} \int_{A_{pe,i}} \rho_{pe} h_{pe} \lim_{T \to \infty} E\Big[\frac{1}{T} \dot{w}^*(x, y, \omega) \dot{w}(x, y, \omega)\Big] dA_{pe,i}, \end{aligned} \tag{3.44}$$

where $\dot{w}(x, y, \omega)$ is the complex amplitude of the time-harmonic transverse velocity of the plate. Also, according to Eq. 3.41, the PSD of the electric power absorbed by the j-th shunt is given by:

$$S_P(R_{sj}, L_{sj}, \omega) = -\frac{1}{R_{sj}} \lim_{T \to \infty} E\Big[\frac{1}{T} v_{sj}^*(\omega) v_{sj}(\omega)\Big], \tag{3.45}$$

where $v_{sj}(\omega)$ is the complex amplitude of the time-harmonic voltage of the shunt. Since the objective of the shunted piezoelectric patch units is to control the resonant response of a target r-th mode, the two cost functions were derived considering the frequency integrals in a band $\Delta\omega_r$ centred on the natural frequency of the target mode such that

$$\bar{K}_r(R_{sj}, L_{sj}) = \frac{1}{\pi} \int_{\omega_{nr} - \frac{\Delta\omega_r}{2}}^{\omega_{nr} + \frac{\Delta\omega_r}{2}} S_K(R_{sj}, L_{sj}, \omega) d\omega, \tag{3.46}$$

$$\bar{P}_r(R_{sj}, L_{sj}) = \frac{1}{\pi} \int_{\omega_{nr} - \frac{\Delta\omega_r}{2}}^{\omega_{nr} + \frac{\Delta\omega_r}{2}} S_P(R_{sj}, L_{sj}, \omega) d\omega. \tag{3.47}$$

Given that the panel structure considered in this study is lightly damped, the frequency band was selected in such a way as to have about a 20 dB bandwidth with respect to the resonance peak of the target mode kinetic energy. The forthcoming section presents the frequency domain formulation developed to derive the PSD functions in Eqs. 3.44 and 3.45 and thus to derive the time-average cost functions given by Eqs. 3.46 and 3.47.

3.2.5 Frequency domain formulation

Assuming time-harmonic functions, the two sets of ordinary differential equations in Eqs. 3.25 and 3.26 become

$$[j\omega\mathbf{M} + \mathbf{C} + \frac{1}{j\omega}\mathbf{K}]\dot{\mathbf{q}}(\omega) + \mathbf{\Theta}_{pe}\mathbf{v}_s(\omega) = \mathbf{\Phi}_p f_p(\omega), \tag{3.48}$$

$$-\mathbf{\Theta}_{pe}^T\dot{\mathbf{q}}(\omega) + j\omega\mathbf{C}_{pe}\mathbf{v}_s(\omega) = \mathbf{i}_s(\omega), \tag{3.49}$$

where, recalling that $\mathbf{i}_s = \frac{d\mathbf{q}_s}{dt}$, the vectors $\dot{\mathbf{q}}(\omega)$, $\mathbf{v}_s(\omega)$, $\mathbf{i}_s(\omega)$ contain the complex amplitudes of the generalized velocities, shunt voltages and shunt currents respectively. Also, $f_p(\omega)$ is the vector with the complex amplitude of the force excitation acting on the panel. For time-harmonic vibrations, the following matrix expression can be set for the five shunts

$$\mathbf{v}_s(\omega) = -\mathbf{Z}_s(\omega)\mathbf{i}_s(\omega), \tag{3.50}$$

where $\mathbf{Z}_s(\omega)$ is a diagonal matrix with the shunt impedances, which are given by

$$Z_{sj} = \frac{j\omega L_{sj}R_{sj}}{R_{sj} + j\omega L_{sj}}. \tag{3.51}$$

Equations 3.48, 3.49, 3.50 can be combined to give

$$\dot{\mathbf{q}}(\omega) = \mathbf{Y}_s(\omega)\mathbf{\Phi}_p f_p(\omega), \tag{3.52}$$

where,

$$\mathbf{Y}_s(\omega) = j\omega[-\omega^2\mathbf{M} + j\omega(\mathbf{C} + \mathbf{\Theta}_{pe}\mathbf{Z}_{pe}(\omega)\mathbf{\Theta}_{pe}^T) + \mathbf{K}]^{-1}, \tag{3.53}$$

and $\mathbf{Z}_{pe}(\omega)$ is a diagonal matrix with the following impedance terms

$$\mathbf{Z}_{pej}(\omega) = \frac{Z_{sj}(\omega)}{1 + j\omega Z_{sj}(\omega)C_{pe}}. \tag{3.54}$$

Also, combining Eqs. 3.49, 3.50, 3.52, the shunt voltages are given by

$$\mathbf{v}_s(\omega) = \mathbf{Z}_{pe}(\omega)\mathbf{\Theta}_{pe}^T\mathbf{Y}(\omega)\mathbf{\Phi}_p f_p(\omega). \tag{3.55}$$

Now, recalling the modal expansion given in Eq. 3.25, the complex amplitude of the plate transverse velocity can be expressed as follows

$$w(x, y, \omega) = \boldsymbol{\phi}(x, y)\mathbf{q}(\omega). \tag{3.56}$$

Since the natural modes are mass-normalised [124], substitution of Eq. 3.56 into Eq. 3.44 leads to the following matrix expression for the PSD of the flexural kinetic energy

$$S_K(\omega) = \frac{1}{2}\mathrm{Tr}[\mathbf{M}\mathbf{Y}(\omega)\boldsymbol{\Phi}_p S_{ff}(\omega)\boldsymbol{\Phi}_p^T\mathbf{Y}^H(\omega)], \tag{3.57}$$

where Tr[ ] is the trace matrix operator and $S_{ff}(\omega)$ is the PSD of the primary force excitation. Also, recalling Eq. 3.45, since for the parallel RL-shunts the voltage drop across the shunt resistor corresponds to the voltage across the shunt terminals, the PSD of the electric power absorbed by the j-th shunt can be derived conveniently using Eqs. 3.55 and 3.45, such that

$$S_P(\omega) = -[\mathbf{R}_s^{-1}\mathbf{Z}_{pe}(\omega)\boldsymbol{\Theta}_{pe}^T Y(\omega)\boldsymbol{\Phi}_p S_{ff}(\omega)\boldsymbol{\Phi}_p^T Y^H(\omega)\boldsymbol{\Theta}_{pe}\mathbf{Z}_{pe}^H(\omega)]_{jj}, \tag{3.58}$$

where $\mathbf{R}_s$ is a diagonal matrix with the shunt resistances R_{sj} and $[\,]_{jj}$ indicates the j-th diagonal term of the square matrix.

3.3 Tuning analysis

To start with, this section presents a tuning analysis assuming all piezoelectric patches are connected to individual RL-shunts set to control the resonant response respectively of the first, second and fourth flexural modes of the panel. In particular, the RL-maps of the reference and tuning cost functions are depicted and analysed to investigate if, for the resonant response of the target mode, the maximization of the time-averaged electric power absorbed by the shunt $\bar{P}_r(R_{sj}, L_{sj})$ leads to the same tuning parameters than the minimization of the time-averaged total flexural kinetic energy $\bar{K}_r(R_{sj}, L_{sj})$. Then, the PSD of the two cost functions are analysed in the frequency domain assuming the piezoelectric patches are either in open circuit or connected to the RL-shunt tuned to maximize the time-averaged electric power absorbed by the shunts from the resonant response of the target mode. The shunted piezoelectric patch vibration absorber is meant to control low-order modes, therefore it has been opted to investigate the tuning to control the resonant responses of the first, second and fourth flexural modes of the panel. The third mode is characterised by a smaller resonant response in first instance and thus it has not been investigated.

3.3.1 Global versus local tuning

Figures 3.3 and 3.4 show the simulated and measured maps of the reference cost function, $\bar{K}_r(R_{sj}, L_{sj})$ (left hand side plots), and tuning cost function, $\bar{P}_r(R_{sj}, L_{sj})$ (right hand side plots), when the shunts connected to the patches are set to control the resonant response of the first, second and fourth flexural modes (i.e. $r = 1, 2, 4$). Considering first the simulated maps shown in Figure 3.3, it is noted that, for all three modes, the map of $\bar{K}_r$ is characterised by a non-convex inverse bell-shape with a single minimum whereas the map of $\bar{P}_r$ has a mirror non-convex bell-shape with a single maximum. As highlighted by the cross and circular markers, the points of minimum of $\bar{K}_r$ and maximum of $\bar{P}_r$ closely overlap in the maps. The same pair of maps were derived for the resonant responses of the other modes that resonate in the 20 – 140 Hz frequency band considered in this study, and all showed these properties. The measured maps depicted in Figure 3.4 show very similar results. Compared to the simulated maps, they appear less smooth. This is due to the lengthy measurement procedure necessary to produce the maps. In fact, to generate each point of the maps, the spectrum of the total flexural kinetic energy of the panel had to be measured with a scanner laser vibrometer. Although a relatively coarse grid of 4×4 points was used to measure the velocities of the panel necessary to estimate the total flexural kinetic energy, the measurement time was rather high. To contain the total time necessary to produce the two maps in 15 hours, the number of points in the maps, that is the number of resistance and inductance values implemented in the shunt, was also kept low. Indeed, the measured maps considered a 21×20 grid of resistance and inductance values.

The overall outcome was therefore non-perfectly smooth surfaces. This problem was not merely the result of the coarse vibration measurements over the surface of the plate and coarse resistance-inductance measurements, but was also due to the variability over the fifteen hours measurement campaign of the flexural response of the plate and electrical response of the equipment used to synthesize the shunt. This variability effect was due primarily to changes of the ambient and equipment temperature. Nevertheless, despite these challenges, the measured maps show quite a remarkable agreement with the simulated ones. The minimum of $\bar{K}_r$ and the maximum of $\bar{P}_r$ are rather close to each other and replicate quite accurately the simulated one. Besides, the two maps are quite flat in the vicinity of minimum/maximum points and thus the non-perfect alignment of the minimum of $\bar{K}_r$ and the maximum of $\bar{P}_r$ can be considered negligible. In conclusion, the simulation and measurement results show that, considering the resonant response of

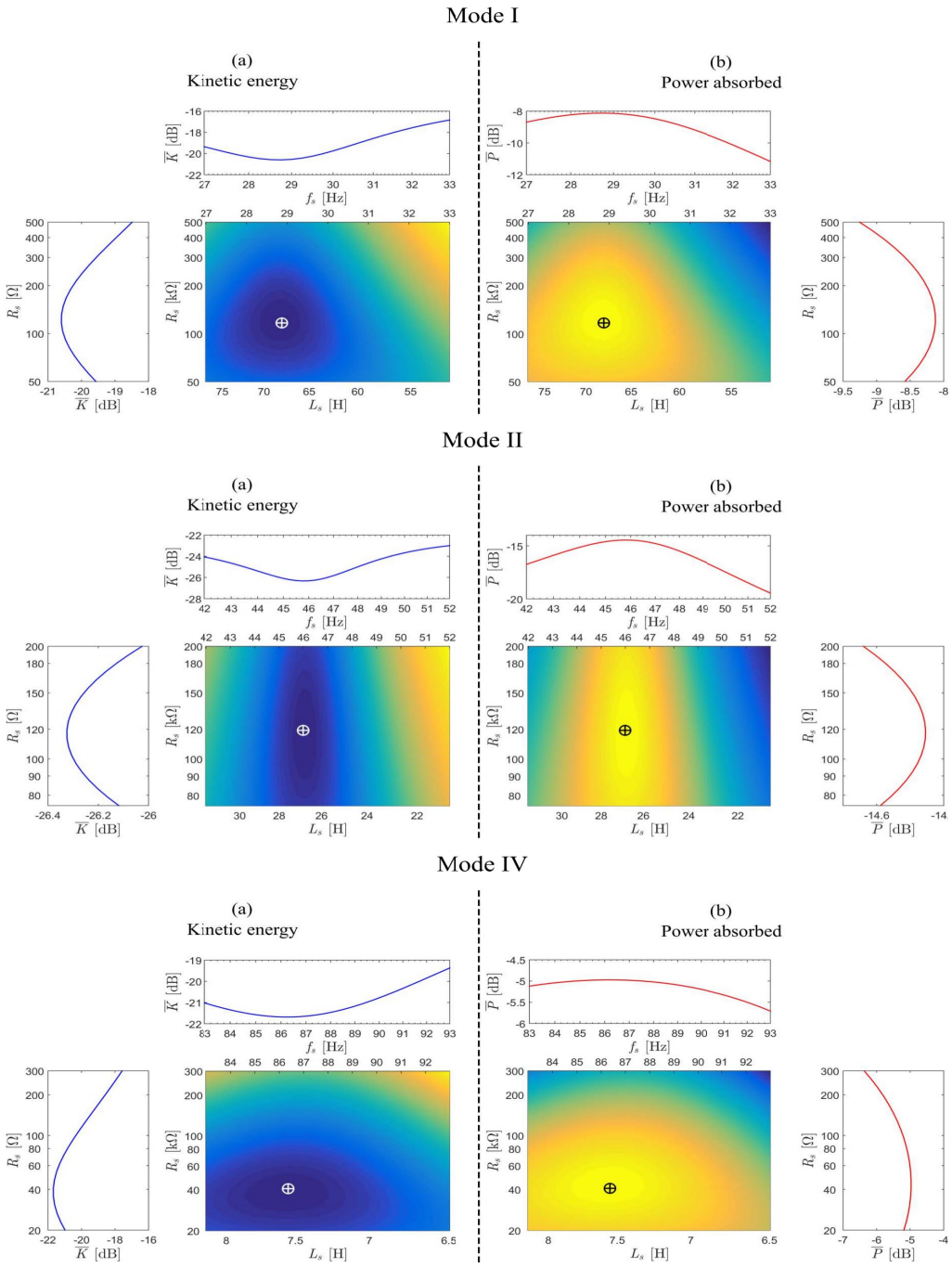

Figure 3.3: Simulated maps of $\bar{K}(R_s, L_s)$ (a) and $\bar{P}(R_s, L_s)$ (b) when the shunts are set to control the resonant response of mode 1 (top), mode 2 (centre), mode 4 (bottom), with slice cuts at $L_s = L_{opt}$ (lateral plots) and $R_s = R_{opt}$ (top plots). Cross marker $\min(\bar{K})$. Circular marker $\max(\bar{P}_j)$.

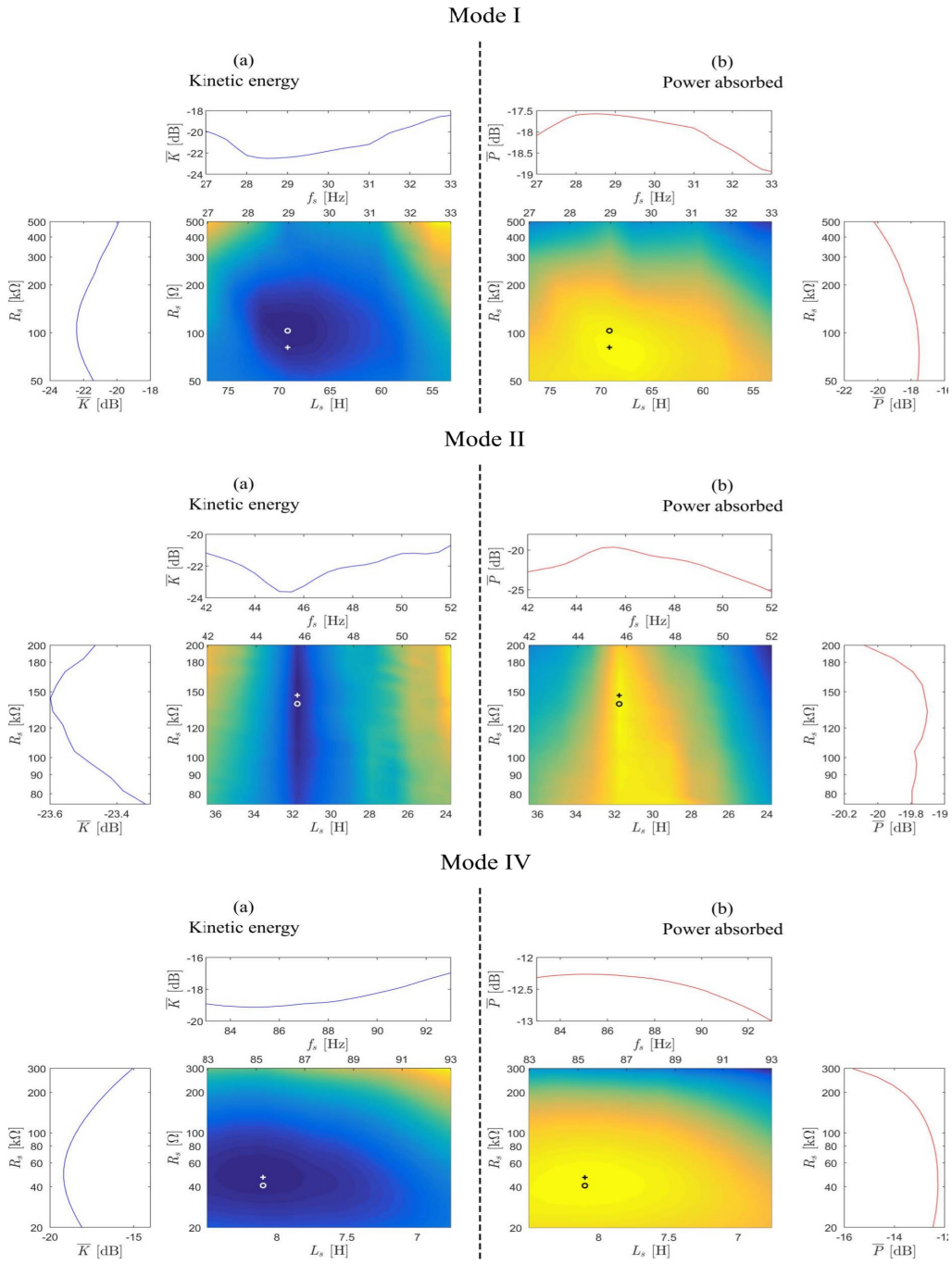

Figure 3.4: Measured maps of $\bar{K}(R_s, L_s)$ (a) and $\bar{P}(R_s, L_s)$ (b) when the shunts are set to control the resonant response of mode 1 (top), mode 2 (centre), mode 4 (bottom), with slice cuts at $L_s = L_{opt}$ (lateral plots) and $R_s = R_{opt}$ (top plots). Cross marker min($\bar{K}$). Circular marker max($barP_j$).

well-separated low-order flexural modes of the structure [9], the minimum of the plate time-averaged total flexural kinetic energy and the maximum of the time-averaged electric power absorbed by the shunt are characterised by close values of the optimal shunt resistance and close values of the optimal shunt inductance. Hence, as found with simulations in Refs. [118], [119], to minimise the time-averaged total flexural kinetic energy, that is the time-averaged and spatially-averaged flexural response of the structure, the resistance and inductance of the shunt should be tuned to maximise the time-average electric power absorbed by the shunt itself. This is quite a remarkable result, which suggests that the RL-shunt can be tuned locally without the need of structural sensors that measure the flexural response of the target mode of the structure, as for example shaped piezoelectric transducers [127]–[130]. On the contrary, it is sufficient to measure the electric power absorbed by the shunt, which, as depicted in Figure 3.2b and given in Eq. (41), can be suitably estimated from the voltage drop across the shunt resistor.

A thorough analysis of the kinetic energy and power cost functions shows that the two maps are characterised by constant resistance $R_{sj} = R_{sj,opt}$ and constant inductance $L_{sj} = L_{sj,opt}$ principal directions [118], [119]. Hence, the tuning can be carried out in two phases where, starting from arbitrary initial values of the shunt resistance and inductance $(R_{sj,ini}, L_{sj,ini})$, the optimal inductance $L_{sj,opt}$ is first searched along the path $R_{sj} = R_{sj,ini}$ and then the optimal resistance is searched along the path $L_{sj} = L_{sj,opt}$. A detailed analysis of the maps highlights that the two paths lead to a point quite close, but not equal, to the maximum of $\bar{P}_r$, that is the minimum of $\bar{K}_r$. Therefore, the two-paths tuning should be repeated continuously online. This would be necessary in any case to trace the optimal tuning of real applications, where the dynamic properties (i.e., natural frequencies and damping ratios) of the structures as well as the electro-mechanical properties of the piezoelectric transducers and shunts may vary significantly during operation. The lateral and top graphs beside the two maps show that the constant resistance $R_{sj} = R_{sj,opt}$ and constant inductance $L_{sj} = L_{sj,opt}$ paths on the kinetic energy cost function are characterised by inverse bell shapes whereas the same paths on the power cost function are characterised by bell shapes. As will be discussed in the forthcoming section, the tuning of the shunt components will therefore involve a search of the maximum along non-convex bell-shaped paths, which, can be suitably implemented with an extremum seeking gradient search algorithm [103], [107], [115], [116].

3.3.2 Spectral analysis

To appreciate the control effects produced by the proposed self-tuning control units, the PSD of the two cost functions are analysed in the frequency domain in Figures 3.5 (simulations) and 3.6 (measurements) assuming the five piezoelectric patches are either in open circuit (blue lines) or connected to the RL-shunts tuned to maximise the time-averaged electric power absorbed from the resonant response of the first, second and fourth flexural modes

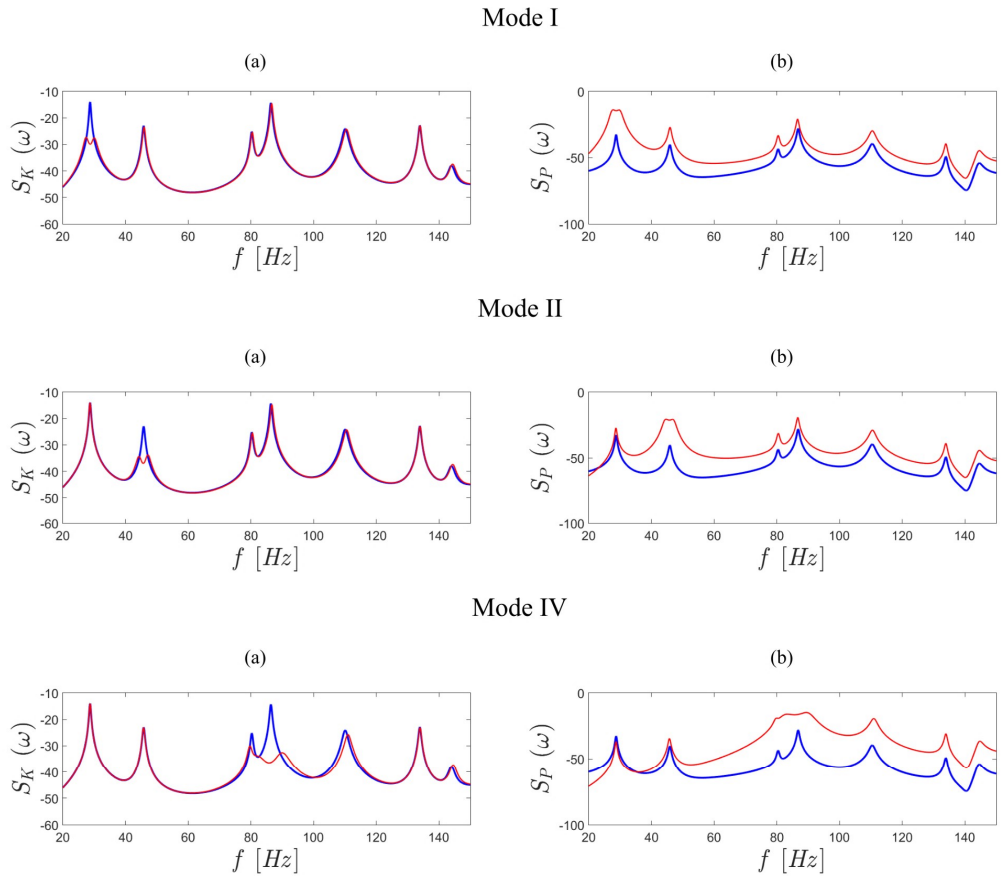

Figure 3.5: Simulated spectra of (a) $S_K(\omega)$ and (b) $S_P(\omega)$ when the piezoelectric patches are either in open circuit (blue lines) or connected to the shunts with the resistance and inductance components tuned to maximise the time-averaged power absorbed by each shunt from the resonant response of the first (top plots), second (centre plots) and fourth (bottom plots) resonant modes (red lines).

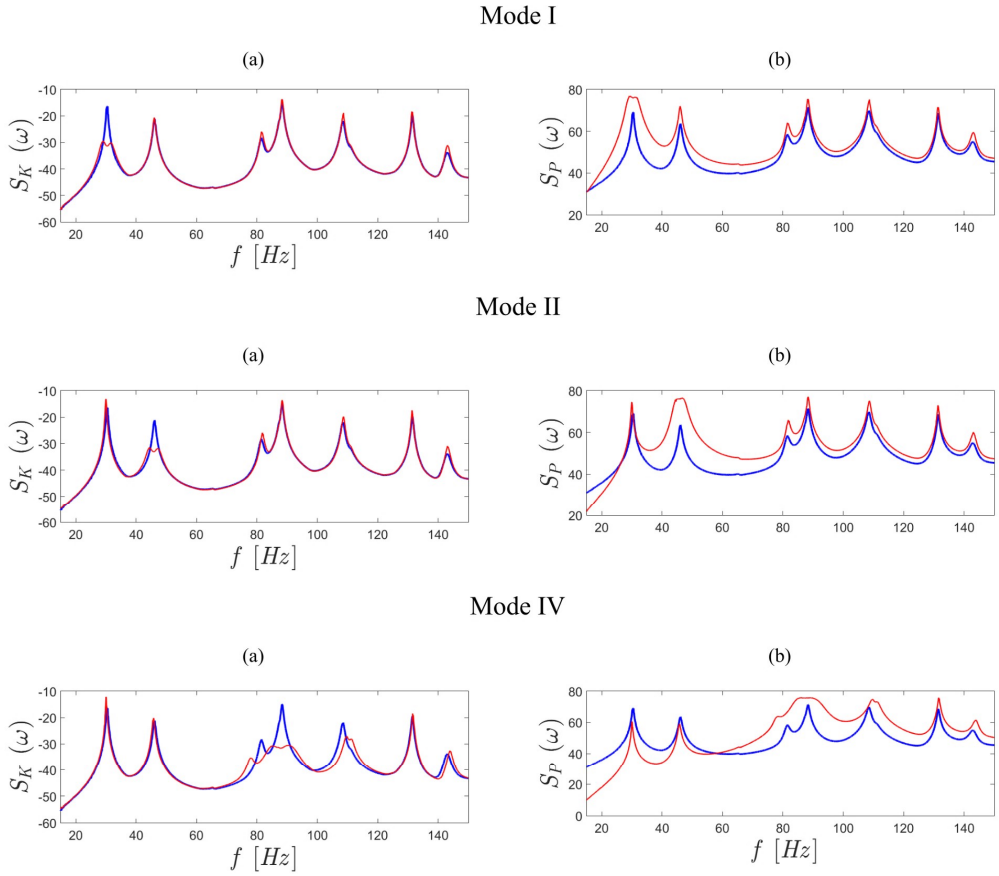

Figure 3.6: Measured spectra of (a) $S_K(\omega)$ and (b) $S_P(\omega)$ when the piezoelectric patches are either in open circuit (blue lines) or connected to the shunts with the resistance and inductance components tuned to maximise the time-averaged power absorbed by each shunt from the resonant response of the first (top plots), second (centre plots) and fourth (bottom plots) resonant modes (red lines).

of the plate (red-lines). In practice, and thus in the simulations too, the open circuit was produced with a very high shunt resistor. In this way, it has been possible to provide a benchmark spectrum for the electric power absorbed by the shunts too. The simulated spectra of the total flexural kinetic energy PSD and absorbed electric power PSD in Figure 3.5 match quite accurately the equivalent measured spectra in Figure 3.6. Considering the configuration with the five patches in open circuit, such that the patches generate an electro-mechanical stiffening effect only [66], the spectrum of the

total flexural kinetic energy PSD is characterised by 7, well separated, sharp resonance peaks. As anticipated above, even when the patches are in the open circuit configuration produced by the very high shunt resistors, some electric power is absorbed by the shunts themselves. As a result, the spectrum of the electric power absorbed by the shunts PSD is characterised by the same 7 resonance peaks despite their lower amplitude level. When the 5 patches are connected to the shunts tuned to maximise the time-averaged electric power absorbed from respectively the resonant response of the first, second, fourth flexural modes of the structure, the first, second, fourth resonance peaks of the total flexural kinetic energy PSD are levelled down in turn by about 18dB, 8dB, 15dB respectively, whereas the other peaks remain unchanged. In parallel, the amplitudes and width of the first, second, fourth resonance peaks of the absorbed electric power PSD are considerably raised in the three tuning cases, whereas the amplitude of the other peaks is significantly lowered. For instance, when the shunts are tuned to control the resonant response of the first flexural mode, the first resonance peak is 10 dB higher and 2 times wider suggesting that the optimally tuned shunt focuses the energy absorption onto the resonant response of the first target flexural mode. A similar result is produced when the 5 shunts are tuned to control the resonant response of the second flexural mode, with an increment of the amplitude of the second resonance peak in the absorbed electric power PSD of about 12dB and a doubling of its width. Instead, when the 5 patches are connected to the shunts tuned to maximise the electric power absorbed from the resonant response of the fourth flexural mode, the fourth peak of the absorbed electric power PSD is raised by about 8dB and significantly widened. Indeed, the width of the peak is about 10 Hz. Moreover, the amplitudes of the other resonance peaks are kept unchanged or slightly enhanced. Thus, when the shunts are tuned to control the resonant response of the fourth resonant mode, the energy absorption is enhanced over a rather wide frequency band that encompasses a few resonances of the structure. In general, the results presented in Figures 3.5 and 3.6 indicate that the proposed tuning approach based on the maximisation of the time-averaged electric power absorbed by the shunts leads to substantial reductions of the resonant response of the target flexural modes of the panel.

3.4 Online implementation of the self-tuning shunts

The online implementation of the self-tuning shunts is now discussed with reference to experimental results obtained with the setup depicted in Figure 3.1. As anticipated in Section 3.2, the five patches were connected to the dSPACE multi-channel digital board via the interface circuits shown in Figure 3.1(c) and described in Figure 3.2(c). The RL-shunts were synthesised in the board according to Eqs. 3.6 and 3.7. Also, the two-paths tuning approach for the maximisation of the absorbed time averaged electric power described in the previous section was implemented online in each shunt. The experiments were carried out with a stationary stochastic primary force excitation. The shunts were tuned to control in turn the resonant response of the first, second and fourth flexural modes of the plate with the power function filtered between $\omega_{nr} - \frac{\Delta\omega_r}{2}$ and $\omega_{nr} + \frac{\Delta\omega_r}{2}$, where the assumed centre frequencies and bandwidths are reported in Table 3.2.

Table 3.2: Experimental data for the online tuning procedure

Parameter	Value
1st mode resonant frequency	$\omega_{n1} = 29.8Hz$
2nd mode resonant frequency	$\omega_{n2} = 45.9Hz$
4th mode resonant frequency	$\omega_{n4} = 88.4Hz$
Band-pass frequency width	$2\Delta\omega_r = 20Hz$
Initial guess, 1st mode tuning	$R_{s,ini} = 400k\Omega, L_{s,ini} = 72H$
Initial guess, 2nd mode tuning	$R_{s,ini} = 100k\Omega, L_{s,ini} = 25H$
Initial guess, 4th mode tuning	$R_{s,ini} = 70k\Omega, L_{s,ini} = 6H$
Power threshold value	$\epsilon_P = 0.05$
Ripple frequency	$\omega_d = 0.7Hz$
High-pass filter frequency	$\omega_{hp} = 0.03Hz$
Low-pass filter frequency	$\omega_{lp} = 0.02Hz$

In order to increase the convergence speed of the shunt parameters, the tuning was implemented in parallel configuration, i.e. all the patches were tuned simultaneously. More specifically, for each unit the two-paths tuning strategy proposed in Ref. [118], [119] and discussed in the previous section was implemented starting from the initial values of the shunt components $R_{sj,ini}, L_{sj,ini}$ reported in Table 3.2. The optimal inductance $L_{sj,opt}$ was first searched along the path $R_{sj} = R_{sj,ini}$ starting from $R_{sj,ini}, L_{sj,ini}$. Then, the optimal resistance $R_{sj,opt}$ was sought along the path $L_{sj} = L_{sj,opt}$ starting

from $R_{sj,ini}, L_{sj,opt}$. The searches along the two paths were implemented using the extremum seeking algorithm whose theoretical basis was introduced in Section 2.4 and is recalled in the forthcoming Subsection 3.4.1 to discuss its practical implementation using the setup described in Section 3.2.1. This is a model-free gradient driven search algorithm, which asymptotically leads to the maximum of the non-convex bell-shaped paths with $R_{sj} = \text{const}$ and $L_{sj} = \text{const}$. Since the tuning process is asymptotic, the search along each path was stopped as the increment of the absorbed power fell below the threshold ϵ_P reported in Table 3.2. The effects produced by the self-tuning shunts connected to the five piezoelectric patches are analysed in the following Subsection 4.2. To start with, the evolution of the shunt resistance and inductance from the initial values $(R_{s5,ini}, L_{s5,ini})$ to the final optimal values $(R_{s5,opt}, L_{s5,opt})$ is discussed. Then, the flexural response of the panel and the energy absorption by the shunts is analysed by contrasting the cases where the piezoelectric patches are left in open circuit and then connected to the optimal shunts.

3.4.1 Extremum seeking tuning algorithm

The sketch in Figure 3.7 exemplifies the two-paths tuning search implemented in each shunt with the extremum seeking algorithm [107], [115], [116]. As suggested in chapter 2 The tuning of the shunt inductance (L-tuning) and resistance (R-tuning) are implemented sequentially with the same procedure. Therefore, for simplicity, the algorithm is described with reference to the L-tuning only. As discussed above, both the shunt and the extremum seeking algorithm are implemented digitally in the multi-channel dSPACE board. Therefore, the whole scheme in Figure 3.7 assumes the parameters are discretised. As sketched in the figure, the electric power absorbed by the shunt, $P_{sj,i}$, is derived from the voltage drop across the shunt resistor, that is the shunt voltage $v_{sj,i}$. The power signal is then averaged over the past N_s samples and sent to the extremum seeking loop to generate the inductance tuning parameter. This algorithm belongs to the perturb-and-observe type algorithms.

More specifically the tuning parameter $L_{sj,i}$ is modulated with a low frequency harmonic signal $z_{d,i} = Z_0 \sin(\omega_d t_i)$, whose modulation magnitude is adjusted by the gain g_{zL}. As a result, the electro-mechanical response of the plate and shunted piezoelectric patch, and thus the electric power absorbed by the shunt, show the time-harmonic dithering effect.More precisely, when the tuning parameter is lower than the optimal value, i.e., $L_{sj,i} < L_{sj,opt}$, the

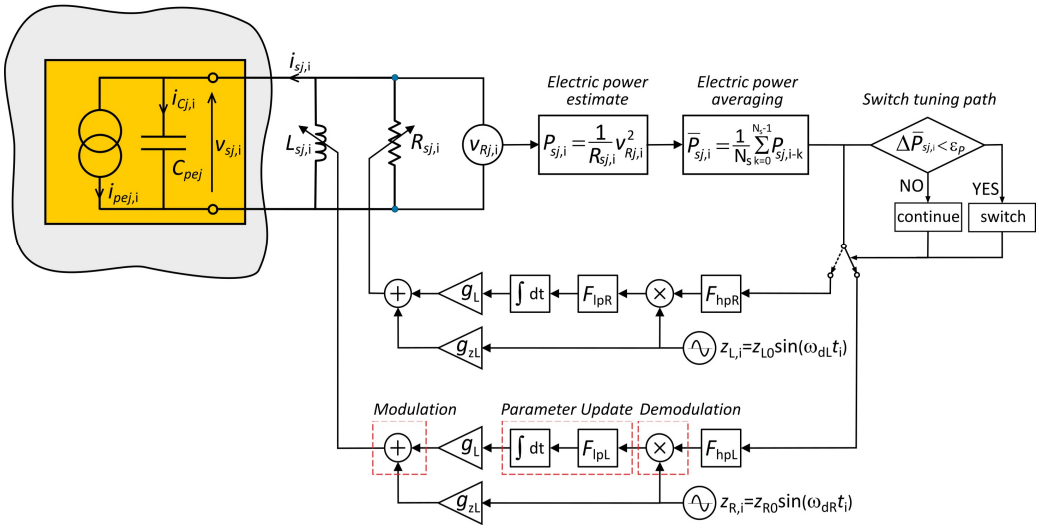

Figure 3.7: Block diagram of the two-paths extremum seeking gradient search algorithm implemented to find the optimal resistance and inductance of the shunt, which maximises the electric power absorption estimated from the electric power dissipated by the shunt resistor.

wavy power signal is in-phase with the dithering signal. Conversely, when the tuning parameter is higher than the optimal value, i.e., $L_{sj,i} > L_{sj,opt}$, the wavy power signal is out-of-phase with the dithering signal. The wavy power signal can thus be used to update the inductance parameter. To this end, the signal is first passed through a high-pass filter $F_{hpL} = \frac{j\omega}{j\omega+\omega_{hp}}$ to remove the bias (ω_{hp} is the filter corner frequency). At this point the signal can be demodulated by multiplying it with the same dithering signal $z_{L,i}$ used in the modulation phase. The resulting wavy signal will be either mostly positive for $L_{sj,i} < L_{sj,opt}$ or mostly negative for $L_{sj,i} > L_{sj,opt}$. The updated tuning parameter $L_{sj,i}$ is then generated by integrating this signal after it has been passed through a low pass filter $F_{lpL} = \frac{1}{j\omega+\omega_{lp}}$ to remove the effects of noise and higher frequency harmonics. The increment or decrement of the updated tuning parameter will be proportional to the slope of the cost function such that fast convergence will be guaranteed along the side branches of the bell-shaped cost function and slow, but precise, tuning will be ensured close to the peak of the cost function where the bell-shape is flatter. This algorithm is bound to converge and oscillate around the maximum value of

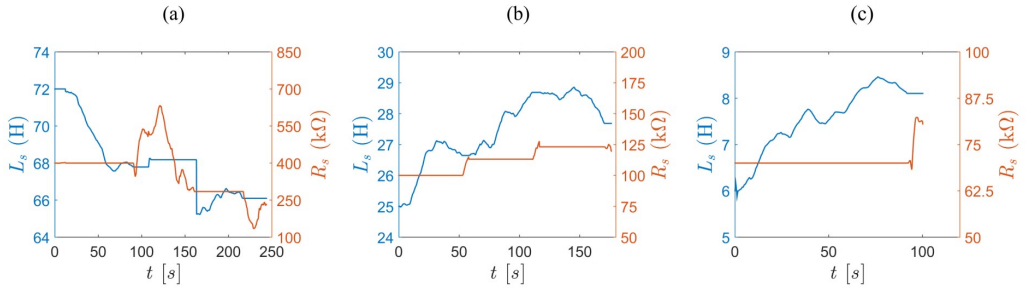

Figure 3.8: Evolutions of the resistance and inductance of the shunt connected to the centre patch when the extremum seeking algorithm is implemented to maximise the time-averaged electric power absorption from the resonant response of the first (a), second (b) and fourth (c) flexural modes.

the power cost function. Therefore, to stop the search along one path and move forward to the search along the other path, as shown in the sketch of Figure 3.7, a switching loop is added to the algorithm such that, when the increment of the averaged absorbed power $\Delta\bar{P}_{sj,i} = \frac{|\bar{P}_{sj,i} - \bar{P}_{j,i-1}|}{\bar{P}_{sj,i-1}}$ is below a given threshold ϵ_P, the search is switched to the other path. It is important to highlight here that the time-window for the N_s samples time-averaging of the absorbed electrical power is much shorter than the period of the dithering signal for the extremum seeking tuning. Thus it does not interfere with the working principle of the extremum seeking algorithm, which is indeed based on the implementation of a dithering tuning signal.

3.4.2 Online tuning

The on-line implementation of the extremum seeking algorithms set to maximise in each control unit the electrical power absorbed by the shunt is finally discussed in this subsection for the cases where the shunts are tuned to control in turn the resonant responses of the first, second and fourth flexural modes of the plate. Figure 3.8 shows the evolutions in time of the resistance and inductance of the shunt connected to the centre patch set to maximise the time-averaged electric power absorbed from the resonant response of the first, second and fourth resonant flexural modes respectively. The three plots show that the tuning of the resistance is much faster than the tuning of the inductance. In this respect, it should be highlighted that a very fine tuning was searched here, that is a fairly small threshold ϵ_P was considered. As can

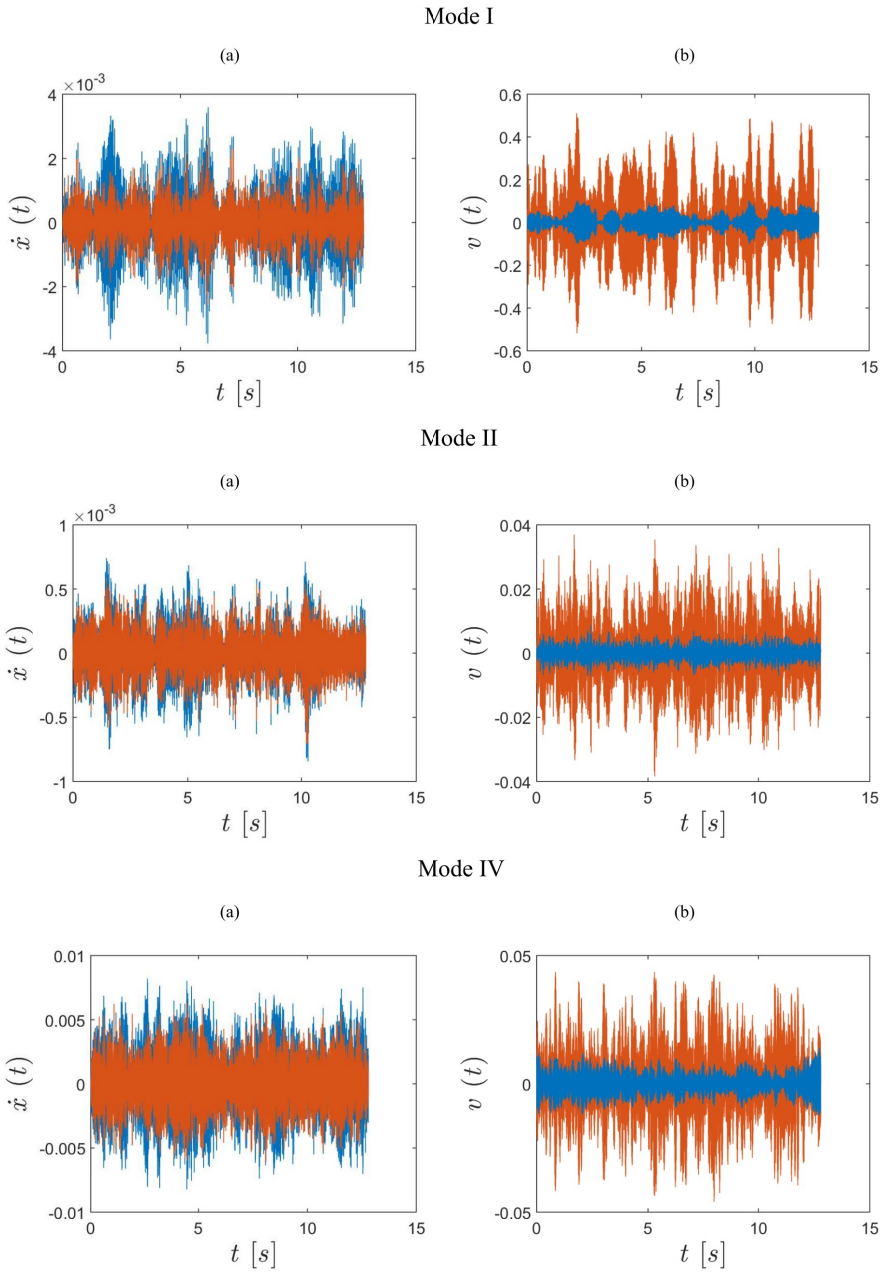

Figure 3.9: Measures of the panel spatially-averaged transverse velocity (a) and voltage drop across the shunt connected to the centre patch when the plate is excited by a stochastic excitation and the patches are either in open circuit (blue lines) or connected to shunts (red lines) set to maximise the time-averaged electric power absorption from the resonant response of the first (top graphs), second (centre graphs) and fourth (bottom graphs) flexural modes.

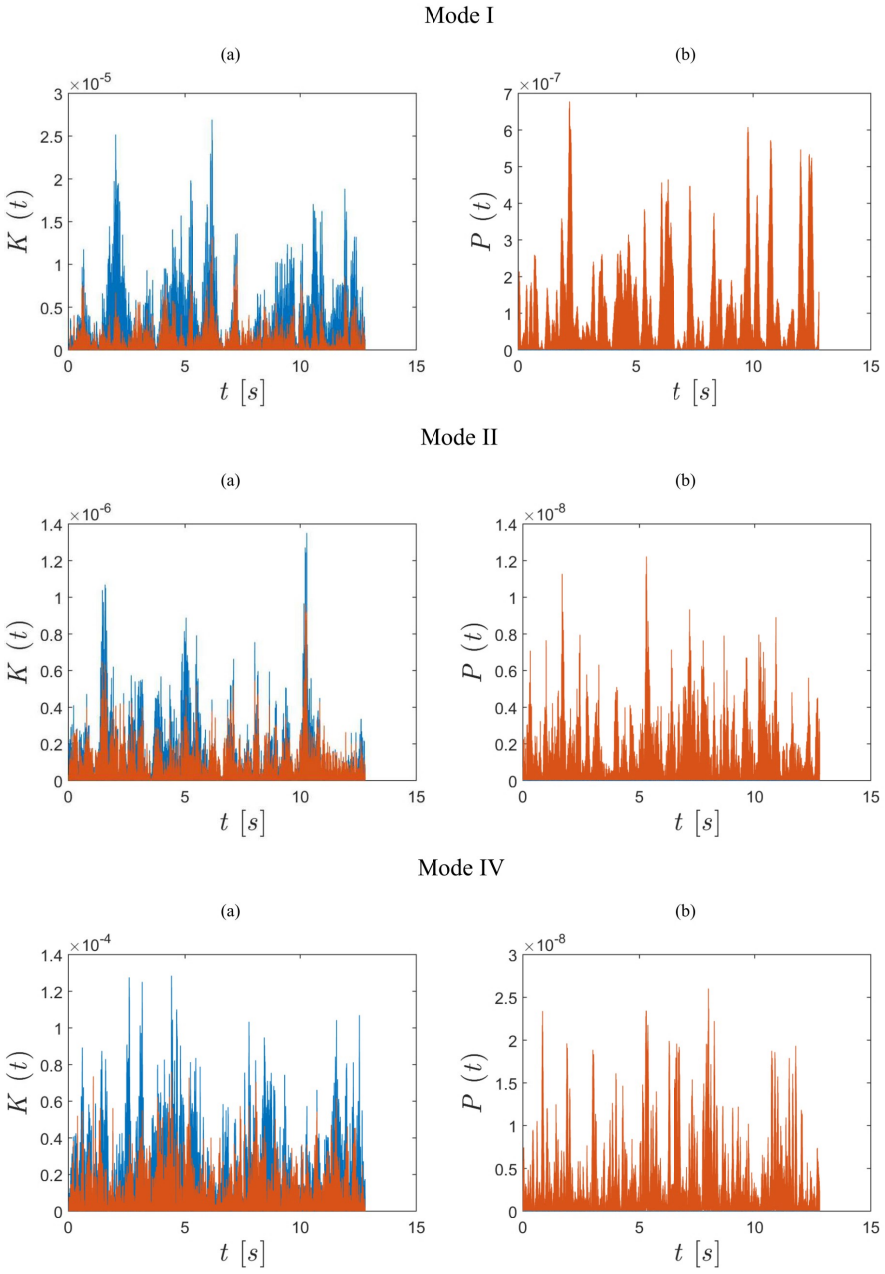

Figure 3.10: Measures of the panel flexural kinetic energy (a) and electric power absorbed by the shunt connected to the centre patch when the plate is excited by a stochastic excitation and the patches are either in open circuit (blue lines) or connected to shunts (red lines) set to maximise the time-averaged electric power absorption from the resonant response of the first (top graphs), second (centre graphs) and fourth (bottom graphs) flexural modes.

be noticed in the maps of Figures 3.3 and 3.4, the monitor and control cost functions are characterised by rather flat surfaces close to the optimal tuning points. Therefore, it is expected that, even with larger threshold ϵ_P, the tuning algorithm will converge to shunt resistance and inductance values that generate nearly optimal electric power absorption and thus nearly optimal reductions of the resonant responses of the target modes. It is important to emphasise a rather important feature of the experiments presented here. Indeed, the online tuning is implemented for the case where the panel is exposed to a stochastic broadband excitation. Therefore, to have a proper estimate of the cost function, that is the time-averaged electric power absorbed by the shunt, rather long time-averages should be implemented. In this respect, to avoid too long convergence times, the length of the time averages was taken equal to ns=12 samples, that is 0.8 s. With this choice, convergence to the optimal tuning parameters was reached in a reasonable timescale, although at the cost of losing some accuracy when the random excitation undergoes rapid and substantial changes. The three graphs show that the tuning time for each mode is different. This is due to two factors. First, the distance from the optimal values of the initial guess for the shunt resistance and inductance was different for the three modes. Second, the profile of the bell shaped cost function was different for the three modes. As a result, a different number of iterations was required before the algorithm climbed to the top of the bell-shaped cost functions to find the optimal inductance and resistance values. In general, when the two tuning paths procedure has been finalised, the tuning algorithm can either be stopped for a while or set to restart form the optimal values. In this way, the shunt parameters are continuously adapted according to changes in the response of the structure, due for example to tensioning effects produced by temperature variations or by the operation condition of the structure. The control effects produced by the shunted piezoelectric patches are now investigated with reference to two configurations where the shunts either implement very large resistances to mimic open circuits or implement the optimal resistances and inductances found with the extremum seeking tuning algorithm set to maximise the electric power absorption from the resonant responses of the first, second and fourth flexural modes respectively. The left hand side columns in Figures 3.9 and 3.10 show the spatially average velocity and the total flexural kinetic energy derived from measurements of the transverse velocity taken at a grid of 4×4 points with a scanner laser vibrometer. The right hand side columns in Figures 3.9 and 3.10 show, for the centre control unit, the measured voltage drop across the terminals of the shunt and the electric power absorbed by the shunt estimated from the voltage drop across the terminals of the shunt and the resistance implemented in the shunt. To better emphasise the vibration control effects produced

by the shunted piezoelectric patches, the force excitation and the measured responses of the panel and shunt were filtered with a 20 Hz band pass filter centred at the target resonance frequency. Also, to allow a fair comparison, the same stochastic force excitation was implemented to produce the results with open circuit and shunted piezoelectric patches.

The left hand side plots in Figure 3.9 show that the amplitude of the spatially averaged transverse vibration velocity of the panel is substantially reduced when the units are set to control the resonant response of the first and fourth flexural modes of the panel (top and bottom graphs). There is also a fair reduction of the resonant response of the second flexural modes of the panel (centre graph). Nevertheless, it is important to highlight that these plots show the spatially-averaged velocity. Typically, vibro-acoustic phenomena are assessed with reference to energy levels. Therefore, to better appreciate the control effect produced by the five control units, the total flexural kinetic energy plots shown on the left hand side column of Figure 3.10 should be considered. Indeed, these graphs show quite remarkable reductions of the resonant responses of the first, second and fourth flexural modes respectively. Considering time-average levels taken over the 13 s time-acquisition, the ratios of the kinetic energy when the units are optimally shunted and in open circuit are of the order $\bar{K}_{sh}/\bar{K}_{oc} = 0.2$ or mode 1, $\bar{K}_{sh}/\bar{K}_{oc} = 0.63$ for mode 2 and $\bar{K}_{sh}/\bar{K}_{oc} = 0.4$ for mode 4, which, translated into dB, result in reductions of 14dB for mode 1, 4dB for mode 2 and 8dB for mode 4. These results are in line with the reductions found with the spectral analysis presented in Section 3.3.2 – Figure 3.6 and thus confirm both the validity of the proposed tuning approach based on the maximisation of the electric power absorption of the shunt and the effectiveness of the extremum seeking tuning algorithm. Moving to the electric response of the shunt connected to the centre patch, the right hand side graphs in Figures 3.9 and 3.10 show that the voltage drop across the shunt terminal, and consequently the absorbed power too, rise significantly when the shunt is indeed set to maximise the time-averaged electric power absorption. The graphs in Figure 3.9 show both the absolute power absorbed by the large resistor mimicking the open circuit condition (blue line), which is therefore rather low, and the much larger power absorber by the resistor of the optimally tuned shunt (orange line). In contrast, the graphs in Figure 3.10 seem to show only the electric power absorbed when the shunts are optimally tuned (orange line). As a matter of fact, the graphs report the electric power absorbed when the shunts are in open circuit too, although the values are so small compared to those of the power absorbed by the optimally tuned shunt that the lines are merely visible (blue lines).

Chapter 4

Piezoelectric patch vibration control units connected to a multi-resonant self tuning shunt

---

4.1 Introduction

This Chapter investigates the implementation of the piezoelectric patch control unit connected to a self-tuning shunt. As proposed in the previous chapters, the approach proposed is based on the maximisation of the time-averaged electric power absorbed by each RLC branch of the shunts relative to the resonant responses of the target modes. In this chapter, the approach is extended to multi-resonant shunts set to control the resonant responses of multiple target modes. The search of the maximum time-averaged electric power absorption local cost function is implemented with the perturb and see approach based on the extremum seeking algorithm introduced in Section 2.4 and discussed further in Section 3.4.1 with respect to its practical implementation in a single resonant shunt.

4.1.1 Modular self tuning multi-resonant shunt for piezoelectric vibration control units

This chapter reports experimental results on the mitigation of the low-frequencies, multi-resonant flexural vibration of a plate subject to a broadband random disturbance. The plate is equipped with five piezoelectric patches connected to self-tuning shunts set to control the resonant response of three target flexural modes. The shunts are composed by three parallel branches, with each branch made by a resistor-inductor-capacitor (RLC) in series. To simplify the experimental work, the shunt circuits are implemented in a dSPACE multichannel digital board, which is connected to the five piezoelectric patches via ad-hoc interface circuits [95], such that the transfer functions implemented in the board are converted into the desired impedance loads that should be exerted by the multi-resonant shunts on the five piezoelectric patches. The study first contrasts the vibration control effects produced by the multi-resonant shunts with respect to the reference cost function given by the time-averaged total flexural kinetic energy of the panel and the proposed cost function given by the time-averaged electric power absorbed locally by each branch of the shunts. Both cost functions are filtered in a narrow band centred on the resonance frequency of the target mode. Next, it investigates the online tuning of the resistive and inductive components of the multi-resonant shunts with an extremum seeking algorithm set to maximise the proposed local cost function, that is the time-averaged electric power absorbed by each branch of the multi-resonant shunts.

4.1.2 Structure of the chapter

This Chapter is structured into three sections. Firstly, Section 4.2 presents the plate structure studied in this paper. Also, it discusses the interface circuits and dSPACE multi-channel digital board arrangement used to implement the multi-resonant shunts composed by three RLC branches in parallel and the perturb-and-see self-tuning approach based on the extremum seeking algorithm. Section 4.33 contrasts the maps of the time-averaged flexural kinetic energy of the panel reference cost function and the time-averaged electric power absorbed by the branches proposed cost function, both filtered in narrow frequency bands centred at the resonance frequency of the target flexural modes, with respect to the RL components in the three branches of the shunts. Next, Section 4.4 presents the online self-tuning of the three branches of each shunt in order to maximise the time-average electric power absorption from the resonant response of the target modes.

4.2 Plate model structure equipped with digital shunts and measurement approaches

This study is focused on the broadband control of flexural vibration in a thin rectangular steel panel. As depicted on Figure 4.1, the plate is fixed on a rigid frame isolated from ground vibrations. The panel is equipped with five square MFC piezoelectric patches [117]. The patches are bonded on one side of the panel and electrically connected via an interfacing circuit to a multi-channel dSPACE digital controller board, which implements the digital shunts as well as the online self-tuning algorithm. The dSPACE controller has 16-bit ±10 V converters for both analogue-to-digital (ADC) and digital-to-analogue (DAC) channels, with the sampling frequency set at 48 kHz. The plate is excited by a broadband white noise transverse point force with a shaker connected to the plate via a force sensor and a stinger. A detailed list of geometric and physical dimensions of the system is given in Table 4.1.

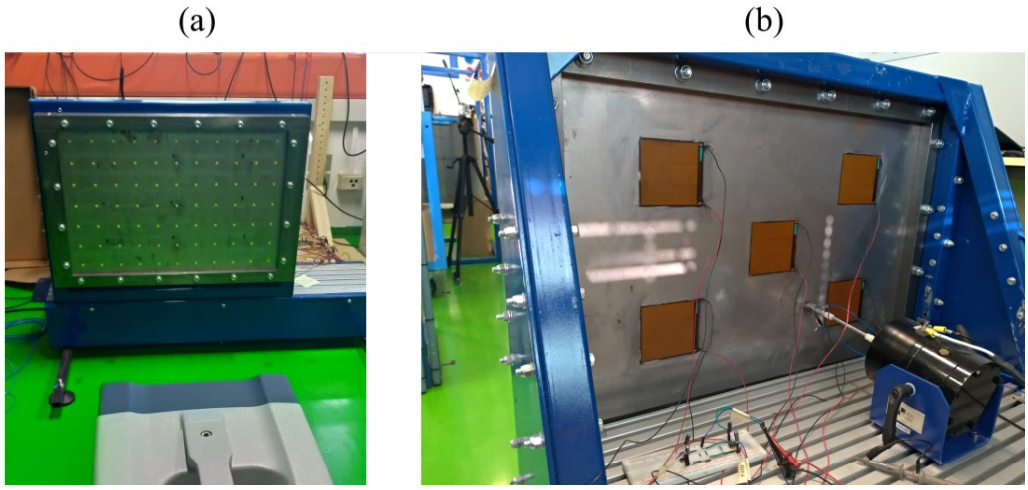

Figure 4.1: Thin panel model structure (a), which is equipped with five piezoelectric patches connected to ad hoc interface circuits (b).

4.2.1 Multi-resonant digital shunt

The electrical scheme of the multi-resonant shunt utilised in this work is adapted from the circuit proposed by Hollkamp [131]. As shown in Figure 4.2(b), in this work, the shunt implements three parallel branches composed

Table 4.1: Plate and piezoelectric patches rig.

Parameter	**Steel Plate**	**Piezoelectric patches**
dimensions	$l_{xp} \times l_{yp} = 668 \times 443$mm	$l_{xpe} \times l_{ype} = 85 \times 85$ mm
thickness	$h_p = 1.8$ mm	$h_{pe} = 0.3$mm
mass	$m_p = 3,7926$kg	$m_{pe} = 11.7$g
point force position	$x_p = 0.63l_{xp}, y_p = 0.25l_{yp}$	
patches centre position		$\frac{l_{xp}}{2}, y_{pe1} = \frac{l_{yp}}{2}$ $x_{pe2,3,4,5} = \frac{l_{xp}}{2} \pm \Delta_x$, $y_{pe2,3,4,5} = \frac{l_{yp}}{2} \pm \Delta_y$ $\Delta_x = 185mm, \Delta_y = 117.5mm$

by a resistor-inductor-capacitor (RLC) in series. This circuit topology ensures each branch can be focused on a narrow frequency band, which is indeed defined by the second order response of the series RLC branch [127]. The centre frequency and bandwidth of the branch filtering effect results from the combined capacitive-inductive and the resistive effects of the branch components. Here, it is important to emphasise that, to generate the desired vibration absorption, the branch inductive-capacitive components should be fixed in such a way as they produce a resonance effect that approximately matches the resonance frequency of the target flexural mode of the plate [66]. Moreover, to maximise the electric power absorption, that is to maximise the flexural vibration power absorption, the shunt resistance is bound to have a comparatively low value, otherwise there would be no current flow in the branch and thus no power absorption. As a result, the filtering effect of RLC branch is bound to be characterised by a narrow frequency band too.

As seen in section 3.4.1 for the single branch shunt, the actual implementation of the shunts was made by digitally mimicking the circuit shown in Figure 4.2(b) with a multichannel dSPACE board connected to the piezoelectric patches via the interface circuit shown in Figure 4.2(c). Considering the electric circuit depicted in Figure 4.2(c) for the j-th shunt, assuming time-harmonic functions given in the form $f(t) = f(\omega)\exp(j\omega t)$, where $f(\omega)$ is the complex amplitude $j = \sqrt{-1}$ and ω is the circular frequency, the following equations can be derived straightforwardly in the frequency domain:

$$v_{inj}(\omega) = v_{sj}(\omega), \tag{4.1}$$

$$v_{opj}(\omega) = G_{sj}(\omega)v_{inj}(\omega), \tag{4.2}$$

$$v_{sj}(\omega) - v_{opj}(\omega) = R_{oj}i_{sj}(\omega). \tag{4.3}$$

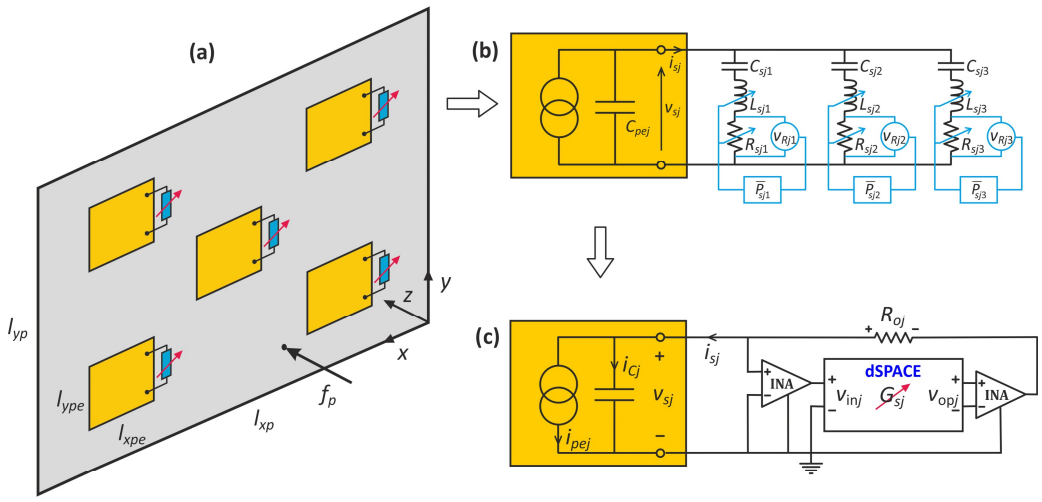

Figure 4.2: Sketches of (a) the plate and shunted piezoelectric patches, (b) shunt circuit with three RLC branches in parallel each equipped with a self tuning loop that maximises the electric power absorbed by the branch, (c) interface circuit and dSPACE platform for the digital implementation of the shunts.

Here, $v_{sj}(\omega)$, $i_{sj}(\omega)$, $v_{inj}(\omega)$, $v_{opj}(\omega)$ are the complex amplitudes of the shunt voltage and current and of the digital board input and output voltages, $G_{sj}(\omega)$ is the frequency response function between the output and input channels board pair of the dSPACE for the j-th shunt and R_{oj} is the feedback resistance used to generate a given current flow. The voltage across the terminals of the piezoelectric patch can be written as

$$v_{sj}(\omega) = Z_{sj}(\omega) i_{sj}(\omega), \tag{4.4}$$

where $Z_{sj}(\omega)$ is the impedance of the multi-resonant shunt, which, for the parallel RLC branches is given by

$$Z_{sj}(\omega) = \left(\sum_{i=1}^{n} \left(\frac{1}{(j\omega C_{sji})} + j\omega L_{sji} + R_{sji} \right)^{-1} \right)^{-1}, \tag{4.5}$$

where n is the number of branches, which in this work will be taken equal to $n = 3$. At this point, combining Eqs. 4.1-4.4, the frequency response function $G_{sj}(\omega)$ that should be implemented digitally in the digital board to generate

desired the electric impedance load of the shunt $Z_{sj}(\omega)$ results given by

$$G_{sj}(\omega) = \frac{v_{opj}(\omega)}{v_{inj}(\omega)} = 1 - \frac{R_{oj}}{Z_{sj}(\omega)}. \tag{4.6}$$

To ensure that the $G_{sj}(\omega)$ is proper and to reduce eventual high frequency noise a low pass filter with a cut-off frequency at $f_{lp} = 500$ Hz is implemented too by setting

$$G_{sj}(\omega) = \Big(1 - \frac{R_{oj}}{Z_{sj}(\omega)}\Big)\Big(\frac{\omega_{\rm lp}}{j\omega + \omega_{\rm lp}}\Big). \tag{4.7}$$

Here $\omega_{\rm lp} = 2\pi f_{lp}$ is the cut off circular frequency of the low pass filter.

4.2.2 Measurement of the cost functions

As anticipated above two cost functions have been considered for the tuning of the multi-resonant shunts. The first, serves as a reference cost function to assess the actual effectiveness of the proposed cost function. Therefore the reference cost function is given by the time-averaged total flexural kinetic energy relative to the resonant responses of the target modes, which has been derived from the following relation

$$\bar{K}_r(R_{sj}, L_{sj}) = \frac{1}{\pi\Delta\omega_r} \sum_{r=-N_\Delta}^{+N_\Delta} S_{Kr}\Big(R_{sji}, L_{sji}, \omega_{nr} + r\frac{\Delta\omega_r}{2N_\Delta}\Big). \tag{4.8}$$

Here R_{sji}, L_{sji} are the resistance and inductance of the i-th branch in the j-th shunt. Also, ω_{nr} is the resonance frequency of the r-th target mode to be controlled and $\Delta\omega_r$, $2N_\Delta$ are respectively the frequency bandwidth and the number of frequency samples in the bandwidth used to derive the average value, which are summarised in Table 4.2. Finally, S_{Kr} is the power spectral density of the total flexural kinetic energy, which was derived from point measurements taken with a laser vibrometer using the following formula

$$S_{Kr}\Big(R_{sji}, L_{sji}, \omega_{nr} + r\frac{\Delta\omega_r}{2N_\Delta}\Big) = \frac{M}{32}\sum_{k=1}^{+16} S_{wkji}\Big(R_{sji}, L_{sji}, \omega_{nr} + r\frac{\Delta\omega_r}{2N_\Delta}\Big). \tag{4.9}$$

Here, M is the total mass of the plate and piezoelectric patches and S_{wkji} is the power spectral density of the transverse vibration velocity of the plate measured at the k-th point of the 4×4 grid of points scanned with the laser vibrometer. The rather coarse 4×4 grid of measurement point was adopted

Table 4.2: Mode frequency ranges

	Min	**Max**
1st mode (ω_1)	26 Hz	33 Hz
2nd mode (ω_2)	47 Hz	51 Hz
3rd mode (ω_3)	78 Hz	83 Hz
4th mode (ω_4)	85 Hz	92 Hz

based on a trade-off between accuracy of the measurements and speed of the measurements. The speed of the measurements was quite critical for the generation of the maps considered in the forthcoming section, which depict the time-averaged total flexural kinetic energy with respect to a 10×25 grid of resistance and inductance values in each branch of the shunts. Even with such a coarse grid for the laser vibrometer measurements, and the likewise coarse grid of resistance of vibration measurement points, these measurements took a rather long time in the order of several hours. Beside the length of the experiments itself, this was a problem since even under a controlled environment, the flexural response of the panel was affected by a certain variability due primarily to the temperature variations in the plate and the shunt equipment. over several hours, thus changes in temperature are, in fact, observable on the measurements. Therefore, the frequencies will be omitted and instead, just the mode order will be displayed. Table 4.2 shows the ranges of frequencies for the modes compressed between 0 and 100Hz.

Beside the reference cost function, a local cost function is proposed in this paper, which is based on local measurements of the time-averaged electric power absorbed by each RLC branch relative to the resonant responses of the target modes. This cost function is of particular practical interest as it does not need a sophisticated sensing system that detects the whole vibration of the panel such as those involving distributed piezoelectric transducers for example [127]–[130]. On the contrary, as highlighted in Figure 4.2a, it can be estimated directly within each branch of the shunt from the voltage across the branch resistor. Indeed, the time-averaged electric power absorbed by the i-th branch of the j-th shunt with respect to the resonant response of the r-th flexural mode of the panel was derived from the following relation

$$\bar{P}_r(R_{sj}, L_{sj}) = \frac{2N_\Delta}{\pi \Delta\omega_r} \sum_{r=-N_\Delta}^{+N_\Delta} S_{Prji}\Big(R_{sji}, L_{sji}, \omega_{nr} + r\frac{\Delta\omega_r}{2N_\Delta}\Big). \tag{4.10}$$

The parameters R_{sji},L_{sji} and ω_{nr}, $\Delta\omega_r$, $2N_\Delta$ are the same as those defined for Eq. 4.6. However, S_{Prji} is the power spectral density of the electric power

absorbed by the i-th branch of the j-th shunt, which was derived from the voltage measurement across the resistor in the i-th branch using the following formula

$$S_{Prji}\Big(R_{sji}, L_{sji}, \omega_{nr} + r\frac{\Delta\omega_r}{2N_\Delta}\Big) = \frac{1}{R_{sji}} S_{vji}\Big(R_{sji}, L_{sji}, \omega_{nr} + r\frac{\Delta\omega_r}{2N_\Delta}\Big). \quad (4.11)$$

where S_{vji} is the measured powers spectral density of the voltage drop across the resistor in the i-th branch. As will be discussed in Section 4, the proposed self-tuning of the multi-resonant shunts was implemented online considering directly the average of the instantaneous absorbed electric power over a short window of N_s samples, such that

$$\bar{P}_r(R_{sj}, L_{sj}) = \frac{1}{N_s} \sum_{s=0}^{N_s-1} P_{srji}(R_{sji}, L_{sji}). \quad (4.12)$$

Here $P_{srij}(R_{sji}, L_{sji})$ is the electric power absorbed by the i-th branch of the j-th shunt at the s-th time sample, which is band pass filtered at the resonance frequency of the r-th target flexural mode. This quantity was derived directly from the voltage $v_{sji}(R_{sji}, L_{sji})$ measured across the resistor R_{sji} with the following relation

$$P_{sji}(R_{sji}, L_{sji}) = \frac{1}{R_{sji}} v^2_{sji}(R_{sji}, L_{sji}). \quad (4.13)$$

4.3 Global vs. local tuning cost function

In this section, the effectiveness and the tuning of the reference and proposed tuning cost functions are investigated in details. As anticipated above, the reference cost function is based on the global measurement of the flexural response of the plate structure, which is expressed in terms of the time-averaged total flexural kinetic energy relative to the resonant responses of the target modes as given in Eq. 4.8. Alternatively, the local cost function is based on the local measurement of the vibration energy absorbed by the shunted piezoelectric patch and is expressed in terms of the time-averaged electric power absorbed by each RLC branch relative to the resonant responses of the target modes as given in Eq. 4.10. To this end, the maps presented in Figure 4.3 have been produced from measurements of the two cost functions with respect to a 10×25 grid of resistance and inductance values in each branch of the shunts. The left hand side maps show the kinetic energy

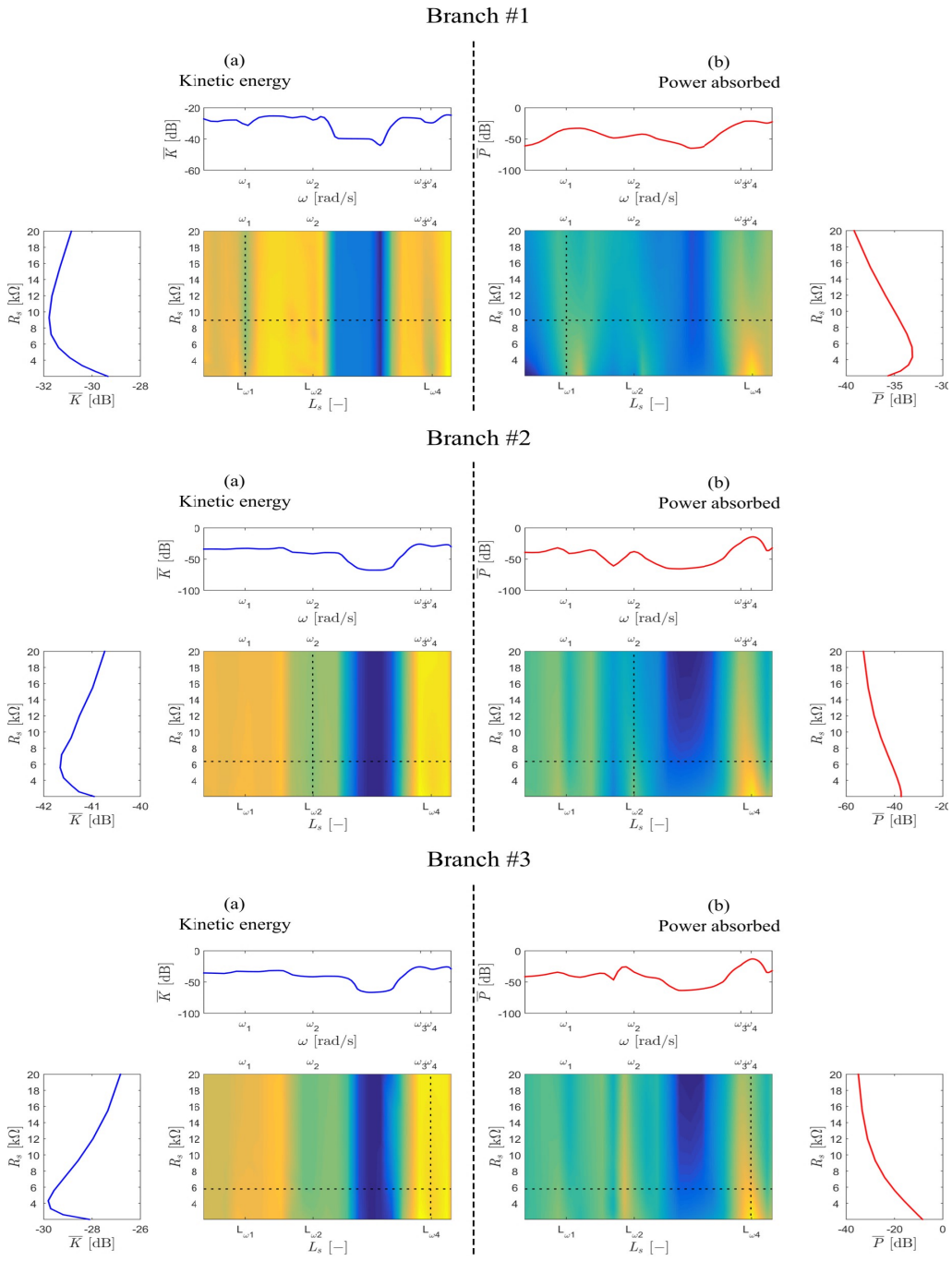

Figure 4.3: Measured maps of the time-averaged total flexural kinetic energy (left hand side plots) and time-averaged electric power absorbed by the shunt branches (right hand side plots) with reference to the inductance and resistance of the branch #1 (top maps), #2 (centre maps) and #3 (bottom maps). Top plots, slices of the maps for constant resistance. Lateral plots, slices of the maps for constant inductance.

cost function whereas the right hand side maps show the electric power cost functions with reference to the inductance (x-axis) and resistance (y-axis) of the first out of one branch (top maps), of the second of two branches (centre maps) and of the third out of three branches (bottom maps). The plots on top of the maps show slices of the kinetic energy and electric power maps for constant shunt resistance. Alternatively, the plots alongside the maps show slices of the kinetic energy and electric power maps for constant shunt inductance. Although the two maps are not smooth, they show the typical reversed bell shapes (kinetic energy maps) and bell shapes (electric power maps) that were found in the theoretical and experimental studies presented for single-resonant shunts in Refs. [118], [132]. As anticipated in Section 4.2.2, to generate the maps, rather lengthy measurement sessions were required such that the results are affected by variations of the plate flexural response and shunt electric response, both due principally to variations of temperature. To keep the acquisition time within a few hours, the overall flexural vibration of the plate was measured over a small grid of 4×4 points. Also, the maps were generated by interpolating the values of the two cost functions measured considering a coarse grid of 10×25 resistance and inductance values in each branch of the shunts. Despite these measurements and plotting artefacts, the maps depicted in Figure 4.3 show the typical inverse bell shaped kinetic energy surfaces and the typical bell shaped electric power surfaces. More specifically, the bell shapes of both maps are characterised by constant-resistance and constant-inductance principal axis. The reversed bell shapes of the flexural kinetic energy maps are centred at the resonance frequencies of the target modes. Thus, as found for the single-resonant shunts, the inductance in each branch should be tuned in such a way as the branch resonates at the resonance frequency of the target flexural mode. The bell shapes of the electric power maps are centred at the resonance frequencies of the target modes too. Actually, the resistance and inductance values of the maxima of these maps closely overlap those for the minima of the flexural kinetic energy maps. Hence, the N-resonant shunts can be conveniently tuned in such a way as the shunted piezoelectric patches control the resonant response of N-target flexural modes of the plate simply by setting the resistance and inductance in each branch to maximise the electric power absorption by the branch itself. As shown in Figure 4.2(c) and discussed in Section 2.2, the electric power absorbed by the shunt can be easily measured locally from the voltage drop across the resistor in the branch and its resistance value itself (e.g. see Eqs. 4.12, 4.13). The fact that the bell shape of the electric power cost function is characterised by constant-resistance and constant-inductance principal axis suggests that the maximum value can be conveniently searched along constant-resistance and constant-inductance paths, which, as can be

noticed in the top and lateral graphs, are equally characterised by bell-shaped functions. Therefore, a two-paths strategy can be implemented in each branch to search in turn the resistance and inductance that would maximise the electric power absorbed by the branch. The inductance should be tuned first along the path $R_s = \text{const}$ and then the resistance should be tuned along the path $L_s = \text{const}$. This sequence can then be implemented recursively to improve the tuning accuracy and, more importantly, to adapt the tuning to changes in the flexural response of the plate and electro-mechanical response of the piezoelectric patch and shunt circuit generated by external factors such as temperature variations. The following section will discuss the online implementation of this tuning strategy, where the climbing of the $R_s = \text{const}$ and $L_s = \text{const}$ paths to find the maximum of the electric power absorption is carried out with a perturb and see algorithm based on the extremum seeking control algorithm [103]–[107].

4.4 Online implementation of the self-tuning shunts

To start with, the experimental implementation of the extremum seeking perturb and see algorithm employed to search the optimal inductance and resistance values in each branch of the shunts is presented. Then, experimental results showing how the shunt inductance and resistance vary during tuning are presented. Finally, the flexural response of the plate and the electric power absorbed by each branch of the shunts before and after tuning is analysed both in the time and frequency domains.

4.4.1 Extremum seeking algorithm for the self-tuning of the RL shunt components in each branch of the multi-resonant shunt

For brevity, only the inductance tuning phase will be addressed in this section considering the block diagram in Figure 4.4 since the tuning of the resistance is very much the same. Considering a time-discrete controller, the ripple signal with the k-th time signal is given by:

$$\tilde{r}_{\mathrm{j,k}} = r_0 \sin(\omega_d t_k), \tag{4.14}$$

with amplitude r_0 and circular frequency ω_d. This signal is amplified by a gain g_{rL} and then added to the tuning inductance signal $\widehat{L}_{\mathrm{j,k}}$ to create a

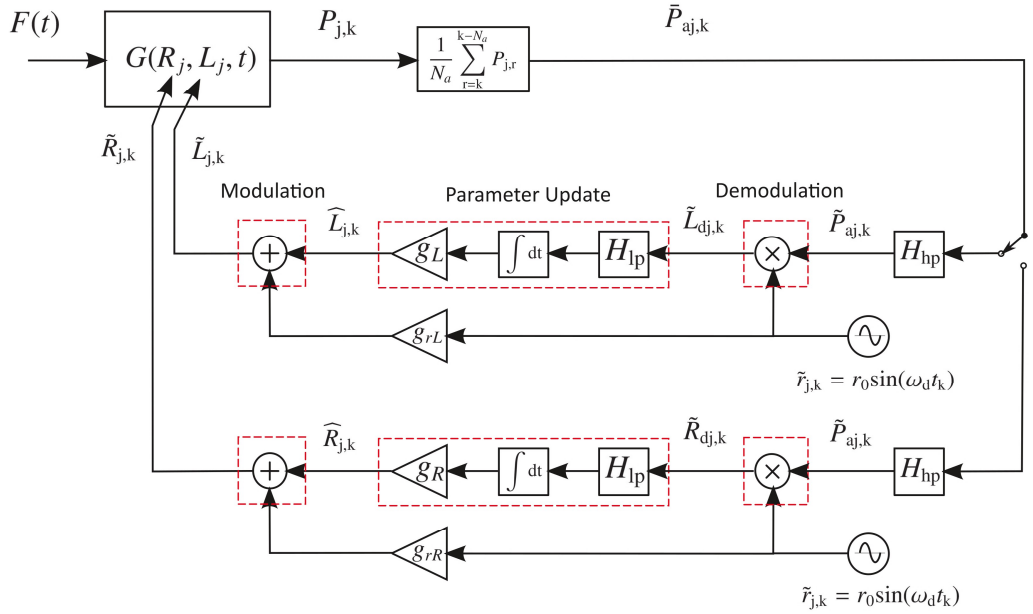

Figure 4.4: Extremum seeking algorithm block diagram.

modulation signal given by:

$$\tilde{L}_{\mathrm{j,k}} = \widehat{L}_{\mathrm{j,k}} + g_{rL}\tilde{r}_{\mathrm{j,k}}. \tag{4.15}$$

This quasi-static variation of $\tilde{L}_{\mathrm{j,k}}$ modulates the value of the electric power absorbed by the shunt, which can be defined as the sum of two power terms

$$P_{\mathrm{j,k}} = \widehat{P}_{\mathrm{j,k}} + \tilde{P}_{\mathrm{j,k}}. \tag{4.16}$$

The first term, $\widehat{P}_{\mathrm{j,k}}$, is the static absorbed power related to the $\widehat{L}_{\mathrm{j,k}}$ tuning component whereas the second term $\tilde{P}_{\mathrm{j,k}} = \sigma_P \tilde{r}_{\mathrm{j,k}}$ encompasses the ripple signal whose amplitude is scaled by a factor σ_P. Then, a time-averaged electric power absorbed by the branch is calculated. As depicted in the block diagram of Figure 4.4, the power signal measured in the shunt is averaged over a small interval of time, that is over a small number of samples N_a, such that:

$$\widehat{P}_{\mathrm{aj,k}} = \frac{1}{N_a}\sum_{\mathrm{r=k}}^{\mathrm{k}-N_a} P_{\mathrm{j,r}}. \tag{4.17}$$

In general, the averaging time interval given by $T_a = N_a T_s$, where T_s is the sampling time of the dSPACE board, is chosen in such a way as it does not remove the modulation of $P_{\mathrm{j,k}}$. Thus, it is considerably shorter than the time period of the dithering signal $T_d = \frac{2\pi}{\omega_d}$. From this step, the algorithm follows as presented and discussed on section 2.4. To mitigate noise and improve convergence, a low pass filter is introduced before the integration step

$$H_{\mathrm{lp}}(j\omega) = \frac{\omega_{\mathrm{lp}}}{j\omega + \omega_{\mathrm{lp}}}, \tag{4.18}$$

having cut-off frequency ω_{lp}, and then it is integrated and magnified such that

$$\widehat{L}_{\mathrm{j,k}} = g_L \sum_{r=k}^{k-N} \tilde{L}_{\mathrm{j,r}} \Delta t. \tag{4.19}$$

where $\widehat{L}_{\mathrm{j,k}}$ is the estimator for the optimal value of the inductance of the shunt.

4.4.2 Online tuning of the multi-resonant shunts

The online implementation of the self-tuning multi-resonant shunts is now investigated considering experimental results obtained with the plate equipped with five piezoelectric patches connected to multi-resonant shunts described in Section 4.2 and depicted in Figures 4.1, 4.2. The shunts are formed by 3 RLC branches in parallel, which are tuned to control the resonant responses of the first, second and fourth flexural mode of the plate. The third flexural mode is not controlled since it is poorly excited by the point force exerted by the shaker and thus generates a small vibration effect anyhow. To simplify this analysis, the tuning of each branch is carried out simultaneously in the five shunts. Therefore, the optimal inductance and resistance of the i-th branch of the shunts is derived for all shunts together considering the total power absorbed by the i-th branch of the N shunts. This simplification is made possible by the fact that, contrary to time-harmonic vibrations [111], for stochastic vibrations the power absorbed by each shunt is independent from that of the other shunts.

Figure 4.5 shows the time evolution of the shunt resistance and inductance, for the first (plot a), second (plot b) and third (plot c) branches. Here, the most relevant aspect is the convergence of the inductance and resistance in each branch to their optimal values. In this respect, to match the resonances

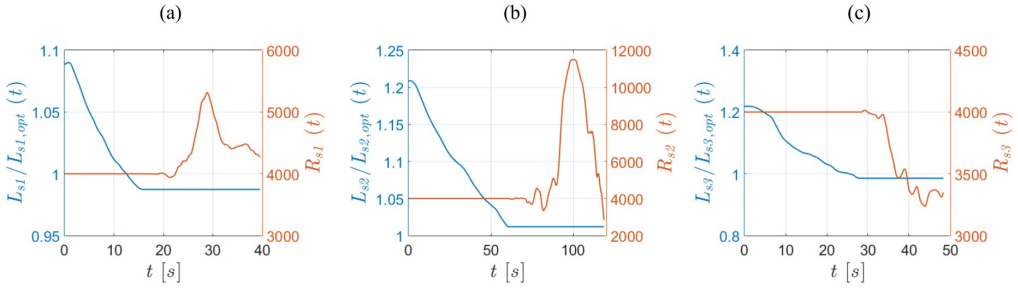

Figure 4.5: Online tuning for the inductances (blue lines) and resistances (orange lines) for the first (a), second (b) and third (c) branch of the shunts set to control the resonant response of the first, the second and the fourth flexural mode of the plate respectively.

of the RLC branches with the resonance frequency of the target modes, the optimal inductances assume rather different values. Therefore, they have been plotted with respect to their optimal values obtained from the maps of the time-averaged electric power absorbed by each branch discussed in Section 3 and depicted in Figure 4.3. Considering first the tuning of the inductances, the blue lines in the three plots of Figure 4.5, show that the inductances in the three branches monotonically approach their optimal values. The tuning of the inductances in the first and third branches is comparatively faster than for the inductance in the second branch. Nevertheless, it should be highlighted here that the convergence time is linked to the initial value of the inductances. Therefore, it is likely that, in practical applications, after the shunts are initially set after production of the smart panel, the online tuning is bound to be rather fast. Moving to the tuning of the resistances, the orange lines in the three plots of Figure 4.5, show that the resistance in the three branches do not converge monotonically. In particular, the resistances of the first and second branch initially exceed their optimal values and then monotonically converge to their optimal values. This is due to the fact that, as can be noticed in the lateral plots beside the electric power maps in Figure 4.3, the curvature of the tuning path for constant inductance is rather small. As a result, the extremum seeking algorithm can easily "surpass" the optimal value and then take quite a few iteration before it inverts the direction of the tuning. This problem is exacerbated by the fact that the primary excitation is stochastic and thus their time-averaged electric power is subject to a steady flickering. Nevertheless, the proposed tuning strategy has led to the optimal

values of the inductance and resistance components in each branch such that the shunted patches effectively couple with the target resonant flexural modes.

4.4.3 Time-domain analysis of the control performance

The control effects generated by the self-tuning multi-resonant shunts are now investigated with reference to time-domain measurements taken on the smart panel excited by a broad band force, which, to better highlight the vibration control effect generated on the resonant responses of the flexural modes 1, 2, 4, was low-pass filtered at 100 Hz. To start with, Figure 4.6 shows the spatially averaged transverse velocity of the panel derived from the laser vibrometer measurements at the 4×4 grid of points (left hand side plots) and the voltage measured across the terminals of the shunt connected to the centre patch (right hand side plots), which gives an indication of the electric power absorbed by the shunt itself. The two sets of plots consider two cases where the inductances and resistors in the branches are mistuned (blue lines) and where the inductances and resistor in branch N. 1 (top plots), N. 1, 2 (centre plots) and N. 1, 2, 3 have been tuned with the proposed approach to optimally control the resonant response of the first, first-second and first-second-fourth flexural modes respectively (orange lines). The top plots in the figure show that, when the first branch in the shunts is tuned to mitigate the resonant response of the first mode, there is only a small reduction of the panel averaged velocity. Also, the shunt voltage does not change significantly. Nevertheless, the centre and bottom plots show that, when the first and second branches and when the first three branches are activated, the reduction of the panel averaged velocity and the increment of the shunt voltage become increasingly more visible. The voltage plots are quite uneven and, for instance, indicate a rather large increment of the voltage when the branches 1, 2 are tuned. This is due to the fact that the graphs show what happens with the centre shunt only, which is characterised by the larger voltage increment when branch N. 1, 2 are activated and branch 3 is mistuned.

To better appreciate the effects generated by the multi resonant shunts, the total flexural kinetic energy of the plate and electric power absorbed by the shunt connected to the centre patch are now analysed considering the plots in Figure 4.7. In this figure, the left hand plots show the panel total flexural kinetic energy whereas the right hand side plots show the electric power absorbed by the shunt connected to the centre patch when the inductances and resistors in the branches are mistuned (blue lines) and when

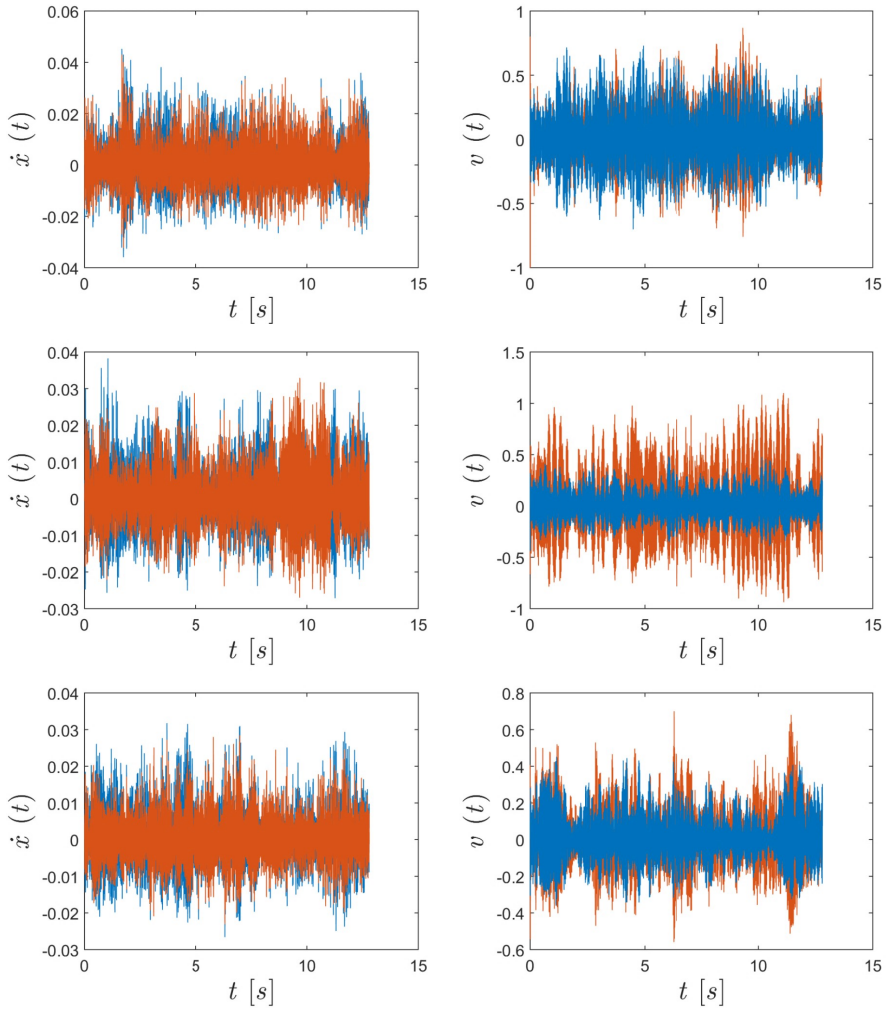

Figure 4.6: Measured time-response of the spatially-averaged velocity of the panel (left hand side plots) and voltage of the centre shunt (right hand side plots) when the branches are mistuned (blue lines) and when the branch N. 1 (top graphs), N. 1, 2 (centre graphs) and N. 1, 2, 3 (bottom graphs) are tuned to control the first, first-second and first-second-fourth flexural modes of the panel.

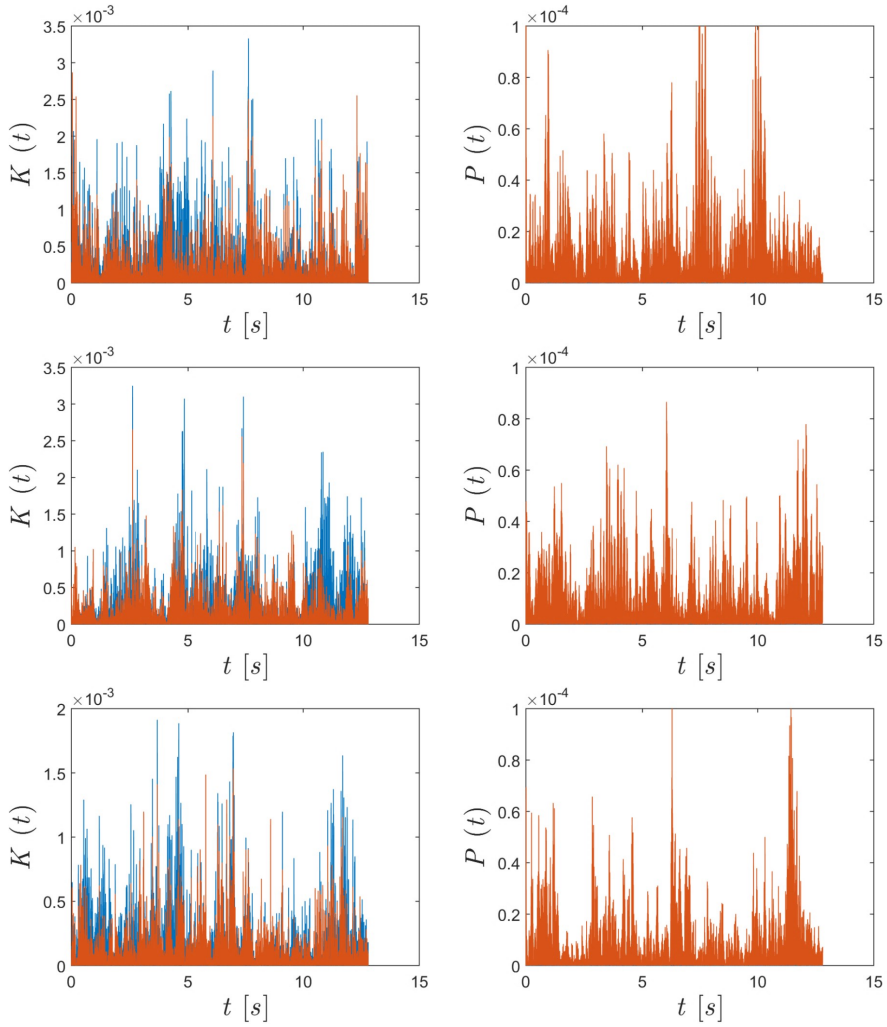

Figure 4.7: Measurement based total flexural kinetic energy (left hand side plots) and electric power absorbed by the centre shunt (right hand side plots) when the branches are mistuned (blue lines) and when the branches N. 1 (top graphs), N. 1, 2 (centre graphs) and N. 1, 2, 3 (bottom graphs) are tuned to control the first, first-second and first-second-fourth flexural modes of the panel.

Table 4.3: Time domain results from Figure 4.7

	1 branch	**2 branches**	**3 branches**
$\bar{K}$ - open circuit	215.23 μJ	179.98 μJ	129.61 μJ
$\bar{K}$ - optimal shunt	158.76 μJ	102.61 μJ	66.63 μJ
$\bar{P}$ - open circuit	49.09 nW	14.60 nW	35.89 nW
$\bar{P}$ - optimal shunt	8210.5 nW	2469.7 nW	5917.1 nW

the inductances and resistor in branch N. 1 (top plots), N. 1, 2 (centre plots) and N. 1, 2, 3 have been tuned with the proposed approach to optimally control the resonant response of the first, first-second and first-second-fourth flexural modes respectively (orange lines). The kinetic energy plots on the left hand side clearly show the reductions of vibration produced by the piezoelectric patches with one, two and three branches activated. Overall, when the three branches are working there is a 6 dB reduction of the time averaged flexural kinetic energy. The right-hand side plots with the electric power show only the orange lines relative to the power absorbed when the centre shunt is tuned to control the resonant responses of the first, first-second, first-second-fourth flexural modes of the plate. This is due to the fact that the powers absorbed when the branches N. 1, N. 1, 2 and N. 1, 2, 3 are optimally tuned, are at least one order of magnitude larger that the power absorbed by the mistuned shunt. Indeed, when the whole three branches are all optimally tuned, the electric power absorption increases by 40 dB. The time averaged results from Figure 4.7 are summarised on Table 4.3. The time averages are given by $\bar{K} = \frac{1}{T}\int_0^T K(t)dt$ and $\bar{P} = \frac{1}{T}\int_0^T P(t)dt$, where T is the averaging time interval and $K(t)$, $P(t)$ are the instantaneous total flexural kinetic energy and electric power absorbed respectively. It is important to highlight here that the plots presented on the top, centre and bottom of Figures 4.6 and 4.7 refer to single acquisitions, which for stochastic vibrations, are bound to have different time-histories, which explains certain discrepancies of results for the three configurations.

4.4.4 Frequency analysis of the control performance

To provide more insights on the control effects and the operation of the multi-resonant shunts, this section presents frequency domain analyses of the panel flexural response and electric power absorbed by the shunt connected to the centre patch. To this end, Figure 4.8 shows the power spectral density of the total flexural kinetic energy (left hand side plots) and the power spectral

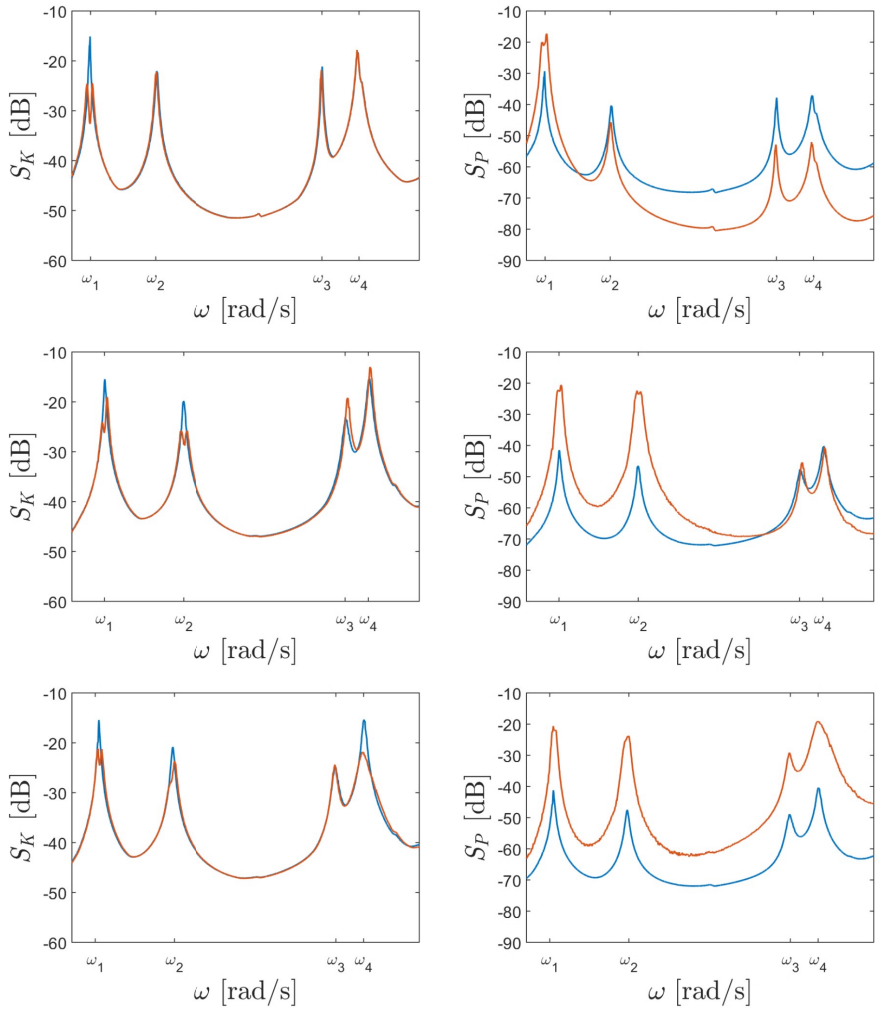

Figure 4.8: Measurement based spectra of the total flexural kinetic energy (left hand side plots) and electric power absorbed by the centre shunt (right hand side plots) when the branches are mistuned (blue lines) and when the branches N. 1 (top graphs), N. 1, 2 (centre graphs) and N.1, 2, 3 (bottom graphs) are tuned to control the first, first-second and first-second-fourth flexural modes of the panel.

densities of the electric power absorbed by the shunt connected to the centre patch (right hand side plots). Here too, the two sets of plots consider the cases where the inductances and resistors in the branches are mistuned (blue lines) and where the inductances and resistor in branch N. 1 (top plots), N. 1, 2 (centre plots) and N. 1, 2, 3 have been tuned with the proposed approach to optimally control the resonant response of the first, first-second and first-second-fourth flexural modes respectively (orange lines). The left hand side plots show that, when the three branches in the shunts are activated in sequence, the first, second and fourth peaks in the flexural kinetic energy spectra, which are due to the resonant responses of the first, second and fourth natural modes, are brought down respectively by 10 dB, 8 dB and 10 dB. In parallel, the right hand side plots show that the spectra of the electric power absorbed by the shunt connected to the centre patch see a substantial increment of the first, second and fourth resonance peaks. Here there is an increment of the third peak too, whose resonance frequency is close to that of the fourth mode. Therefore the response, and thus power absorption linked to the response of the fourth mode overlaps with that of the third mode such that the third resonance peak results magnified. The experimental results presented in this section show the potential of semi-active control with piezoelectric patches connected to self-tuning multi-resonant shunts, which can generate significant reductions of the resonant responses of low order flexural modes of the hosting structure, comparable to those obtained with piezoelectric patches connected to fully active feedback systems [31], [133]–[142].

Chapter 5

Summary and Conclusions

5.1 Overview of the study

This thesis has presented a comprehensive theoretical, simulation and experimental study on a modular control unit formed by a piezoelectric patch connected to a self-tuning shunt, which can be bonded in batches on thin structures to control the low frequency flexural response due to stochastic broadband disturbances. In particular, the focus has been on the conception and development of either a single-resonant or a multi-resonant shunt, which can be tuned online in such a way as to control the resonant response of single or multiple flexural modes of the hosting structure.

The study has considered two tuning strategies, based on a global metric and a local metric. More specifically, the so-called reference tuning strategy refers to the minimisation of the time-averaged total flexural kinetic energy of the hosting thin plate strategy. This cost function provides a global indication of the overall flexural vibration of the panel. Thus, it has been used as a benchmark to assess the effectiveness of the so called practical tuning strategy, which involves the maximisation of the time-averaged electric power absorbed by the RL branch or by each RLC branch of the single-resonant and multi-resonant shunts respectively.

The practical implementation of the self-tuning shunts has been based on a novel two paths tuning approach, based on the extremum seeking perturb-and-see algorithm. The study has been structured in three parts. Firstly, Chapter 2 has presented the proposed self-tuning shunt considering a simplified

mechanical problem encompassing a single degree of freedom spring-mass-damper system connected to the self-tuning shunt via a piezoelectric idealised transducer. Two shunt configurations have been considered, which are formed by a resistor and inductor (RL) connected either in series or parallel. Then, Chapters 3 and 4 have discussed the actual implementation of the proposed control unit on a thin plate structure subject to a stationary stochastic excitation. More specifically, Chapter 3 has investigated the implementation of single-resonant self tuning shunt set to control the resonant response of a target flexural mode of the hosting structure. Instead, Chapter 4 has explored the implementation of multi-resonant self tuning shunt set to control the resonant response of multiple target flexural modes of the hosting structure. The single-resonant shunt is formed by a single branch formed by a resistor and inductor in parallel. The multi-resonant shunt is formed by multiple branches connected in parallel, which are formed by a resistor, inductor and capacitor connected in series. The following section presents the principal conclusions of the studies presented in the three chapters.

5.2 Conclusions

As anticipated above, the conclusions of the study are organised with respect to the results presented in each chapters as detailed below.

5.2.1 Chapter 2 – conclusions

To start with, this chapter has contrasted the minimisation of the time-averaged kinetic energy of the mechanical system with the maximisation of the time-averaged electric power absorbed by the shunt, that is, the time-averaged electric power dissipated by the shunt resistor. The study has shown that:

1. the kinetic energy cost function is characterised by an inverse bell-shape whereas the absorbed electric power objective function is characterised by a bell-shape;
2. both functions are characterised by constant-resistance and constant-inductance principal directions;
3. the minimum of the kinetic energy cost function and the maximum of the absorbed electric power objective function are characterised by the same optimal resistance and inductance of the shunt.

A local tuning strategy has therefore been proposed, where the resistance and inductance of the shunt are set online to maximise the time-averaged electric power absorbed by the shunt, which can be suitably measured locally as the time-averaged electric power dissipated by the resistor. More specifically, a two-paths tuning sequence has been proposed, where the inductance and resistance of the shunt are tuned in sequence along constant-resistance and constant-inductance paths respectively. In this respect, the study has shown that

1. the two paths are characterised by non-convex functions with a single maximum, which identify the optimal inductance and optimal resistance respectively;

2. the optimal inductance and resistance can be effectively searched along the two paths with an extremum seeking gradient search algorithm;

3. the two-paths optimisation can be implemented sequentially online such that the tuning of the shunt is continuously adapted to both changes of the dynamic response of the mechanical system and variations of the electrical response of the piezoelectric transducer capacitance and shunt resistance and inductance.

5.2.2 Chapter 3 – conclusions

At the beginning, this Chapter has also contrasted the vibration control effects generated when the practical control unit formed by a piezoelectric patch connected to the single-resonant shunt is set

(a) either to minimise the time-averaged total flexural kinetic energy of the hosting plate due to the resonant response of the target flexural mode

(b) or to maximise the time-averaged electric power absorbed by the shunt from the resonant response of the target flexural mode.

In line with Chapter 2, Chapter 3 has shown that the two cost functions are characterised by mirrored bell shapes whose minimum and maximum occur for the same RL shunt parameters. Therefore, the shunts can be conveniently tuned locally by maximising the electric power absorbed by the shunts from the resonant response of the target flexural mode.

In the second part, the Chapter has investigated the practical implementation of the two-step tuning approach proposed in Chapter 2, where

the extremum seeking algorithm is implemented online to find online the optimal inductance and resistance respectively along constant-resistance and constant-inductance paths. The study has shown that the two paths are characterised by bell-shaped curves, which can be effectively "climbed" to the top by the extremum seeking algorithm.

Indeed, on-line experiments taken on a thin panel equipped with 5 of these control units have shown that the proposed local tuning of the five piezoelectric patches generates reductions of the resonant responses of the first, second and fourth flexural mode of the order of 14 dB, 4 dB, 8 dB

5.2.3 Chapter 4 – conclusions

In parallel to the study presented in Chapter 3 for the single-resonant shunt, Chapter 4 has contrasted the vibration control effects generated when the practical control unit formed by a piezoelectric patch connected to the multi-resonant-resonant shunt is set

(a) either to minimise the time-averaged total flexural kinetic energy of the hosting plate due to the resonant responses of the target flexural modes;

(b) or to maximise the time-averaged electric power absorbed by each branch of the shunt from the resonant response of the target flexural modes.

To start with, this Chapter has shown that the proposed tuning function based on the maximisation of the time-averaged electric power absorbed by each branch of the shunt with respect to the resonant response of a specific target flexural mode provides the same optimal resistance and inductance values that would be necessary to minimise the time-averaged flexural kinetic energy of the target flexural modes. Moreover, it has shown that the power cost function is characterised by a surface with a sequence of non-convex bell shapes having constant-resistance and constant-inductance principal directions. As a result, the two-step tuning strategy proposed for the single-resonant shunt has been adapted in such a way as the inductance is tuned first along the constant-resistance path and then the resistance is tuned along the resulting constant-inductance path. The RLC branches generate a filtering effect such that, based on their initial values, each branch filters the response of a specific target modes and the proposed tuning strategy leads to the optimal tuning that minimises the resonant response of the target mode.

In the second part, the Chapter has investigated the practical implementation of a modified version of the two-step tuning approach proposed in Chapter 2, which deals with multiple bell shapes of the cost function. The study has shown that the proposed extremum seeking algorithm can be effectively employed to "climbed" to the top of the multiple bell-shaped portions of the local cost function.

Here too, on-line experiments taken on a thin panel equipped with 5 of these control units have shown that the proposed on-line local tuning of the five piezoelectric patches generates a reduction of the resonant responses of the first, second and fourth flexural modes in the order of 10 dB 8 dB and 10 dB respectively, and a broadband effect of 6 dB reduction of overall kinetic energy over a time window.

5.3 Future Works

This thesis has proven the feasibility of a self contained vibration control unit composed by a piezoelectric patch connected to a self-tuning single resonant or multi-resonant shunt, which can be bonded on thin structures to control the flexural vibration at low frequencies, where the response is controlled by the resonant responses of low order target flexural modes. For commercial use, however, more efforts are required to develop the final product. In particular, the unit should be miniaturised in order to diminish its volume and weight. In addition, the circuitry for the actual implementation of the self-tuning shunt should be optimised in order to minimise the electric power consumption. In particular, the possibility of running intermittently the tuning algorithm should be investigated. This is quite a relevant topic, which could lead to the idea of harvesting and storing the electric power absorbed by the shunt and then using it during short time windows to update the tuning of the shunt.

Bibliography

[1] J. S. Mixson and J. F. Wilby, "Interior Noise," *Aeroacoustics of Flight Vehicles: Theory and Practice. Volume 2: Noise Control*, Jan. 1991.

[2] P. Gardonio, "Review of Active Techniques for Aerospace Vibro-Acoustic Control," *Journal of Aircraft*, vol. 39, no. 2, pp. 206–214, Mar. 2002.

[3] D. J. Thompson and J. Dixon, "Vehicle Noise," in *Advanced Applications in Acoustics, Noise and Vibration*, London: F. Fahy, J. Walker (Eds.), 2004, pp. 236–291.

[4] D. Thompson, *Railway Noise and Vibration: Mechanisms, Modelling and Means of Control*. Elsevier, Dec. 2008.

[5] X. Wang, *Vehicle Noise and Vibration Refinement*. Elsevier, Mar. 2010.

[6] A. Caiazzo, N. Alujević, B. Pluymers, and W. Desmet, "Active control of turbulent boundary layer-induced sound transmission through the cavity-backed double panels," *Journal of Sound and Vibration*, vol. 422, pp. 161–188, 2018.

[7] F. J. Fahy and P. Gardonio, *Sound and Structural Vibration: Radiation, Transmission and Response*. Elsevier, Jan. 2007.

[8] R. S. Langley and F. J. Fahy, "High-frequency structural vibration," in *Advanced Applications in Acoustics, Noise and Vibration*, London: F. Fahy, J. Walker (Eds.), 2004, pp. 490–529.

[9] P. Gardonio and E. Turco, "Tuning of vibration absorbers and Helmholtz resonators based on modal density/overlap parameters of distributed mechanical and acoustic systems," *Journal of Sound and Vibration*, vol. 451, pp. 32–70, Jul. 2019.

[10] D. J. Mead, *Passive vibration control*. John Wiley & Sons, 1998.

[11] P. A. Nelson and S. J. Elliott, *Active control of sound*. Academic press, 1991.

[12] M. J. Brennan and N. S. Ferguson, "Vibrations," in *Advanced Applications in Acoustics, Noise and Vibration*, London: F. Fahy, J. Walker (Eds.), 2004, pp. 530–580.

[13] J. P. Den Hartog, *Mechanical vibrations*. Courier Corporation, 1985.

[14] D. J. Inman and R. C. Singh, *Engineering vibration*. Prentice Hall Englewood Cliffs, NJ, 1994, vol. 3.

[15] S. Krenk and J. Høgsberg, "Tuned mass absorber on a flexible structure," *Journal of Sound and Vibration*, vol. 333, no. 6, pp. 1577–1595, Mar. 2014, ISSN: 0022460X.

[16] M. Zilletti, S. J. Elliott, P. Gardonio, and E. Rustighi, "Experimental implementation of a self-tuning control system for decentralised velocity feedback," *Journal of Sound and Vibration*, vol. 331, no. 1, pp. 1–14, Jan. 2012.

[17] D. J. Thompson, "Noise Control," in *Fundamentals of Sound and Vibration*, Chichester, U.K.: F. Fahy, D. Thompson (Eds.), 2015, pp. 213–310.

[18] D. Halim and S. R. Moheimani, "An optimization approach to optimal placement of collocated piezoelectric actuators and sensors on a thin plate," *Mechatronics*, vol. 13, no. 1, pp. 27–47, 2003.

[19] M. Trindade, "Optimization of active–passive damping treatments using piezoelectric and viscoelastic materials," *Smart Materials and Structures*, vol. 16, no. 6, p. 2159, 2007.

[20] M. A. Trindade and A. Benjeddou, "Effective electromechanical coupling coefficients of piezoelectric adaptive structures: Critical evaluation and optimization," *Mechanics of Advanced Materials and Structures*, vol. 16, no. 3, pp. 210–223, 2009.

[21] R. L. Clark and C. R. Fuller, "Optimal placement of piezoelectric actuators and polyvinylidene fluoride error sensors in active structural acoustic control approaches," *The Journal of the Acoustical Society of America*, vol. 92, no. 3, pp. 1521–1533, 1992.

[22] B.-T. Wang, R. A. Burdisso, and C. R. Fuller, "Optimal placement of piezoelectric actuators for active structural acoustic control," *Journal of Intelligent Material Systems and Structures*, vol. 5, no. 1, pp. 67–77, 1994.

[23] A. Preumont, *Vibration control of active structures: an introduction*. Springer, 2018, vol. 246.

[24] S. Skogestad and I. Postlethwaite, *Multivariable feedback control: analysis and design*. Citeseer, 2007, vol. 2.

[25] S. E. Burke, J. E. Hubbard Jr, and J. E. Meyer, "Colocation: Design constraints for distributed and discrete transducers," in *International Design Engineering Technical Conferences and Computers and Information in Engineering Conference*, American Society of Mechanical Engineers, vol. 6258, 1991, pp. 75–81.

[26] T. Bailey and J. E. Hubbard Jr, "Distributed piezoelectric-polymer active vibration control of a cantilever beam," *Journal of Guidance, Control, and Dynamics*, vol. 8, no. 5, pp. 605–611, 1985.

[27] C. Fuller, "Feedforward control of vibration," 2001.

[28] R. Burdisso and C. R. Fuller, "Theory of feedforward controlled system eigenproperties," *Journal of Sound and Vibration*, vol. 153, no. 3, pp. 437–451, 1992.

[29] C. C. Fuller, S. J. Elliott, and P. A. Nelson, *Active control of vibration*. Academic press, 1996.

[30] P. Gardonio and S. J. Elliott, "Smart panels with velocity feedback control systems using triangularly shaped strain actuators," *The Journal of the Acoustical Society of America*, vol. 117, no. 4, pp. 2046–2064, 2005.

[31] Y. Aoki, P. Gardonio, and S. J. Elliott, "Rectangular plate with velocity feedback loops using triangularly shaped piezoceramic actuators: Experimental control performance," *The Journal of the Acoustical Society of America*, vol. 123, no. 3, pp. 1421–1426, 2008.

[32] P. Gardonio and N. Alujević, "Double panel with skyhook active damping control units for control of sound radiation," *Journal of the Acoustical Society of America*, vol. 128, no. 3, pp. 1108–1117, 2010.

[33] N. Alujević, H. Wolf, B. Depraetere, *et al.*, "Self-tuneable velocity feedback for active isolation of random vibrations in subcritical two degree of freedom systems," *Acta acustica united with acustica*, vol. 101, no. 5, pp. 950–963, 2015.

[34] M. Zilletti, S. J. Elliott, and P. Gardonio, "Self-tuning control systems of decentralised velocity feedback," *Journal of Sound and Vibration*, vol. 329, no. 14, pp. 2738–2750, 2010.

[35] N. Alujević, D. Čakmak, H. Wolf, and M. Jokić, "Passive and active vibration isolation systems using inerter," *Journal of Sound and Vibration*, vol. 418, pp. 163–183, 2018.

[36] K. Ogata, *System Dynamics*, 4th ed. Upple Saddle River, 2003.

[37] S. Kumar, R. Sehgal, M. Wani, and M. D. Sharma, "Stabilization and tribological properties of magnetorheological (MR) fluids: A review," *Journal of Magnetism and Magnetic Materials*, vol. 538, p. 168 295, 2021.

[38] D. J. Klingenberg, "Magnetorheology: Applications and challenges," *American Institute of Chemical Engineers. AIChE Journal*, vol. 47, no. 2, p. 246, 2001.

[39] A. Planes and L. Mañosa, "Vibrational properties of shape-memory alloys," *Solid state physics*, vol. 55, pp. 159–267, 2001.

[40] C. A. Rogers, "Active vibration and structural acoustic control of shape memory alloy hybrid composites: Experimental results," *The Journal of the Acoustical Society of America*, vol. 88, no. 6, pp. 2803–2811, 1990, Publisher: Acoustical Society of America.

[41] E. Rustighi, M. J. Brennan, and B. R. Mace, "A shape memory alloy adaptive tuned vibration absorber: Design and implementation," *Smart materials and Structures*, vol. 14, no. 1, p. 19, 2004, Publisher: IOP Publishing.

[42] M. A. Savi, A. S. De Paula, and D. C. Lagoudas, "Numerical investigation of an adaptive vibration absorber using shape memory alloys," *Journal of Intelligent Material Systems and Structures*, vol. 22, no. 1, pp. 67–80, 2011, Publisher: Sage Publications Sage UK: London, England.

[43] R. S. Silva, T. G. Ritto, and M. A. Savi, "Shape memory alloy couplers applied for torsional vibration attenuation of drill-string systems," *Journal of Petroleum Science and Engineering*, vol. 202, p. 108 546, 2021.

[44] J. McCormick, R. DesRoches, D. Fugazza, and F. Auricchio, "Seismic vibration control using superelastic shape memory alloys," 2006.

[45] S. Behrens, A. Fleming, and S. R. Moheimani, "Electromagnetic shunt damping," in *Proceedings 2003 IEEE/ASME International Conference on Advanced Intelligent Mechatronics (AIM 2003)*, IEEE, vol. 2, 2003, pp. 1145–1150.

[46] A. McDaid and B. Mace, "A self-tuning electromagnetic vibration absorber with adaptive shunt electronics," *Smart materials and structures*, vol. 22, no. 10, p. 105 013, 2013, Publisher: IOP Publishing.

[47] S. J. Elliott and M. Zilletti, "Scaling of electromagnetic transducers for shunt damping and energy harvesting," *Journal of sound and vibration*, vol. 333, no. 8, pp. 2185–2195, 2014.

[48] C. Paulitsch, P. Gardonio, and S. J. Elliott, "Active vibration damping using an inertial, electrodynamic actuator (DETC2005-84632)," *Journal of Vibration and Acoustics*, vol. 129, no. 1, pp. 39–47, Feb. 2007. (visited on 08/17/2022).

[49] T. Inoue, Y. Ishida, and M. Sumi, "Vibration suppression using electromagnetic resonant shunt damper," *Journal of Vibration and Acoustics*, vol. 130, no. 4, p. 041 003, Aug. 2008.

[50] X. Zhang, H. Niu, and B. Yan, "A novel multimode negative inductance negative resistance shunted electromagnetic damping and its application on a cantilever plate," *Journal of Sound and Vibration*, vol. 331, no. 10, pp. 2257–2271, 2012, Publisher: Elsevier.

[51] B. Yan, X. Zhang, Y. Luo, Z. Zhang, S. Xie, and Y. Zhang, "Negative impedance shunted electromagnetic absorber for broadband absorbing: Experimental investigation," *Smart Mater. Struct.*, vol. 23, no. 12, p. 125 044, Dec. 2014.

[52] S. Miani, M. Zilletti, P. Gardonio, F. Blanchini, and P. Colaneri, "Switching and sweeping vibration absorbers: Theory and experimental validation," *Automatica*, vol. 93, pp. 290–301, 2018.

[53] E. Turco, P. Gardonio, R. Petrella, and L. Dal Bo, "Modular vibration control unit formed by an electromagnetic proof-mass transducer and sweeping resistive–inductive shunt," *Journal of Vibration and Acoustics*, vol. 142, no. 6, p. 061 005, 2020, Publisher: American Society of Mechanical Engineers.

[54] D. Niederberger, S. Behrens, A. J. Fleming, S. R. Moheimani, and M. Morari, "Adaptive electromagnetic shunt damping," *IEEE/ASME Transactions on Mechatronics*, vol. 11, no. 1, pp. 103–108, 2006, Publisher: IEEE.

[55] A. J. McDaid and B. R. Mace, "A robust adaptive tuned vibration absorber using semi-passive shunt electronics," *IEEE Transactions on Industrial Electronics*, vol. 63, no. 8, pp. 5069–5077, 2016, Publisher: IEEE.

[56] P. Gardonio, E. Turco, A. Kras, L. Dal Bo, and D. Casagrande, "Semi-active vibration control unit tuned to maximise electric power dissipation," *Journal of Sound and Vibration*, vol. 499, p. 116 000, May 2021.

[57] E. Turco, P. Gardonio, and L. Dal Bo, "Tuning of a shunted electromagnetic vibration absorber based on the maximisation of the electrical power dissipated," *Proceedings of the Institution of Mechanical Engineers, Part C: Journal of Mechanical Engineering Science*, vol. 235, no. 14, pp. 2570–2586, Jul. 2021.

[58] M. Zilletti, "Feedback control unit with an inerter proof-mass electrodynamic actuator," *Journal of Sound and Vibration*, vol. 369, pp. 16–28, 2016.

[59] R. L. Forward, "Electronic damping of vibrations in optical structures," *Applied optics*, vol. 18, no. 5, pp. 690–697, 1979, Publisher: Optica Publishing Group.

[60] N. Hagood and A. von Flotow, "Damping of structural vibrations with piezoelectric materials and passive electrical networks," *Journal of Sound and Vibration*, vol. 146, no. 2, pp. 243–268, 1991.

[61] S. R. Moheimani and A. J. Fleming, *Piezoelectric transducers for vibration control and damping*. Springer, 2006, vol. 1.

[62] S.-Y. Wu, "Piezoelectric shunts with a parallel RL circuit for structural damping and vibration control," in *Smart Structures and Materials 1996: Passive Damping and Isolation*, vol. 2720, SPIE, May 1996, pp. 259–269.

[63] J. Høgsberg and S. Krenk, "Balanced calibration of resonant shunt circuits for piezoelectric vibration control," *Journal of Intelligent Material Systems and Structures*, vol. 23, no. 17, pp. 1937–1948, Nov. 2012.

[64] P. Soltani, G. Kerschen, G. Tondreau, and A. Deraemaeker, "Piezoelectric vibration damping using resonant shunt circuits: An exact solution," *Smart Materials and Structures*, vol. 23, no. 12, p. 125 014, Oct. 2014, Publisher: IOP Publishing.

[65] M. Berardengo, A. Cigada, S. Manzoni, and M. Vanali, "Vibration control by means of piezoelectric actuators shunted with LR impedances: Performance and robustness analysis," *Shock and Vibration*, vol. 2015, e704265, May 2015.

[66] P. Gardonio and D. Casagrande, "Shunted piezoelectric patch vibration absorber on two-dimensional thin structures: Tuning considerations," *Journal of Sound and Vibration*, vol. 395, pp. 26–47, May 2017.

[67] O. Thomas, J. Ducarne, and J.-F. Deü, "Performance of piezoelectric shunts for vibration reduction," *Smart Materials and Structures*, vol. 21, no. 1, p. 015 008, 2011, Publisher: IOP Publishing.

[68] G. Zhao, N. Alujević, B. Depraetere, and P. Sas, "Dynamic analysis and H_2 optimisation of a piezo-based tuned vibration absorber," *Journal of Intelligent Material Systems and Structures*, vol. 26, no. 15, pp. 1995–2010, 2015.

[69] S. R. Moheimani, "A survey of recent innovations in vibration damping and control using shunted piezoelectric transducers," *IEEE transactions on control systems technology*, vol. 11, no. 4, pp. 482–494, 2003.

[70] J. J. Hollkamp and T. F. Starchville, "A self-tuning piezoelectric vibration absorber," *Journal of Intelligent Material Systems and Structures*, vol. 5, no. 4, pp. 559–566, Jul. 1994.

[71] A. J. Fleming and S. O. R. Moheimani, "Adaptive piezoelectric shunt damping," *Smart Mater. Struct.*, vol. 12, no. 1, pp. 36–48, Feb. 2003.

[72] D. Niederberger, A. Fleming, S. R. Moheimani, and M. Morari, "Adaptive multi-mode resonant piezoelectric shunt damping," *Smart Materials and Structures*, vol. 13, no. 5, p. 1025, 2004.

[73] M. Ogawa, K. Takagi, I. Jikuya, and T. Inoue, "Adaptive piezoelectric shunt damping by self-tuning negative capacitor," *Transactions of the JSME*, vol. 80, no. 820, DR0382–DR0382, 2014.

[74] J. Gripp, O. Heuss, L. Góes, and T. Melz, "Adaptive resonant piezoelectric shunt damping enhanced by a synthetic negative capacitance," *Proceedings of ISMA2014 Including USD2014*, pp. 653–666, 2014.

[75] K. Uchino and T. Ishii, "Mechanical damper using piezoelectric ceramics," *Journal of the Ceramic Society of Japan*, vol. 96, no. 1116, pp. 863–867, 1988.

[76] J. E. Brock, "A note on the damped vibration absorber," 1946, Publisher: American Society of Mechanical Engineers.

[77] O. Nishihara and T. Asami, "Closed-form solutions to the exact optimizations of dynamic vibration absorbers (minimizations of the maximum amplitude magnification factors)," *J. Vib. Acoust.*, vol. 124, no. 4, pp. 576–582, 2002.

[78] T. Asami, O. Nishihara, and A. M. Baz, "Analytical solutions to H_∞ and H_2 optimization of dynamic vibration absorbers attached to damped linear systems," *J. Vib. Acoust.*, vol. 124, no. 2, pp. 284–295, 2002.

[79] J. Høgsberg and S. Krenk, "Calibration of piezoelectric RL shunts with explicit residual mode correction," *Journal of Sound and Vibration*, vol. 386, pp. 65–81, Jan. 2017.

[80] T. Ikegame, K. Takagi, and T. Inoue, "Exact solutions to H_∞ and H_2 optimizations of passive resonant shunt circuit for electromagnetic or piezoelectric shunt damper," *Journal of Vibration and Acoustics*, vol. 141, no. 3, 2019, Publisher: American Society of Mechanical Engineers Digital Collection.

[81] M. Neubauer, R. Oleskiewicz, K. Popp, and T. Krzyzynski, "Optimization of damping and absorbing performance of shunted piezo elements utilizing negative capacitance," *Journal of Sound and Vibration*, vol. 298, no. 1, pp. 84–107, Nov. 2006.

[82] K. Yamada, H. Matsuhisa, H. Utsuno, and K. Sawada, "Optimum tuning of series and parallel LR circuits for passive vibration suppression using piezoelectric elements," *Journal of Sound and Vibration*, vol. 329, no. 24, pp. 5036–5057, Nov. 2010.

[83] G. Caruso, "A critical analysis of electric shunt circuits employed in piezoelectric passive vibration damping," *Smart materials and structures*, vol. 10, no. 5, p. 1059, 2001, Publisher: IOP Publishing.

[84] J. Kim, Y.-H. Ryu, and S.-B. Choi, "New shunting parameter tuning method for piezoelectric damping based on measured electrical impedance," *Smart Materials and Structures*, vol. 9, no. 6, p. 868, 2000, Publisher: IOP Publishing.

[85] J. Kim and J.-K. Lee, "Broadband transmission noise reduction of smart panels featuring piezoelectric shunt circuits and sound-absorbing material," *The Journal of the Acoustical Society of America*, vol. 112, no. 3, pp. 990–998, Sep. 2002.

[86] J. Kim and J.-Y. Choi, "Performance test for transmitted noise reduction of smart panels using piezoelectric shunt damping," *Smart materials and structures*, vol. 14, no. 4, p. 587, 2005, Publisher: IOP Publishing.

[87] H. Hanselka, "Adaptronik und fragen zur systemzuverlassigkeit," *Automatisierungstechnische Praxis*, vol. 44, no. 2, pp. 40–49, 2002.

[88] D. Niederberger, M. Morari, and S. J. Pietrzko, "Adaptive resonant shunted piezoelectric devices for vibration suppression," in *Smart Structures and Materials 2003: Smart Structures and Integrated Systems*, SPIE, vol. 5056, 2003, pp. 213–224.

[89] G. Matten, M. Collet, E. Sadoulet-Reboul, and S. Cogan, "Sensitivity analysis and control of a cantilever beam by mean of a shunted piezoelectric patch," in *1st Euro-Mediterranean Conference on Structural Dynamics and Vibroacoustics (MEDYNA 2013)*, France, Jan. 2013, pp. 1–4.

[90] U. Andreaus and M. Porfiri, "Effect of electrical uncertainties on resonant piezoelectric shunting," *Journal of Intelligent Material Systems and Structures*, vol. 18, no. 5, pp. 477–485, May 2007, ISSN: 1045-389X, 1530-8138.

[91] R. Darleux, B. Lossouarn, and J.-F. Deü, "Passive self-tuning inductor for piezoelectric shunt damping considering temperature variations," *Journal of Sound and Vibration*, vol. 432, pp. 105–118, Oct. 2018.

[92] W.-K. Chen, *Passive, active, and digital filters*. CRC Press, 2018.

[93] P. Horowitz and W. Hill, *The art of electronics*, 2nd ed. Cambridge, England: Cambridge University Press, 1989.

[94] A. J. Fleming, S. Behrens, and S. O. R. Moheimani, "Synthetic impedance for implementation of piezoelectric shunt-damping circuits," *Electronics Letters*, vol. 36, no. 18, pp. 1525–1526, Aug. 2000.

[95] L. Dal Bo, P. Gardonio, D. E. Casagrande, and S. Saggini, "Smart panel with sweeping and switching piezoelectric patch vibration absorbers: Experimental results," *Mechanical Systems and Signal Processing*, vol. 120, pp. 308–325, Apr. 2019.

[96] G. Raze, A. Jadoul, S. Guichaux, V. Broun, and G. Kerschen, "A digital nonlinear piezoelectric tuned vibration absorber," *Smart Mater. Struct.*, vol. 29, no. 1, p. 015 007, Jan. 2020.

[97] R. L. Forward, *Electromechanical transducer-coupled mechanical structure with negative capacitance compensation circuit*, US Patent 4,158,787, Jun. 1979.

[98] S.-Y. Wu, *Broadband piezoelectric shunts for structural vibration control*, US Patent 6,075,309, Jun. 2000.

[99] M. Tsai and K. Wang, "On the structural damping characteristics of active piezoelectric actuators with passive shunt," *Journal of Sound and Vibration*, vol. 221, no. 1, pp. 1–22, Mar. 1999.

[100] S. Behrens, A. J. Fleming, and S. O. R. Moheimani, "A broadband controller for shunt piezoelectric damping of structural vibration," *Smart Mater. Struct.*, vol. 12, no. 1, pp. 18–28, Feb. 2003.

[101] C. H. Park and A. Baz, "Vibration control of beams with negative capacitive shunting of interdigital electrode piezoceramics," *Journal of Vibration and Control*, vol. 11, no. 3, pp. 331–346, Mar. 2005.

[102] B. de Marneffe and A. Preumont, "Vibration damping with negative capacitance shunts: Theory and experiment," *Smart Mater. Struct.*, vol. 17, no. 3, p. 035 015, Jun. 2008.

[103] K. B. Ariyur and M. Krstic, *Real-Time Optimization by Extremum-Seeking Control*. John Wiley & Sons, Oct. 2003.

[104] I. S. Morosanov, "Method of extremum control," *Automatic and Remote Control*, vol. 18, pp. 1077–1092, 1957.

[105] Y. Ostrovsky, "Extremum regulation," *Avtomat. i Telemechan.*, vol. 18, pp. 852–858, 1957.

[106] S. M. Meerkov, "Asymptotic methods for investigating a class of forced states in extremal systems," *Automation and Remote Control*, vol. 28, no. 12, pp. 1916–1920, 1967.

[107] M. Krstić, "Performance improvement and limitations in extremum seeking control," *Systems & Control Letters*, vol. 39, no. 5, pp. 313–326, Apr. 2000.

[108] M. Krstić and H.-H. Wang, "Stability of extremum seeking feedback for general nonlinear dynamic systems," *Automatica*, vol. 36, no. 4, pp. 595–601, Apr. 2000.

[109] A. Scheinker and M. Krstić, "Minimum-seeking for CLFs: Universal semiglobally stabilizing feedback under unknown control directions," *IEEE Transactions on Automatic Control*, vol. 58, no. 5, pp. 1107–1122, May 2013.

[110] P. Gardonio, S. Miani, F. Blanchini, D. Casagrande, and S. J. Elliott, "Plate with decentralised velocity feedback loops: Power absorption and kinetic energy considerations," *Journal of Sound and Vibration*, vol. 331, no. 8, pp. 1722–1741, Apr. 2012.

[111] O. Bardou, P. Gardonio, S. J. Elliott, and R. J. Pinnington, "Active power minimization and power absorption in a plate with force and moment excitation," *Journal of Sound and Vibration*, vol. 208, no. 1, pp. 111–151, Nov. 1997.

[112] P. Gardonio and L. Dal Bo, "Scaling laws of electromagnetic and piezoelectric seismic vibration energy harvesters built from discrete components," *Journal of Sound and Vibration*, vol. 476, p. 115 290, Jun. 2020.

[113] A. Preumont, *Mechatronics: dynamics of electromechanical and piezoelectric systems*. Dordrecht: Springer, 2006.

[114] A. G. Piersol and J. S. Bendat, *Random data: analysis and measurement procedures*. 2013.

[115] Y. Tan, W. Moase, C. Manzie, D. Nešić, and I. Mareels, "Extremum seeking from 1922 to 2010," in *Proceedings of the 29th Chinese Control Conference*, Jul. 2010, pp. 14–26.

[116] D. Dochain, M. Perrier, and M. Guay, "Extremum seeking control and its application to process and reaction systems: A survey," *Mathematics and Computers in Simulation*, 6th Vienna International Conference on Mathematical Modelling, vol. 82, no. 3, pp. 369–380, Nov. 2011.

[117] H. A. Sodano, G. Park, and D. J. Inman, "An investigation into the performance of macro-fiber composites for sensing and structural vibration applications," *Mechanical Systems and Signal Processing*, vol. 18, no. 3, pp. 683–697, May 2004.

[118] P. Gardonio, G. Konda Rodrigues, L. Dal Bo, and E. Turco, "Extremum seeking online tuning of a piezoelectric vibration absorber based on the maximisation of the shunt electric power absorption," *Mechanical Systems and Signal Processing*, vol. 176, p. 109 171, Aug. 2022.

[119] P. Gardonio, M. Zientek, and L. Dal Bo, "Panel with self-tuning shunted piezoelectric patches for broadband flexural vibration control," *Mechanical Systems and Signal Processing*, vol. 134, p. 106 299, Dec. 2019.

[120] N. W. Hagood, W. H. Chung, and A. Von Flotow, "Modelling of piezoelectric actuator dynamics for active structural control," *Journal of Intelligent Material Systems and Structures*, vol. 1, no. 3, pp. 327–354, Jul. 1990.

[121] S. H. Crandall, D. C. Karnopp, A. F. Kurtz, and D. C. Pridmore-Brown, *Dynamics of Mechanical and Electromechanical Systems*. 1968.

[122] J. N. Reddy, *Mechanics of laminated composite plates: theory and analysis*. Boca Raton: CRC Press, 1997.

[123] J. N. Reddy, *Theory and analysis of elastic plates and shells*, eng, 2. ed. Boca Raton, Fla.: CRC Press, 2007.

[124] L. Meirovitch, *Principles and techniques of vibrations*. Upper Saddle River, N.J: Prentice Hall, 1997.

[125] L. Dal Bo, H. He, P. Gardonio, Y. Li, and J. Z. Jiang, "Design tool for elementary shunts connected to piezoelectric patches set to control multi-resonant flexural vibrations," *Journal of Sound and Vibration*, vol. 520, p. 116 554, Mar. 2022.

[126] K. Shin and J. K. Hammond, *Fundamentals of signal processing for sound and vibration engineers*. Chichester, England; Hoboken, NJ: John Wiley & Sons, 2008.

[127] C.-K. Lee and F. C. Moon, "Modal sensors/actuators," *Journal of Applied Mechanics*, vol. 57, no. 2, pp. 434–441, Jun. 1990.

[128] Y. Gu, R. L. Clark, C. R. Fuller, and A. C. Zander, "Experiments on active control of plate vibration using piezoelectric actuators and polyvinylidene fluoride (PVDF) modal sensors," *Journal of Vibration and Acoustics*, vol. 116, no. 3, pp. 303–308, Jul. 1994.

[129] P. Gardonio, Y.-S. Lee, S. J. Elliott, and S. Debost, "Analysis and measurement of a matched volume velocity sensor and uniform force actuator for active structural acoustic control," *The Journal of the Acoustical Society of America*, vol. 110, no. 6, pp. 3025–3031, Dec. 2001.

[130] H. Sumali, K. Meissner, and H. H. Cudney, "A piezoelectric array for sensing vibration modal coordinates," *Sensors and Actuators A: Physical*, vol. 93, no. 2, pp. 123–131, Sep. 2001.

[131] J. J. Hollkamp, "Multimodal passive vibration suppression with piezoelectric materials and resonant shunts," *Journal of intelligent material systems and structures*, vol. 5, no. 1, pp. 49–57, 1994.

[132] G. Konda Rodrigues, P. Gardonio, L. Dal Bo, and E. Turco, "Piezoelectric patch vibration control unit connected to a self-tuning rl-shunt set to maximise electric power absorption," *Journal of Sound and Vibration*, vol. 536, p. 117 154, 2022.

[133] C. Fuller, C. Rogers, and H. Robertshaw, "Control of sound radiation with active/adaptive structures," *Journal of Sound and Vibration*, vol. 157, no. 1, pp. 19–39, 1992.

[134] G. Ferrari and M. Amabili, "Active vibration control of a sandwich plate by non-collocated positive position feedback," *Journal of Sound and Vibration*, vol. 342, pp. 44–56, 2015.

[135] A. Alaimo, A. Milazzo, and C. Orlando, "A smart composite-piezoelectric one-dimensional finite element model for vibration damping analysis," *Journal of Intelligent Material Systems and Structures*, vol. 27, no. 10, pp. 1362–1375, 2016.

[136] R. L. Clark and C. R. Fuller, "Experiments on active control of structurally radiated sound using multiple piezoceramic actuators," *The Journal of the Acoustical Society of America*, vol. 91, no. 6, pp. 3313–3320, 1992.

[137] C. R. Fuller and R. J. Silcox, "Acoustics 1991: Active structural acoustic control," *The Journal of the Acoustical Society of America*, vol. 91, no. 1, pp. 519–519, 1992.

[138] W. T. Baumann, F.-S. Ho, and H. H. Robertshaw, "Active structural acoustic control of broadband disturbances," *The Journal of the Acoustical Society of America*, vol. 92, no. 4, pp. 1998–2005, 1992.

[139] B. Petitjean, I. Legrain, F. Simon, and S. Pauzin, "Active control experiments for acoustic radiation reduction of a sandwich panel: Feedback and feedforward investigations," *Journal of sound and vibration*, vol. 252, no. 1, pp. 19–36, 2002.

[140] E. Bianchi, P. Gardonio, and S. Elliott, "Smart panel with multiple decentralized units for the control of sound transmission. part iii: Control system implementation," *Journal of sound and vibration*, vol. 274, no. 1-2, pp. 215–232, 2004.

[141] P. Gardonio, E. Turco, and L. Dal Bo, "Comparison of smart panels for tonal and broadband vibration and sound transmission active control," *International Journal of Smart and Nano Materials*, vol. 11, no. 4, pp. 431–484, 2020.

[142] M. A. Trindade, A. Benjeddou, and R. Ohayon, "Piezoelectric active vibration control of damped sandwich beams," *Journal of Sound and Vibration*, vol. 246, no. 4, pp. 653–677, 2001.